

3D Manufacturing Using Laser Direct Structuring and the Application on the Development of Antenna Systems

Von der Fakultät für Elektrotechnik und Informatik
der Gottfried Wilhelm Leibniz Universität Hannover
zur Erlangung des akademischen Grades

Doktor-Ingenieurin
(abgekürzt: Dr.-Ing.)

genehmigte Dissertation

von Frau
Dipl.-Ing. Aline Friedrich

geboren am 14. März 1982 in Sebnitz/Deutschland

Hannover, 2019

1. Referent:

Prof. Dr.-Ing. Dirk Manteuffel

2. Referent:

Prof. Ronan Sauleau

Vorsitzender der Prüfungskommission:

Prof. Dr. Jürgen Peissig

Tag der Promotion:

17.05.2019

Danksagung

Die folgende Arbeit entstand während meiner Tätigkeit als wissenschaftliche Mitarbeiterin am Institut für Hochfrequenztechnik und Funksysteme der Leibniz Universität Hannover. Dabei habe ich vielfältige Unterstützung erfahren für die ich mich an dieser Stelle bedanken möchte.

Mein besonderer Dank gilt Prof. Dr.-Ing. Dirk Manteuffel, der während der wesentlichen Zeit dieser Arbeit mein Betreuer war. Insbesondere seine motivierende Art mich zur fachlichen Weiterentwicklung meiner Arbeit anzuregen war mir eine große Hilfe.

Ich danke ebenfalls Prof. Ronan Sauleau für das Interesse am Thema meiner Arbeit und die Übernahme des Koreferats und Prof. Dr. Jürgen Peissig für die Übernahme des Prüfungsvorsitzes.

Danken möchte ich an dieser Stelle meinen beiden Bürokollegen Quang Huy Dao und Lukas Berkelmann. Es hat mir großen Spaß gemacht, mit ihnen zusammenzuarbeiten, zu diskutieren und Dinge voran zu bringen. Ebenso danke ich Christian Zietz, Steffen Probst, Nikolai Peitzmeier, Christian Orlob, Johannes Meyer, Timo Martinelli, Henning Hartmann und Eckhard Denicke für die kollegiale Zusammenarbeit und Gemeinschaft. Darüber hinaus möchte ich mich bei apl. Prof. Dr.-Ing. Bernd Geck für seine Unterstützung insbesondere in der Anfangszeit meiner Arbeit am Institut bedanken.

Zudem danke ich allen Studierenden, mit denen ich in meiner Zeit am Institut zusammenarbeiten konnte.

Mein Dank gilt ebenfalls den Mitarbeitern der BMW Group, die mich bei der Durchführung dieser Arbeit begleitet haben. Ausdrücklich möchte ich dabei Adrian Posselt, Oliver Klemp und Christian Arendt für ihren fachliche Rat und die persönliche Unterstützung bei der Erstellung dieser Arbeit danken.

Ich habe weitere Unterstützung von der LPKF Laser & Electronics AG erhalten. Ich danke allen Mitarbeitern und ehemaligen Mitarbeitern, insbesondere Malte Fengler, Lars Führmann und Andreas Fischer für ihre Hilfe in allen Fragen

zur Fertigungstechnik.

Abschließend danke ich meiner Familie, insbesondere meinen Eltern Ramona und Dietmar Friedrich und meiner Schwester Christin sowie meinen guten Freunden Tatjana und Hanno Rabe für ihre Unterstützung bei der Erstellung dieser Arbeit.

Kurzfassung

Die Entwicklung von Funksystemen unterliegt ständig wachsenden Anforderungen. Diese betreffen sowohl die zu realisierende Funktion als auch die geometrische Konfiguration in immer kleiner werdenden Bauräumen. Dies führt insbesondere dazu, dass Antennen nicht mehr nur als Einzelkomponente entwickelt und darauffolgend integriert werden können. Es ist vielmehr erforderlich den Bauraum als Teil der Antenne zu betrachten und diesen entsprechend elektromagnetisch zu funktionalisieren. Eine Fertigungstechnologie, die diesen Ansatz inhärent aufgreift, ist die 3D MID (Moulded Interconnect Devices) Technologie. Diese ermöglicht eine selektive Metallisierung von Kunststoffteilen. Die elektronische/elektromagnetische Funktionalisierung von mechanischen Komponenten, wie zum Beispiel Gehäuseteilen, wird damit möglich. Die Fertigungs- und Materialparameter der verschiedenen MID-Herstellungsverfahren sind häufig lediglich für die mechanischen oder elektrischen Anforderungen charakterisiert obwohl z.B. das LDS (Laser Direkt Strukturierung)-Verfahren bereits seit Jahren für die Fertigung von Antennen in Endverbrauchgeräten eingesetzt wird. Ziel der vorliegenden Arbeit ist es daher eine strukturierte technologische Analyse des LDS-Verfahrens für Hochfrequenzanwendungen bis 70 GHz durchzuführen und diese Erkenntnisse anhand von Antennenentwicklungen zu verifizieren, die den durch die Technologie gegebenen dreidimensionalen Designspielraum möglichst umfassend nutzen.

Nach einer Beschreibung des LDS-Verfahrens werden die relevanten Parameter in Bezug auf HF Systeme abgeleitet. Auf Basis dieser erfolgt eine detaillierte Diskussion der mechanischen Parameter, der dielektrischen Materialparameter der LDS-Kunststoffe sowie die der applizierten Metallisierung. Die gewonnenen Erkenntnisse werden durch Messungen verifiziert.

Darauffolgend werden die gewonnenen Daten für die Entwicklung verschiedener Antennenkonzepte verwendet. Zuerst erfolgt die Entwicklung zweier Antennensysteme für die Integration in ein Fahrzeug. Das erste System greift den aktuell vorhandenen Bauraum eines Dachantennenmoduls auf, während ein zweites System auf einen neuartigen Bauraum zur Integration abzielt. Die entwickelten Antennen werden mit dem LDS-Verfahren realisiert und charakterisiert.

Im Weiteren erfolgt die Betrachtung zweier Antennenkonzepte, die von einem konkreten Bauraum unabhängigen sind, jedoch die Möglichkeit zur Adaption an den Bauraum als Optimierungsziel berücksichtigen. Ein Konzept bezieht sich auf Mikrostreifenleitungsantennen. Der in diesem Rahmen realisierte aktive GPS Antennenprototyp vereint Beschaltung und Antenne auf einem dreidimensionalen Substrat. Als zweiter Ansatz werden von Hohlleitern gespeiste Antennen diskutiert. Zwei Prototypen im 24 GHz und 61 GHz ISM-Band verifizieren die Eignung der Fertigungstechnologie für Frequenzen im Bereich der Millimeter-Wellen. Abschließend erfolgt eine auf einen generischen Bauraum bezogene Untersuchung des Antennenkonzepts auf Basis von elektromagnetischen Feldsimulationen.

Schlagworte: Antennen, 3D Fertigungsverfahren, Laser Direkt Strukturierung

Abstract

The development of radio systems is subject to constantly increasing demands. These concern the function to be implemented as well as the geometric dimensions of the RF devices in decreasing installation spaces. One resulting aspect is that the antenna can no longer be developed as a single component and be integrated subsequently. It is rather necessary to consider the installation space as a part of the antenna and to use it electromagnetically according to the requirements. One manufacturing technology that inherently takes up this approach is Moulded Interconnect Devices (MID) technology. MIDs are three-dimensional plastic parts which are selectively metallised. The electronic/electromagnetic functionalisation of mechanical components, such as housing parts, is thus possible. The manufacturing and material parameters of the different MID manufacturing processes are often characterised regarding the mechanical or electrical requirements, although e.g. the MID LDS (Laser Direct Structuring) process has been used for years for the production of antennas in consumer devices. Therefore, the main aim of the present work is to carry out a structured technological analysis of the LDS process for high-frequency applications up to 70 GHz and to verify the results by means of antenna developments, which use the three-dimensional design scope provided by the technology.

After a description of the manufacturing process of the LDS process, the relevant parameters with regard to radio frequency systems are derived. Based thereon, a detailed discussion of the mechanical parameters, the dielectric material parameters of the LDS plastics as well as the applied metallisation is carried out. The results are verified by measurements.

These findings are subsequently used in the development of various antenna concepts which can be fabricated using the LDS process. First of all, two antenna systems are developed to be integrated into a vehicle. The first system takes up a current installation space, a roof antenna module, while a second system is aimed at a new installation space. The developed antennas are realised with the LDS method and subsequently characterised.

In addition, two antenna concepts are examined which are independent of

a specific installation space, but which take into account the possibility of adapting them to the installation space as an optimisation goal. One concept covers the use of 3D manufacturing in connection with microstrip antennas. A prototype of an active patch antenna for Global Positioning Satellite System (GPS) which combines circuit and antenna on a three-dimensional substrate is realised. The second approach includes antennas which are fed by dielectric filled waveguides. Two prototypes in the 24 GHz and 61 GHz ISM band verify the suitability of the manufacturing technology for frequencies in the millimetre wavelength range. Finally, the antenna concept is investigated on the basis of electromagnetic field simulations in a generic installation space.

Keywords: Antennas, 3D Manufacturing, Laser Direct Structuring

Contents

The Authors Publications	I
Abbreviations	III
1 Introduction	1
1.1 State of the Art	2
1.2 Objectives	4
1.3 Outline	5
2 Technological Evaluation of the Laser Direct Structuring	7
2.1 Fabrication of RF Devices	9
2.2 The Laser Direct Structuring Process	11
2.2.1 3D Antenna Design	11
2.2.2 Injection Moulding	12
2.2.3 Laser Structuring	13
2.2.4 Plating	14
2.3 Fabrication Accuracy and Surface Condition	15
2.4 RF Properties of LDS Substrate Materials	21
2.4.1 Chemical and Physical Properties	24
2.4.2 Description of the Measurement Setup	27
2.4.3 Dielectric Characterisation	30
2.4.3.1 Grilamid 1SVX-50H LDS	31
2.4.3.2 Vectra E840i LDS	34
2.4.3.3 VESTAMID HTplus M1033	37
2.4.3.4 Xantar LDS 3720 and Xantar LDS 3732	39
2.4.3.5 LPKF ProtoPaint LDS	44
2.4.4 Conclusion	45
2.5 RF Properties of LDS Metallisation	46
2.5.1 Layered Metallisation	47
2.5.2 Influences Due to Surface Quality	49
2.5.3 Influences Due to Edge Quality	51

2.5.4	LDS Fabricated Transmission Lines	51
2.5.4.1	Measurement of Propagation Constant	55
2.5.5	Conclusion	61
3	Electromagnetic Field Simulation	62
4	3D Antenna Concepts for Vehicle Integration	64
4.1	3D Roof-Top Antenna System	68
4.1.1	Prototypical Realisation	71
4.1.2	System Level Evaluation of the Integrated 3D Roof Antenna Module	78
4.1.3	Conclusion	81
4.2	3D Antenna System for a Conformal Integration	82
4.2.1	Vehicle Integration Spaces for Conformal Antenna In- tegration	82
4.2.2	Antenna Development	85
4.2.2.1	Prototypical Realisation	89
4.2.3	Evaluation of the Conformal Integrated 3D Antenna System	92
4.2.4	Conclusion	94
5	3D Fabrication for Microstrip Antennas	96
5.1	Characteristics of Microstrip Antennas	96
5.2	3D Modification of Microstrip Antennas	101
5.2.1	3D Surface Modulation	103
5.2.2	Combined 3D Microstrip Antenna and Circuitry	109
5.3	Realisation of 3D Active GPS Antenna	113
6	3D Fabrication for Waveguide Fed Antennas	120
6.1	Concept for LDS Fabricated Waveguide Fed Antennas	120
6.2	Feeding Concepts	123
6.3	Prototypic Realisation	127
6.4	Plastic Integrated Waveguide Fed Antennas	131
7	Conclusion	135
	References	137

The Authors Publications

The following work contains material that is based on the following publications and contributions authored or co-authored by the author. The publications are cited in the specific Section.

- [AF1] A. Friedrich and M. Fengler and B. Geck and D. Manteuffel (2017): 60 GHz 3D integrated waveguide fed antennas using laser direct structuring technology, 2017 11th European Conference on Antennas and Propagation (EUCAP), pp. 2507-2510 (©IEEE 2017)
- [AF2] A. Friedrich, M. Fengler, A. Fischer, B. Geck (2016): 24 GHz Dielectric Filled Waveguide Fed Horn Antenna Using 3D-LDS MID Technology, European Microwave Conference (EUMC 2016), London, Germany, October 3-7, 2016 (©IEEE 2016)
- [AF3] A. Friedrich, M. Fengler, B. Geck (2016): LDS MIDs Fit for mmWave, Microwave Journal, no. 9, vol. 59, September 2016
- [AF4] A. Friedrich, M. Fengler, B. Geck (2016): LDS Manufacturing Technology for Next Generation Radio Frequency and Sensor Applications - A discussion on Requirements and Solutions -, 12th International Congress Molded Interconnect Devices 2016, Würzburg, Germany, September 28-29, 2016 (©IEEE 2016)
- [AF5] A. Friedrich, L. Berkelmann, T. Martinelli, B. Geck, O. Klemp, I. Kriebitzsch (2015): An Active Three-Dimensional GPS Patch Antenna Using MID-Technology, European Microwave Conference 2015 (EuMC 2015), Paris, France, September 7 - 11, 2015 (©IEEE 2015)
- [AF6] A. Friedrich, B. Geck, O. Klemp, A. Posselt, I. Kriebitzsch (2014): 3D-Antennensysteme - Design und Validierung, ATZ-Elektronik 9, Nr. 6, S. 44-51, Springer Vieweg, Dezember 2014 (© Springer Vieweg 2014)

[AF7] A. Friedrich, Q. H. Dao, B. Geck (2014): Charakterisierung der Hochfrequenz-Eigenschaften von Materialien für LDS-MID, PLUS Produktion von Leiterplatten und Systemen, Leuze Verlag, Februar, 2014

[AF8] A. Friedrich, B. Geck, O. Klemp, H. Kellermann (2013): On the Design of a 3D LTE Antenna for Automotive Applications based on MID Technology, European Microwave Conference 2013 (EuMC 2013), Nürnberg, Deutschland, October 6 - 11, 2013 (©IEEE 2013)

Co-Authored:

[AP1] A. Posselt, A. Friedrich, L. Ekiz, O. Klemp, B. Geck (2014): System-Level Assessment of Volumetric 3D Vehicular MIMO Antenna Based on Measurement, The 3rd International Conference on Connected Vehicles & Expo (ICCVE 2014), Vienna, Austria, November 3-7, 2014 (©IEEE 2014)

[OK1] O. Klemp, A. Friedrich, B. Geck, A. Posselt (2014): 3D-Antennensysteme - Anforderungen an die Fahrzeugintegration, ATZ - Automobiltechnische Zeitschrift 116, Springer Vieweg, Nr. 12, S. 60-65 (© Springer Vieweg 2014)

Patent:

[AF9] A. Friedrich, A. Posselt, O. Klemp (2017): Patent: Antennenelement, Empfänger, Sender, Sendeempfänger, Fahrzeug und Verfahren zum Herstellen eines Antennenelements, Publication No. DE 102015216147 A1, BMW Group (Applicant) March 2, 2017 (Publication Date)

Abbreviations

AR	Axial Ratio
ABS	Acrylnitril Butadien Styrol
AM	Amplitude Modulation
CPW	Coplanar Waveguide
DAB	Digital Audio Broadcasting
DC	Direct Current
ENIG	Electroless Nickel Immersion Gold
EM	Electromagnetic
ECAD	Electrical Computer Aided Design
FM	Frequency Modulation
FDM	Fused Deposition Modeling
GSM	Global System for Mobile Communications
GPS	Global Positioning Satellite System
GCPW	Grounded Coplanar Waveguide
GNSS	Global Navigation Satellite System
LDS	Laser Direct Structuring
LCP	Liquid Crystal Polymer
LNA	Low Noise Amplifier
LER	Line Edge Roughness
LTE	Long Term Evolution
MIMO	Multiple Input Multiple Output

MSL	Microstrip line
MCAD	Mechanical Computer Aided Design
MID	Molded Interconnect Devices
PCB	Printed Circuit Board
PA	Polyamid
PC	Polycarbonate
PIM	Passive Intermodulation
PPA	Polyphthalamide
RMS	Root Mean Square
RF	Radio Frequency
SMT	Surface Mount Technology
SMA	Surface Mount Assembly
SEM	Scanning Electron Microscope
SLA	Stereolithography Apparatus
SLS	Selective Laser Sintering
SAW	Surface Accoustic Wave
SIW	Substrate Integrated Waveguide
TM	Transverse Magnetic
TE	Transverse Electric
TEM	Transversal Electromagnetic
TRL	Through Reflect Line
V2V	Vehicle-to-Vehicle
UV	Ultra Violet

Wireless data transfer plays a dominant role in daily life with rapidly growing impact on nearly every area. From electrical tooth brushes sending messages about the cleaning process to high data rate transfer via mobile communication, wireless data transmission seems indispensable. Thereby the number of different communication standards that have to be integrated in one device is constantly increasing while the spaces for installation are often decreasing. Besides the rising amount of RF systems the functional requirements on a single system are increasing as well. Higher data rates, reliability and reduced latency times are the factors leading to a fairly challenging situation for the development of these components. Approaches to meet the requirements, like for example using Multiple Antenna Systems (MIMO) often lead to an additional increase of the space needed for the antenna integration.

As a consequence, the antenna systems often have to be integrated into the close surrounding of other antennas, circuit components and dielectric or metallic housing parts. In fact an antenna cannot be seen as one single element anymore. It has to be seen as one part of an overall system or from the opposite perspective: The integration space becomes part of the antenna and has to be considered and adapted within the design specifications of the application. The objective of utilising an integration space as efficient as possible is one main idea behind 3D fabrication methods that are summarised under the term Moulded Interconnect Devices or most recently, Mechatronic Integrated Devices (MID).

The MID technology utilises 3D plastic parts as circuit or antenna carriers by selectively metallising the surfaces. This seems to be a suitable solution when faced with challenging integration situations. This is why the technology is more frequently used in different applications from DC circuitry to mobile devices antennas, operating in frequency ranges up to $f = 6$ GHz. The efficiency in terms of the utilisation of an integration space is achieved by adding an additional function to a given mechanical part. Combining a mechanical and electrical function requires a proceeding in the development process differing from that of a development using Printed Circuit Boards (PCBs). In the design

of a 3D substrate mechanical as well as the electrical requirements have to be considered. Moreover, the electric design has to be closely linked with the mechanical development.

Besides the aspects of the development the condition of the fabricated device may differ from that known from a fabrication using typical RF substrates. Adding an electromagnetic function to a metallised plastic part brings up the question of material properties. These are depending on the fabrication process as well as on the respective RF design. An RF system is typically designed using materials with well know properties over the whole operating frequency range. The materials used for MIDs are typically not developed focusing on RF applications. This also applies to the characteristic data provided by the manufacturer of these materials. To use the possibilities of 3D manufacturing for RF devices this gap between manufacturing and RF development has to be closed. These requirements define the main topic of this work: The evaluation of the MID fabrication method, Laser Direct Structuring (LDS), for RF applications ranging up to 70 GHz.

1.1 State of the Art

The Laser Direct Structuring process is based on an injection-moulded plastic part made of plastic filled with an additive that allows for a selective laser activation. These activated areas can be metallised by electroless plating, subsequently. The LDS process is already used for RF device fabrication. In the consumer market, for example, several series applications are produced with LDS technology covering the frequency range up to $f = 6$ GHz [1]. These applications often utilise only one type of material leading to the situation that only these materials are characterised concerning their dielectric properties and only in the specific operating frequency range.

A scientific investigation of the dielectric properties of the LDS material Vectra E840i is found in [2], limited to the frequency range up to $f = 2$ GHz and without consideration of the anisotropy of the material. Besides that, a detailed characterisation of the MID material Pocan DP T7140 LDS (Lanxess AG) is described in [3]. The frequency range covered is $f = 1$ GHz up to $f = 12$ GHz. There are a various types of LDS capable thermoplastics available that meet different mechanical and electrical requirements. Compared to typical RF laminates these materials have special properties e.g. due to a filling with mineral or glass fibres leading to inhomogeneity and anisotropy of the material.

These materials are currently not characterised concerning their RF properties. A further aspect of 3D MID fabricated parts is the applied metallisation. The properties of the plated materials can be assumed to be different compared to commonly applied copper layers. For current LDS applications the influences of the metallisation are often not considered. There can be found an evaluation of LDS fabricated RF transmission line trying to extract the conductor losses in [4]. This evaluation is done for frequencies up to 1 GHz. There are principal investigations of the RF losses in a conductor carried out e.g. by Pytel et. al. in [5]. Huray et. al. developed a model to describe the RF losses of rough conductors using optical analysis of SEM photographs of copper surfaces like processed in PCB industry [6]. To evaluate if these approaches can be applied on the laser structured surface the exact surface structure has to be investigated.

Currently, the evaluation of the suitability of LDS fabrication for RF applications is carried out for a small number of materials and in a very limited frequency range.

Using the third dimension to develop antennas as it can be done with the 3D MID technology is not a new idea. Nevertheless, the developments are often oriented on the possibilities but also limitations of the fabrication processes currently established. A simple way to realise a 3D antenna is sheet metal bending as in [7] on the example of a broadband monopole or in [8] on the example of a dual band monopole for GSM and GPS. Another possibility to fabricate 3D shaped antennas is using metal foils that are bend on a 3D surface. This technique is limited to a surface that is bent only in one direction. Bending the foil on a surface that is shaped in two directions would cause wrinkles in the metal foil. Another method to realise 3D shaped antennas on plastic parts is metallising these plastic part with electroless or galvanic plating. Compared to a selective 3D metallisation with LDS these methods are typically limited to metallising the complete plastic surfaces, as discussed in [9] on the example of 3D printed horn antennas. 3D shaped antennas can also be realised using single planar substrate parts and putting these parts together to a 3D shape as discussed in [10] on the example of a monopole. This method seems only practicable for producing a very small quantity of antennas, like prototypes for example. Using a selective metallisation different research topics investigating 3D antenna design can be found in literature. Volume efficient antenna designs under the umbrella term conformal antennas are often used to adapt an antenna to a given volume. One antenna type frequently used in

this concern are microstrip antennas that are conformal integrated on surfaces. These antennas are often only slightly bend and mainly in one direction as e.g. described in [11] on the example of a conformal patch array or in [12]. An example design of a rectangular patch antenna array on a double bend substrate can be found in [13]. Wu et. al. use a slightly double curved surface for a 4x4 array with the result that the single antenna elements applied on this substrate are only slightly 3D shaped. This leads the author to the assumption that the 3D shaping has only a slight influence on the antenna performance. A first realisation of conformal patch antennas bend in one direction on LDS MID is described in [14]. Antenna concepts that are based on 3D LDS technology addressing mobile communication antennas for cellphones can be found in [15] and [16]. These examples use linear structures that are only slightly shaped in three dimensions due to the limitations of the installation space.

Current research activities on antenna development show an increasing usage of 3D fabrication possibilities. The design space used is often very limited.

1.2 Objectives

Based on the state of the art described in the last Section, the main objectives of the following work are:

- Evaluation of 3D manufacturing for RF applications with operating frequencies up to 70 GHz focusing on the LDS process.
- Deriving the main influencing factors for an optimisation of the LDS process parameters for RF devices
- Developing suitable design approaches for RF systems, especially antennas, using the design scope of 3D fabrication methods focused on the efficiency of the development and fabrication process
- Development, realisation and characterisation of different antennas and system design concepts on the basis of a vehicular installation environment.
- Development, realisation, characterisation of antenna and system design concepts independent of an underlying installation space using the 3D design scope to influence the RF system characteristics.

The antenna approaches and prototypes within this work are developed for an fabrication with the LDS method. Nevertheless, a large proportion of the results obtained can be applied on other 3D MID fabrication methods.

1.3 Outline

This work is divided in 6 Chapters starting with an introduction in Chapter 1.

Chapter 2 starts with a detailed technological evaluation as the basis of a reliable usage of the LDS technology for RF devices. Firstly, the aspects that have to be considered to allow for a reliable evaluation of a fabrication process are presented. The proceeding of the following evaluation is additionally derived. On the basis of this relevant geometric and mechanical parameters of LDS fabricated parts are described. Following, a detailed description of the LDS process is given. All relevant process steps are discussed bringing out the parameters that may be important concerning RF applications. Next, LDS capable substrate materials are evaluated using different measurement methods. The material specific characteristics are discussed considering the processing of the materials in an injection moulded process. Besides these prototyping materials of additive manufacturing methods are considered. Following, the metallisation applied in the LDS process is evaluated. On the basis of the mechanical investigations of the LDS specific surface curvature the influences on the RF properties are analysed. The principle findings are verified by measurements.

Chapter 3 deals with an antenna concept for vehicular integration covering the frequency range up to $f = 6$ GHz. Firstly, an antenna system is developed for the housing of a currently used roof antenna compartment. The antenna system is realised with LDS method and verified by measurements on system level during test drives in Munich, Germany. Hereafter, an analysis of possible installation spaces for an antenna system for mobile communication, WIFI and vehicle-to-vehicle (V2V) communication is carried out. On the basis of this, two different conformal monopole antennas are developed and fabricated with LDS technology. This MIMO antenna system is designed for an installation in the cowl of a convertible. The concept is verified by measurements of the single antenna elements and by EM simulations of the overall system in the vehicular integration space.

The usage of 3D fabrication for microstrip antennas is discussed in Chapter 4. Considering the concept of conformal antennas that can be found in literature, different possible configurations are described. Selected antenna configurations are evaluated by EM simulations. This includes microstrip antennas with a modulated surface as well as concepts for a circuit installation on or nearby the antenna. To verify the results obtained an active patch antenna for GNSS is developed. The system consisting of the antenna and a low noise amplifier (LNA) is realised with the LDS process.

Chapter 5 describes a further application of 3D fabrication; antennas that are fed by a dielectric filled waveguide. Different concepts of waveguide fed antennas that can be integrated into plastic parts are described. Two prototype antennas operating at $f = 24$ GHz and $f = 61$ GHz ISM band are fabricated and characterised. Subsequently, the concept is applied on a dielectric horn antenna which is integrated into a generic plastic frame. The antenna is designed to operate in $f = 60$ GHz WiGig band.

All results are summed up in Chapter 6.

Technological Evaluation of the Laser Direct Structuring

| 2

There are different methods available to fabricate 3D Molded Interconnect Devices (MIDs) distinguishing in the mechanical and electrical properties of the manufactured part [1]. Fig. 2.1 shows a schematic sketch of an 3D MID fabricated part. MIDs are typically based on a plastic substrate which is fabricated with injection moulding, two shot injection moulding or insert moulding. In case of injection moulding melted plastic material is extruded into a mould. By cooling down the plastic part is solidified. For insert moulding the same process is used with the only difference that metal parts are inserted in the mould additionally. In doing so e.g. conducting paths, contact pins or clips can be moulded in the plastic part. For two-shot injection moulding (2K) two different materials are processed. These materials can be two different plastic materials but also a plateable material. This allows for a realisation of 3D circuit pattern on the plastic surface.

In the past years more and more additive fabrication methods, better known as 3D printing techniques, are used. This is for example fused deposition modelling (FDM), selective laser sintering (SLS) or stereolithography (SLA). These techniques provide the advantage that small numbers can be fabricated cost efficiently, like for prototyping or small series. For FDM a plastic filament is melted to built up the 3D plastic part. In the SLS process, the raw material is a powder. The powder is applied in layers and sintered with a laser in the areas the fabricated part should be build. The sintering solidifies the raw materials. The raw material can e.g. be plastic, ceramic or metal powder. SLA is a process in which a photosensitive liquid resin is solidified by a Ultraviolet (UV) laser in the areas in which the solid structure is to be realised. All these processes are based on special raw materials whose RF properties may significantly depend on the manufacturing process.

The technique that can be used for metallisation varies depending on the manufacturing of the plastic part. With two-shot injection moulding and insert moulding, the areas to be metallised are specified during the design of the plastic part or even realised in conjunction with the plastic part. For injection moulded

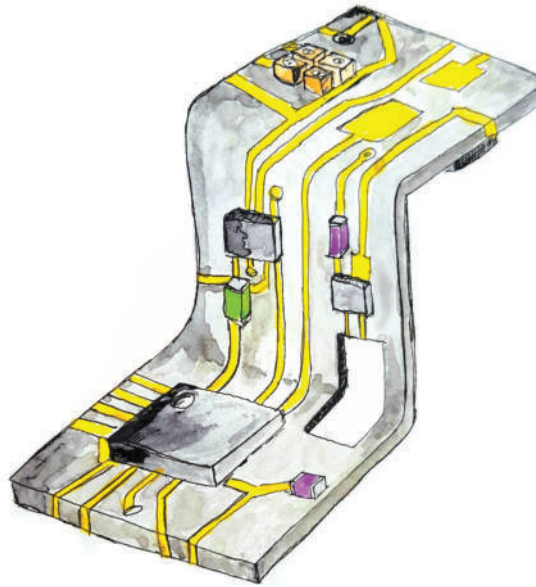


Figure 2.1 Schematic sketch of a Molded interconnect device - MID

and 3D printed plastic parts, different printing processes based on metal inks can be used. One example for metal printing is the aerosol-jet process. The 3D plastic surface is metallised with metal ink using an aerosol as carrier. There are different metal inks available distinguishing in their electric and mechanical properties [17]. Another way to apply a metal layer on plastic parts is ink-jet printing [18]. Besides these, a further additive metallisation method is the Laser Direct Structuring (LDS) process. On the basis of an injection-molded plastic part made of an LDS-capable material, the surfaces to be metallised are activated by a laser. Afterwards the activated areas can be metallised in a catalytic/electroless plating process.

The LDS technology is a process to manufacture MIDs, which is already used in various large-scale productions. The RF devices currently fabricated cover operating frequencies up to $f = 6$ GHz. These applications are found e.g. in the consumer market, where LDS fabricated antennas are integrated in laptops, tablets or smartphones. Currently, the RF properties of the LDS materials are often evaluated in the operating frequency ranges covered by and solely for the plastic material used in the application.

To use the 3D LDS technology for future RF applications ranging up to the millimetre waves, the suitability of LDS technology must be verified in general. This includes the evaluation of the complex permittivity of the LDS capable materials. Furthermore, it can be expected that the applied LDS metallisation will

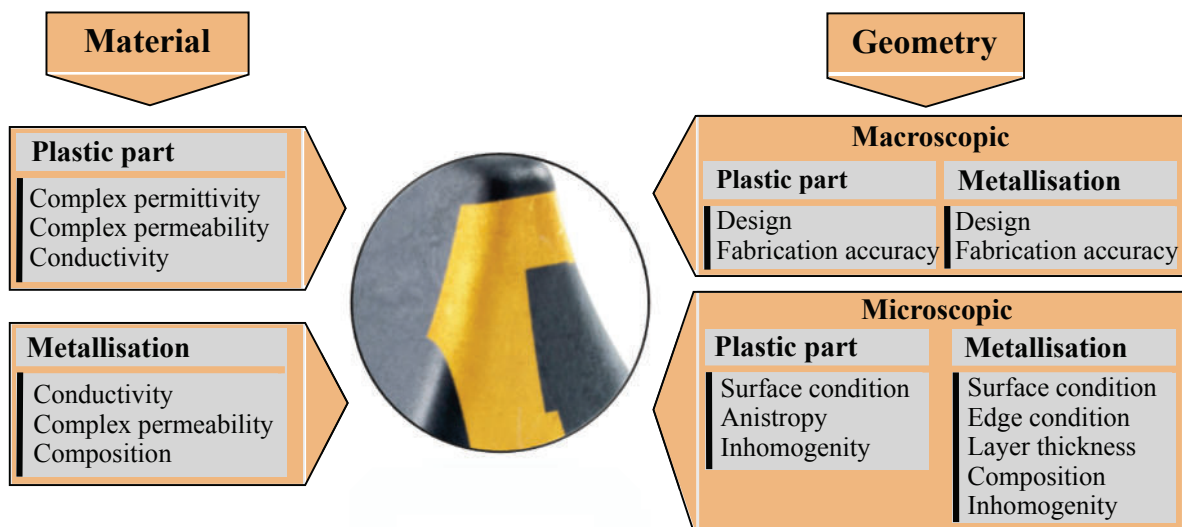


Figure 2.2 Aspects influencing the electromagnetic behaviour of a LDS fabricated structure

considerably influence the properties of a RF device with increasing operating frequencies. In particular, the surface quality of the LDS metallisation differs significantly from that of an RF substrate fabricated with a typical manufacturing process.

In the following Sections the RF characteristics of LDS manufactured parts are evaluated for operating frequencies ranging from $f = 0.1$ GHz up to $f = 70$ GHz.

2.1 Fabrication of RF Devices

In order to evaluate a manufacturing process such as the LDS process for RF applications, a systematic analysis of the influencing parameters must be carried out. Based thereon, the investigation can be divided into different aspects to ensure that they are evaluated separately or as needed for the development process. The phenomenal effects of electromagnetic fields are defined by Maxwell's equations as they are defined by James Clark Maxwell. These formulations are valid to describe the relation of electric and magnetic fields, current- and charge densities [19]. The boundary conditions are defined by the surrounding media and its spacial arrangement. This description of the relations of the field vectors and current and charge densities can be used to develop structures that allow for guiding, radiating or shielding electromagnetic waves. In different technical

applications this is used to process, transmit and receive information. Maxwell's equations for linear, isotropic and homogeneous materials with a harmonic time dependency are defined as:

$$\nabla \times \mathbf{H} = j\omega\varepsilon\mathbf{E} + \sigma\mathbf{E} \quad (2.1)$$

$$\nabla \times \mathbf{E} = -j\omega\mu\mathbf{H} \quad (2.2)$$

$$\nabla \mathbf{E} = \frac{\rho}{\varepsilon} \quad (2.3)$$

$$\nabla \mathbf{H} = 0 \quad (2.4)$$

When evaluating the formulations, especially with regard to the boundary conditions, there is a dependence on three material constants, the complex permittivity ε , the complex permeability μ and the static electrical conductivity σ . This implies that these material parameters and the associated spatial arrangement of the material define the electromagnetic behaviour of a structure at a given frequency ω . When applying this to the evaluation of the LDS process with regard to RF device fabrication, the boundary condition of an LDS part must be defined in general.

An LDS-manufactured part usually consists of a plastic substrate, the applied metallisation and the assembled circuit parts. The spatial arrangement varies according to the specific application. Fig. 2.2 lists and categorises the different aspects that influence the RF properties of an LDS-manufactured component. It should be noted that these aspects cannot be characterised separately of each other and this may also be not expedient. When characterising a material, the sample will always have a certain shape and the raw material is processed in a specific way. In case of the LDS metallisation, a characterisation without the substrate would be impossible.

Starting with a description of the LDS process in the following Section the categories defined in Fig. 2.2 are applied on the evaluation of the RF properties of the LDS process in the following Sections.

2.2 The Laser Direct Structuring Process

The Laser Direct Structuring method, abbreviated as LDS, is a laser based process to selectively metallise 3D shaped surfaces of plastic parts in an additive procedure. The method is under patent of the LPKF Laser & Electronics AG. For several years different LDS large scale productions are implemented covering a wide range of applications. These range from DC circuit pattern and connectors to antennas and shielding elements. Concerning RF applications LDS is used e.g. to realise antennas for mobile communication in consumer devices like smart phones, laptops or tablets. The frequencies that are covered by these applications range up to 6 GHz. Those antennas or feeding structures are realised on the surfaces of plastic parts, like housings, covers or other mechanical parts. The metal layer is applied on the 3D plastic surface implementing an electromagnetic functionality efficiently into a given volume and onto an already existing part. To apply a metal layer on the surface of a plastic part with the LDS method several process steps are required. Fig. 2.3 shows these steps on the example of a generic antenna design.

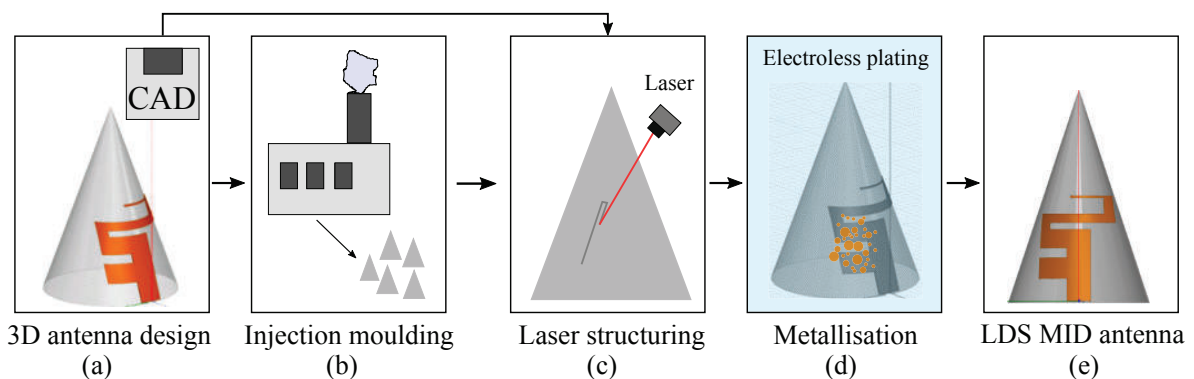


Figure 2.3 Process steps of the LDS technology

2.2.1 3D Antenna Design

The development of the LDS part, starts with the design of the plastic part. The shape is often determined or influenced by the geometry of an already existing plastic component or housing. Besides this, the plastic part can also be especially designed and optimised for an application. The plastic part to be used for the LDS process is typically fabricated as injection mould. The shape is mainly restricted by the design rules of the injection moulding process.

In addition, the design rules of the LDS process must already be taken into account during the development of the plastic part in order to avoid metallised surfaces that cannot be properly reached by the laser. In the case of large series production, the processing possibilities, e.g. handling of the plastic part, should also be taken into account when developing the plastic carrier.

The design of the plastic part can be done with typical mechanical computer-aided design (MCAD) tools like e.g. SOLIDWORKS, CATIA. In case of the development of an RF device there are electromagnetic (EM) simulation tools, like e.g. ANSYS HFSS, CST Microwave Studio, FEKO or EMPIRE XPU used to construct and optimise RF structures prior to its realisation. These programs provide a 3D CAD kernel that allows 3D structures to be constructed, but often with certain limitations in design scope and manageability compared to MCAD software. The advantage of a construction using EM field simulation software is that the plastic parts can be parametrised. Nevertheless, for more complex mechanical structures the design of the substrate using EM field simulation software is often not possible. In these cases a MCAD tool can be used. Afterwards, the CAD data can be imported in the EM simulation software

On the basis of the designed plastic part the metal pattern that should be applied on the surface can be developed. In case of a simple circuit pattern this can be done using MCAD tools. For more complex structures there are tools available combining electronic and mechanical CAD possibilities like e.g. MIDCAD or NEXTRA MID. As already mentioned, in case of an RF structure there is often an additional EM modelling required. This is done in a EM simulation software or in a circuit designer, e.g. Agilent ADS, for an RF circuit. Due to the fact that for these simulations parameter variations are typically used, the layout needs to be developed in the specific software. If it is not necessary to parameterise a structure, the metal pattern design can also be done in an MCAD tool. Afterwards, the developed RF structure can be imported in the field simulation software for an EM analyses.

2.2.2 Injection Moulding

Based on the CAD design the plastic part can be fabricated. This is typically done by injection moulding. The substrate materials used are thermoplastic or duroplastic materials that are filled with a mixed metal oxide that is dissolved or fine dispensed in the plastic raw material [1]. This can e.g be a chelate complex of a precious metal (e.g. palladium (Pd²⁺) or copper (Cu²⁺)) as described

in [20]. This metal complex is non-conductive. The chemical combination of plastic material and the special filler is modifiable by a high energy laser beam. The activation allows for a deposition of metal on the activated areas in a catalytic process. There are also LDS-capable plastics that can be processed with additive manufacturing technology, for instance FDM. In addition, substrates produced with additive manufacturing which do not consist of LDS-capable material can be coated with the LDS additive (LPKF ProtoPaint). This could be used, for example, for an initial test of the LDS process on an existing plastic part or for rapid prototyping and small series.

2.2.3 Laser Structuring

After the mechanical and electrical design and the manufacturing of the plastic part, the laser structuring is done. The geometry of the plastic part and the metal layer are exported as a CAD dataset. For the laser structuring the CAD file is prepared in a software like e.g. LPKF CircuitPro 3D. The surfaces that should be structured are divided into single faces to be efficiently processed. The way the surfaces are split to be processed, the pattern these surfaces are structured and the order the laser beam scans the single areas influences the processing time on one hand. This is particularly important for large series in which the processing time is to be kept short. On the other hand, the specific requirements of an application can be taken into account when splitting the surfaces. For critical areas, e.g. bends close to 90° or electromagnetically critical parts such as thin lines or small gaps, the structuring process may be adapted to achieve an optimal result.

In addition to the three-dimensional structuring, the parameters of the laser beam can be modified to influence the subsequent plating process, which in turn influences the electrical and mechanical properties of the metal layer. Parameters that can be modified are e.g. the power of the laser, the pulse repetition rate, the scanning speed, the overlap of the lines structured or the laser inclination angle (α). Some of these parameters generally need to be modified depending on the plastic material used. Nevertheless, these values can be varied within limits for a specific material. The surface condition of structured surfaces on the plastic substrate, but also the surface condition and material properties of the metal layer can be influenced. This will also have an impact on the mechanical characteristics of the metal layers, for instance the adhesive strength.

During the structuring process, the pulsed laser beam scans the surface and



Figure 2.4 Plastic part in different LDS processing steps - SLA part (only for LPKF ProtoPaint), injection moulded or ProtoPaint SLA part, laser structured part, metallized with LDS copper and metallised with surface finish (NiP/Au)

activates and exposes the mixed metal oxide on and in a small zone within the plastic. The roughened surface is required to cause a strong bond between the metal layer and the plastic. During laser structuring, the ablated particles are partially spread over the surface of the structured part. These activated particles can lead to an undesired deposition of metal in the plating process on the surfaces that are not structured. To avoid this a proper cleaning of the structured part has to be carried out subsequent to the laser structuring. This is especially important for RF structures with small gaps like e.g. coplanar waveguides. The particles spread in the structuring process may lead to small, sometimes nearly invisible metal bridges in the gaps. This will lead to a defective function.

2.2.4 Plating

After the cleaning, the structured plastic part can be metallised in the electroless plating process (Fig.2.3 c). Depending on the plastic used, a first layer of catalytic copper strike is deposited. This first layer is intended to build a strong contact between the metal layer and the plastic surface [21]. Following on the strike layer, a copper layer, with a typical thickness of about $h_{\text{layer}} = 7 \mu\text{m}$ to $h_{\text{layer}} = 10 \mu\text{m}$, is deposited in a further catalytic process. Some LDS materials are coated without the strike copper layer and the entire copper layer is built up in a single catalytic process.

On the basis of the copper layer different, electrolytic or catalytic plated, surface finishes are available. The currently (2019) used standard finish is an activation of the copper surfaces with palladium (Pd) covered by a nickel/phosphorus (NiP) layer in various phosphorus concentrations which is covered with immersion gold (iAu), abbreviated as ENIG [22]. Depending on the application also other electroless plated surface finishes can be applied e.g. immersion silver (iAg). In

addition to electroless plating, electroplating can also be used. This could be done, for example, by an additional layer of galvanic copper in order to achieve higher layer thicknesses. This can e.g. be used to increase the current carrying capacity of the conductor in case of a DC application. Another reason for using higher layer thicknesses is the aspect of thermal cooling, which is particularly important in applications with high power.

Besides the protection of the copper surfaces against oxidation, the surface finishes influence the electric and surface properties. How the plating influences the metal layer systems concerning RF applications is further evaluated in Sec. 2.5. Thereby the available LDS metal compounds are considered and typical electromagnetic and mechanical properties are described. Subsequent to the plating the 3D LDS substrate can be assembled in state-of-the-art surface mounted technology (SMT) processes by applying low or high temperature soldering methods, depending on the plastic resin used.

2.3 Fabrication Accuracy and Surface Condition

The geometric form of a RF device defines the electromagnetic characteristic of a RF device according to Maxwell's equations. In the development of a RF device, materials such as dielectrics and metallic structures are arranged in such a way that the required electromagnetic characteristics are achieved. Realising such a structure under ideal conditions would mean that all geometric dimensions exactly match the underlying model. In this case a RF device will provide the characteristics intended. Manufacturing under realistic conditions means that aspects like surface condition, resolution or fabrication accuracy have to be considered. This variances in the fabrication process leads to deviations from the RF characteristics designed. The influences of these variances will typically grow with the operating frequency. In order to take these inaccuracies into account in the development of a device, they must be evaluated with regard to the variable process parameters and parameters that can be intentionally influenced.

A LDS part consists of a plastic substrate whose surface condition is determined by the plastic material and the processing of the raw material. Typically, it will be an injection moulded part. The resulting surface condition is influenced by the injection mould and the plastic material. The surface condition of the injection moulded part used for the LDS process can be regarded as perfectly flat, taking into account the frequency ranges addressed in this thesis. This does

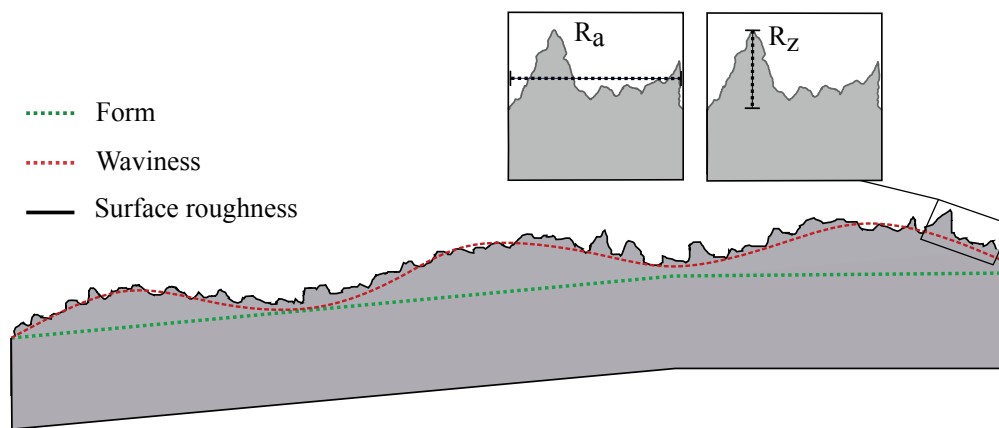


Figure 2.5 Descriptive parameters for rough surfaces

not apply to all additive manufactured plastic parts such as FDM parts. In this case, the substrate may have a surface condition that has a significant influence on the RF properties. This aspect will be further discussed in Sec. 2.4.

In addition to the plastic part, an LDS part consists of the metallisation layer deposited on the laser-structured surfaces. Structuring the plastic with the laser causes a micro rough surface that ensures a proper adhesive strength of the metallisation. Consequently, the surface roughness of the plastic part after laser structuring will differ from that of the injection moulded part. The surface quality of the metallisation on the external, visible surface and on the edges of the metallised areas is influenced by the plating as well as structuring process.

The surface condition is typically described by roughness values [23]. Fig. 2.5 depicts the definition that is frequently used to describe a rough surface. The surface profile is split up into roughness, waviness and form. In doing so the surface shape that is intended due to functional reasons can be extracted. The evaluation of the surface can be done as profile roughness measuring the profile along one line. Another common method is the characterisation of the surface over an area often described as areal roughness.

Different values are used for the qualitative description of the surface condition. One value frequently specified for LDS fabricated parts is R_a . R_a is the arithmetic mean value of the surfaces measured profile (peaks and valleys) over a line with the length L .

$$R_a = \frac{1}{L} \int_0^L |z(x)| dx \quad (2.5)$$

In addition to the arithmetic mean, the maximum peak-to-valley height measured over the sampling length L is often used, symbolised as R_z . Both values can also be evaluated over an area as areal roughness. These parameters are denoted with S . Analogous to Eq. 2.5 S_a is derived by calculating the integral over an area. S_z denotes the maximum peak-to-valley value in the area analysed.

In terms of the RF properties of a conductor, roughness leads to additional losses compared to a smooth conductor. A further aspect influenced by the surface condition of a conductor is passive intermodulation (PIM) causing non-linearity effects for high-power signals as e.g. described in [24]. PIM is not considered in this work, since for all applications discussed PIM can not occur. Depending on the field distribution, the effective surface in terms of surface condition can be the surface connected to the plastic or the external visible surface. Consequently, the roughness has to be evaluated for both surfaces. Furthermore, the filtering that splits up the surface profile into waviness, form and roughness has to be done considering the operating frequency range.

Fig. 2.6 shows the areal surface (Fig. 2.6a) and surface profile (Fig. 2.6b) analysis of a LDS plastic part for different production steps. The substrate material is Xantar LDS 3730. The surface analysis is performed using a Keyence 3D Measurement Macroscop VR-3000. As can be seen in the surface analysis, the laser structuring is reflected as grooves that are aligned with the direction in which the laser has scanned the surface (arrows). These grooves vary in depth, which is mainly influenced by the laser power, the pulse repetition rate and the scanning speed. The surface profile shows considerable differences for an evaluation in the direction of laser structuring or transverse to it (Fig. 2.6b). This leads to the assumption that the same applies to the associated RF properties. This aspect is further investigated and discussed in Section 2.5.

The roughness values of different LDS-manufactured samples are evaluated according to the definitions described above. The results are listed in Tab. 2.1. For comparison, the roughness of a Rogers 4003C substrate which is metallised with a rolled copper layer is analysed and shown in Tab. 2.1. The LDS sample with standard LDS metallisation (Cu/NiP/Au) shows the highest surface roughness with $S_a = 14.4 \mu\text{m}$. The same substrate material that is metallised with copper has a areal roughness of $S_a = 6.1 \mu\text{m}$, while the sample that is only laser structured

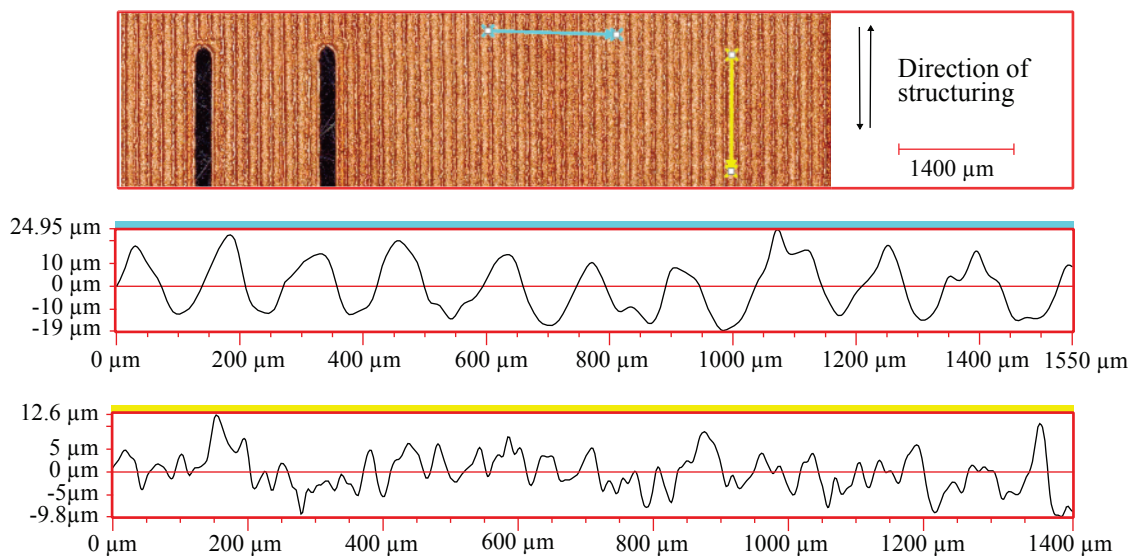
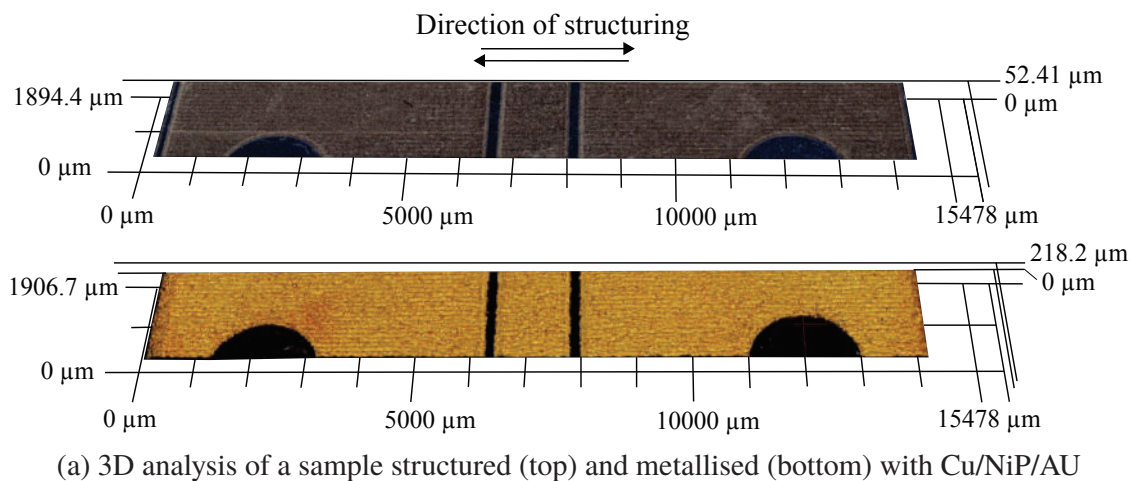


Figure 2.6 Surface analysis of a LDS fabricated part

has a roughness of $S_a = 2.8 \mu\text{m}$. For the sample, on liquid crystal polymer (LCP) Vectra E840i LDS, the roughness is only $S_a = 3.2 \mu\text{m}$. The test sample on Rogers 4003C has a surface roughness of $S_a = 2.4 \mu\text{m}$.

As can be seen, the roughness of the LDS samples show a strong variation depending on the substrate material used. This is inter alia due to changes in the laser parameters used for structuring different types of materials. As mentioned before, the laser parameters can additionally be varied for the same type of material. A variation influences the surface texture of the structured

Description	S_a	S_z	S_q	Area size
Xantar LDS 3730, structured	2.8 μm	53.7 μm	3.7 μm	0.2 cm^2
Xantar LDS 3730, Cu/NiP/Au	11.2 μm	149.9 μm	14.4 μm	0.1 cm^2
Xantar LDS 3730, Cu	4.1 μm	93.2 μm	6.1 μm	0.1 cm^2
Vectra E840i LDS, Cu	3.2 μm	83.3 μm	5.2 μm	0.085 cm^2
Rogers 4003, Cu (rolled)	2.4 μm	73.6 μm	4.5 μm	0.02 cm^2
Description	R_a	R_z	R_q	Line length
Xantar LDS 3730, Cu, measured in line	4.66 μm	35.41 μm	5.6 μm	2222.74 μm
Xantar LDS 3730, Cu, measured transverse	9.85 μm	46.43 μm	11.40 μm	2249.52 μm

Table 2.1 Evaluated surface roughness of different LDS samples

sample, which in turn influences the subsequent plating process. In this way, mechanical properties such as the adhesive strength can be optimised. Since the variation of the laser parameters influences the roughness, this indicates that the conductor losses can also be influenced. The measured profile roughness in the direction of structuring and transverse to it shows that the roughness of LDS samples is strongly anisotropic. This indicates that an additional optimisation can be achieved by considering the direction of structuring for a RF device. The roughness values for the sample on LCP indicate that the roughness of metallised LDS samples can be in a similar range to that of a rolled copper layer, depending on the material of the substrate and corresponding laser parameters. Besides the surface finish the fabrication accuracy of the LDS fabricated part will influence the RF behaviour. The geometric dimensions can be separated into the shape that is intentionally developed to achieve the electromagnetic behaviour and the deviations of this structure due to fabrication inaccuracies. The aspect last-mentioned is unintended and influenced by the fabrication process. Dimensional deviations of the injection moulded part are usually specified by the manufacturer. These deviations may result e.g. from inaccuracies in the injection mould or from shrinkage of the plastic material in the process. Inaccuracies of the applied metallisation result from the inaccuracy of laser structuring process. Today's (2018) LDS laser can achieve an position accuracy

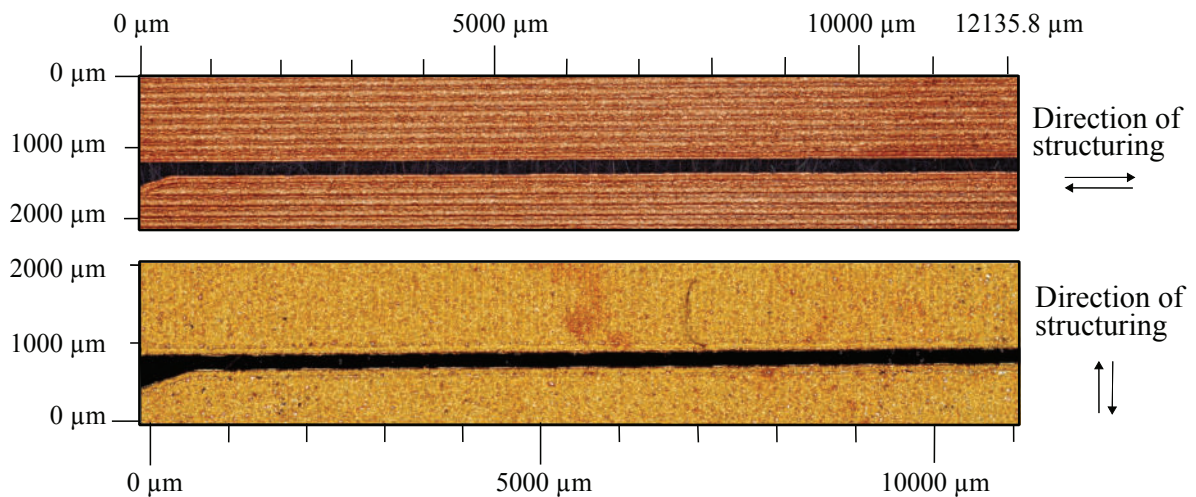


Figure 2.7 Edges of LDS fabricated coplanar waveguides that is structured in line (top) and transverse (bottom)

of $\Delta_{\text{pos}} = \pm 25 \mu\text{m}$ in a calibrated 3D scan volume. This value describes the accuracy the laser can reach one position in a 3D volume. The repeatability accuracy is about $\Delta_{\text{rep}} = \pm 10 \mu\text{m}$ describing the exactness the laser can reach one position in calibrated scan area again. The current processable resolution is a line and space width of $w = 75 \mu\text{m}$ and $g = 75 \mu\text{m}$ [AF4]. The inaccuracy of the positioning results in a misalignment of the entire layout, which is structured on the surface. How this influences the RF characteristics mainly depends on the electromagnetic design and the operation frequency. The inaccuracy in terms of the repeatability can e.g. lead to a variation of the line or gap width. In case of a transmission line, such variations lead to a change of the line impedance. In addition to the inaccuracy of the dimensions of the metal layer due to laser structuring, the catalytic metallisation process leads to a varying edge profile. Since these variations are based on the same mechanisms that cause the surface texture, it is called line edge roughness (LER). The edges of a coplanar waveguide are shown in Fig. 2.7 for a metallised sample, which is structured in the direction of wave propagation (top) and transverse to it (bottom). The sample structured transverse shows a higher line edge roughness due to the laser structuring. When scanning the surface, the laser is stopped at the edge and then changes direction. Due to the shape of the laser spot, the resulting edge has a wave-shaped structure. The sample that is structured in line with the edges has a smoother edge curvature. In this case, the laser scans the edge in a line.

In addition to electrical or electromagnetic functionality, the metallised LDS substrate must fulfil a mechanical function. This should be considered from

the beginning of the development process. When developing antennas to be manufactured with the LDS process, the substrate must be selected in such a way that it is suitable for the antenna application, but also fulfils the respective mechanical requirements. The requirements for the mechanical properties vary depending on the installation space and the environmental conditions associated with it. For most applications, the environmental and mechanical requirements on the plastics are defined by standards. In addition, the electromagnetic requirements are standardised and defined in detail in a specification sheet. As for non-LDS thermoplastics, data sheets containing the common mechanical properties such as temperature stability and glass transition temperature are available. In most cases the basic thermoplastics are already used in various areas of application, so that experience with these plastics is already available. The decision as to which substrate material can be used and how it can be coated to meet the mechanical and electrical requirements of an application must be made in order to find a balance between both aspects.

The significant findings of this Section are:

- Laser structuring generates a grooved surface in the direction in which a sample is structured. This results in a surface with a different surface structure depending on the direction of observation.
- The roughness values for different LDS samples show a strong variation depending on the process parameters such as laser power, laser beam width, overlap and metallisation. With these parameters, the surface quality of an LDS sample can be optimised within certain limits.
- Structuring the edges of the areas to be metallised in line with the edges leads to a reduction of the line edge roughness.

2.4 RF Properties of LDS Substrate Materials

The 3D substrate is the mechanical carrier of an LDS manufactured component. The chemical structure of the carrier material influences the electromagnetic properties, in addition to the mechanical properties. As derived in Sec. 2.1 under consideration of Maxwell's equations (Eq. 2.1), the influences of materials on the electric and magnetic field or flow are defined by the material constants, the

complex permittivity ε , the complex permeability μ and the static conductivity σ . When developing an RF component, a precise knowledge of these values is required in order to describe the behaviour of a structure prior to its realisation. To determine the material properties of LDS plastics, it is necessary to consider the main influence mechanisms in the manufacturing process and the chemical structure of the materials in order to select an appropriate measuring technique and sample preparation.

The complex dielectric constant ε is a material characteristic that describes the interaction of an electric field with a material. The complex dielectric constant for isotropic materials is defined as:

$$\varepsilon = \varepsilon_0 \varepsilon_r = \varepsilon' - j\varepsilon'' \quad (2.6)$$

and depends on chemical structure of a material, frequency and temperature [23]. For an anisotropic material, the dielectric constant is additionally dependent on the direction of the electric field vector \mathbf{E} . For these materials, ε and ε_r in Eq. 2.6 becomes a tensor. ε_0 defines the dielectric constant of free space ($\varepsilon_0 = 8.854 \cdot 10^{-12}$), while the relative dielectric constant ε_r is defined as the ratio of complex dielectric constant to the dielectric constant of free space. The relative dielectric constant ε'_r denotes the real part of the dielectric constant, while the loss tangent, referred to as $\tan \delta$, describes the ratio of the imaginary part and the real part of the relative dielectric constant. The relative dielectric constant, dielectric constant and loss tangent are dimensionless.

The complex permittivity dependency over frequency is influenced by different effects that are related to the chemical structure of the material. Within this work LDS plastics are characterised in a frequency range from $f = 0.1$ GHz to $f = 70$ GHz. In this range, the frequency response is determined by dielectric relaxation, which describes the reorientation of electrical dipoles in an applied electric field. There are different models that describe the behaviour of the dielectric constant over frequency due to this effect. For polar materials with a single characteristic relaxation frequency f_r the model of Debye describes the complex permittivity behaviour over frequency due to these polarisation effects [25]. This model is modified by Cole and Cole considering one or more types of polarisation [26]. Both models describe qualitatively the same frequency behaviour of the complex permittivity. For low frequencies starting with a static value of ε_r , which decreases to a smaller static value for high frequencies. For composite dielectrics, e.g. plastics filled with glass fibres

or mineral particles, the frequency behaviour of the complex permittivity is determined by both materials.

Besides the dielectric relaxations there can occur dielectric resonances [23]. For homogeneous and linear materials no dielectric resonance is to be expected in the frequency ranges examined in this work. However, dielectric resonances can occur in composites due to the filler particles. The resonance frequency is dependent on the complex permittivity of filler and basis material and the size of the filler particles which act as dielectric resonators [27]. In addition to resonances caused by filler particles, the measurement setup and the sample size can cause a resonance which can be seen in the frequency response of the measured complex permittivity. It has to be considered that this is not a material characteristic.

Due to the frequency dependence of the dielectric constant, the operating frequency range to be covered by an application must be taken into account for the characterisation. In addition to the frequency, the complex dielectric constant depends on the environmental conditions in which a material is used. Humidity and temperature are the most important influencing factors for an LDS plastic in relation to an RF application. The plastics can adsorb water, depending on the humidity in which they are used. The rate of the water adsorption influences the complex permittivity considerably due to the fact that water has a high permittivity in the evaluated frequency range [27]. The water adsorption is specified in the material data sheet. The characterisation is carried out e.g. according to DIN EN ISO 62. Temperature changes influence the chemical state of a plastic. These different chemical states have a high impact on the mechanic as well as the electric properties of a material. The glass transition temperature is an important parameter that describes one of these changes. The glass transition defines the temperature at which a change in the mechanical properties from ductile to brittle occurs [28]. This may have a considerable influence on the dielectric constant of the plastic, but also on the geometric dimensions, e.g. the wall thickness. Within this work the effects of environmental influences are not considered. All measurements carried out in the following are obtained at room temperature ($T = 22\text{ C}^\circ$). In addition, all the materials investigated have a glass transition that is far above or below this temperature.

As a second material property, which determines the electromagnetic behaviour of a device according to Maxwell's equations (Equ. 2.4), the complex permeability μ describes the reaction of a material to an applied magnetic field and vice versa [19]. In analogy to the complex dielectric constant, relative permeability is often denoted as μ_r and defined as the ratio of complex permeability and

permeability of free space ($\mu_0 = 4\pi \times 10^{-7}$ H/m). For all LDS-capable dielectrics currently available, it can be assumed that $\mu_r = 1$. Consequently, this material property is not taken into account in this work.

The last material property to be considered is the static electrical conductivity (σ). Current (2019) LDS plastics filled with the organic metal complex and other fillers are non-conductive ($\sigma \rightarrow 0$). In order to achieve selective conductivity of LDS plastics, the surfaces must first be activated by laser and then plated in an electroless process.

2.4.1 Chemical and Physical Properties

LDS materials are typically thermoplastics or thermoset materials. In addition to the use of homogeneous materials, they are often reinforced with fillers such as glass, carbon or polymer fibres. A filling is often done to optimise mechanical properties such as stiffness and strength [28]. The filling leads to a structural anisotropy and inhomogeneity, which affects both mechanical and electromagnetic properties. The influence on the material properties of the base material depends on the degree of filling and the type of filler. The materials are typically processed in an injection mould and the fibre reinforcement is made discontinuously with short strands or balls. In the injection moulding process, the filler is aligned in relation to the flow direction of the mass. Consequently, the dielectric properties may vary for each plastic part.

In addition, this anisotropy leads to a dielectric constant which may vary over the different areas of a plastic part, depending on the wall thickness, the geometric shape and the injection moulding process. Nevertheless, a characterisation of the dielectric properties of such a composite material can be carried out considering the injection direction in the injection moulding process and using sample geometries with defined injection direction. The measurement is performed for each direction in which the electromagnetic field can penetrate the material based on a Cartesian coordinate system. Fig. 2.8 shows the definition used hereinafter to describe the orientation of the electromagnetic field and filler for anisotropic materials. Accordingly, the complex permittivity for an electromagnetic field penetration in x-direction is referred to as the dielectric value in x-direction ($\epsilon_{r,x}$). In this case, the filler particles are aligned with the electromagnetic field. For values in the y- and z-direction, the filler is aligned perpendicular to the penetrating electromagnetic field. The inhomogeneity can be neglected as long as the filler particles are very small compared to the wavelength. For higher

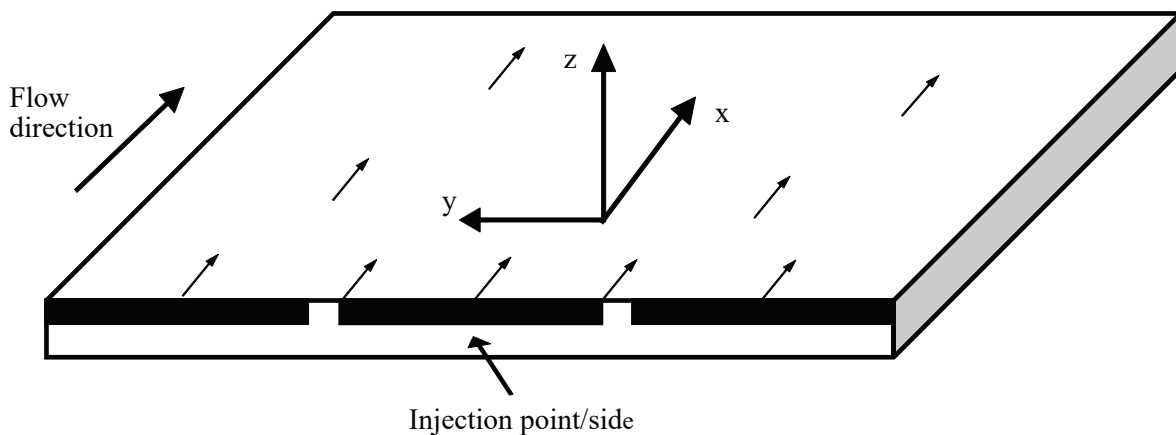
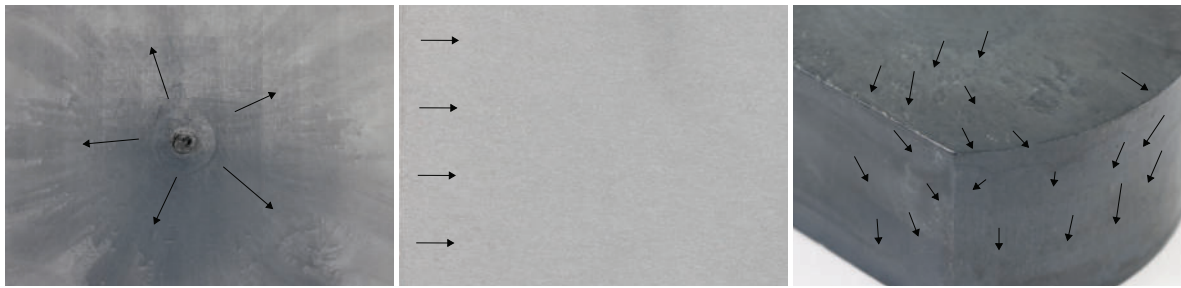


Figure 2.8 Underlying coordinate system for characterisation of anisotropic materials

frequencies, where the size of the filler is in the same range as the wavelength, resonances can be caused as it is described in the last Section. The LDS-capable materials also differ in that the mixed metal oxide filler is added. The filler can be assumed to be very small and evenly distributed. It does not cause anisotropy or inhomogeneity with respect to the frequency ranges considered here.

When developing an RF device with such a reinforced material, the direction of injection and the associated dielectric constant must be taken into account. The flow direction can be precisely simulated in injection molding simulation software such as Moldex3D or SIGMASOFT. A resulting dielectric constant can be calculated for certain areas. Depending on the complexity of the shape, the dimensions and positioning of the metallised surfaces and the operating frequency range, an effective dielectric constant can also be estimated approximately. This could be done by optical inspection of the surfaces and the flow direction. Particularly for injection molded parts with relatively thin walls, the flow direction and the orientation of the fillers can be assumed to be parallel to the surface. This simplifies the calculation, since only two orientations of the filling particles can occur.

As an example, Fig. 2.9a shows the picture of an injection-molded plastic plate with a height of $h = 1$ mm. The flow direction of the mineral-filled plastic (Vectra E840i LDS, Celanese GmbH) is clearly visible. This plate has an injection point in the middle of the plate. As a result, the flow direction is radial to the injection point. This may be critical for a dielectric material characterisation, as the properties should be measured with an exactly defined flow direction. Depending on the geometric dimensions of the samples that are required for material characterisation, this cannot be achieved with the plastic plate shown



(a) Injection point in the middle (b) Injection point on the edges (c) Thick plate with swirled filler

Figure 2.9 Injection moulded plate with mineral filler

in Fig. 2.9a. The measurement data obtained for such a sample correspond to a mixed orientation (x- and y-direction) of the filling particles. For a precise orientation of the filler, an injection should be made along one side of the sample plate. The injection should also be done over a wide range as shown in Fig. 2.9b. On this picture the flow direction is nearly not visible due to the straight alignment of the filler in the plastic sheet with a low height of $h = 1$ mm. For thick plastic sheets, the filler particles can be swirled at the edges of the plastic part, as shown in Fig. 2.9c. This can lead to a completely mixed orientation of the filler in some areas. The dielectric values measured in this area apply only to this particular structure. In order to achieve a valid material characterisation, such plastic parts can only be used in areas where the filler has a defined orientation.

In addition to the fabrication of the substrate with injection moulding, additive manufacturing processes such as FDM, SLA or SLS can be used. This could be done with LDS-capable materials using the FDM method. For other additive manufacturing processes, such as SLS or SLA, the LDS-compatible coating, LPKF ProtoPaint LDS, is available. The processing of a material with additive manufacturing methods can also lead to considerable anisotropy and inhomogeneity of the substrate. As an example, Fig. 2.10a shows a FDM part where the material is applied as small strings of molten plastic. Depending on the resolution this can be seen on the surface of the FDM part as for the part shown in Fig. 2.10a. The way the material is applied leads to varying dielectric properties. Besides the type of plastic material used, process parameters like the thickness of the string of molten material, the direction the material is applied and possible air inclusions are the influencing factors. Fig. 2.10 shows a close-up of a low-resolution FDM part. As can be seen, there are relatively

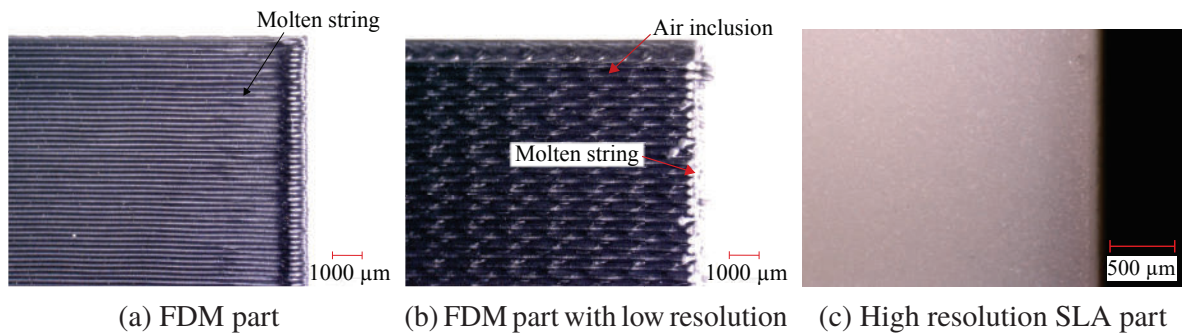


Figure 2.10 Surfaces of additive manufactured plastic parts

large air inclusions. When characterising the dielectric properties of such a material, only an approximate value can be determined, since a variation in the manufacturing process can lead to considerable differences in the structure of the sample. Fig. 2.10c shows a sample of a high-resolution SLA part. The material used is an epoxy resin. This part has a homogeneous structure without any air inclusions, which allows for a precise material characterisation. Anisotropy can also occur with other additive manufacturing methods than those shown above. In order to use these fabrication methods for RF substrates, this must be taken into account when characterising the dielectric properties and developing the RF structure.

2.4.2 Description of the Measurement Setup

There are several methods available for characterising the relative dielectric constant and the loss tangent, which have already been studied and published in detail. These methods differ in their physical principle, their accuracy and the required geometry of the test specimens. A detailed description of these measuring principles can be found e. g. in [27]. The measurement methods are typically classified based on their underlying electromagnetic principle. These are impedance based measurements, transmission based and resonance/standing wave based measurements. Besides the underlying electromagnetic principle of a specific measurement setup the direction the electromagnetic field penetrates the test sample varies. This is especially important for anisotropic materials. When investigating the dielectric properties of LDS plastics, production-specific aspects must be taken into account. These are e.g. the dimensions that can be manufactured and the processing of the raw material. The latter especially

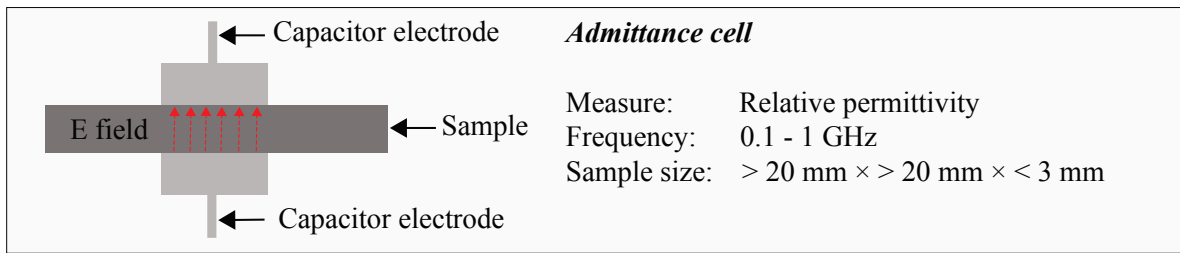
applies on composite materials.

In this work, four measurement configurations covering all three of these principles are used. Fig. 2.11a-c shows the measurement configurations used in this work and their specifications. As described in Section 2.4.1, the definition of the direction of the electric field is based on a Cartesian coordinate system. In this way, the measurements are carried out for an electrical field penetrating the sample in x-, y-, z-direction. The measurement configurations used cover a frequency range from $f = 0.1$ GHz to $f = 65$ GHz. For anisotropic materials, this frequency range may only apply to a certain direction of electromagnetic field penetration depending on the possibilities of the sample fabrication/preparation.

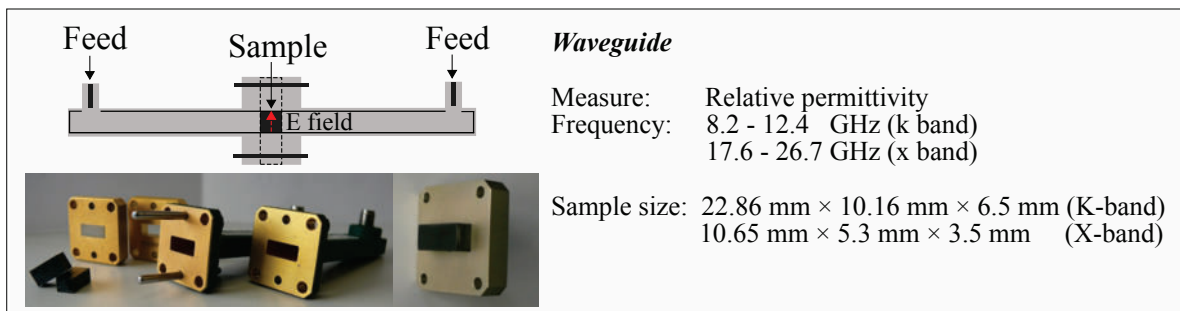
The first measuring instrument used is the commercial impedance analyser Agilent E4991A RF Impedance/Material Analyser and the 16453A Dielectric Material Test Fixture and material option (Fig. 2.11a). The measuring frequency ranges from $f = 0.1$ GHz to $f = 1$ GHz. A plastic plate is required as test sample. The plastic plate is fixed between two metal electrodes that form a capacitance. Depending on the dielectric constant of the material which is inserted between the electrodes, the complex impedance of the capacitance changes. In this way, the complex dielectric constant can be calculated taking into account the measuring device and the dimensions of test object. The electrical field penetrates the sample mainly perpendicular to its surface. Depending on the frequency, thickness of the sample and its dielectric constant, fringing fields are generated at the edges of the metal electrodes. This leads to an error in the measured values. The error tolerances are given in detail in the data sheet of the measurement device [29].

The transmission method used is a waveguide in the X- and K-band (Fig. 2.11b). The X-band covers frequencies from $f = 8.2$ GHz to $f = 12.4$ GHz, while the K-band waveguide operates from $f = 17.6$ GHz to $f = 26.7$ GHz. The rectangular waveguide is fed with its fundamental mode, which induces an electrical field aligned along the short side of the waveguide cross-section. The evaluation is performed according to [30] and is calculated using the method described in [31]. The samples are prepared as cuboids that are inserted into the rectangular waveguide. The dielectric constant can be calculated on the basis of a TRL calibration and the measurement of the transmission and reflection coefficient of the filled waveguide. The accuracy is influenced, among other things, by the sample, which has to be manufactured very precisely in order to fit into the waveguide cross-section without air gaps.

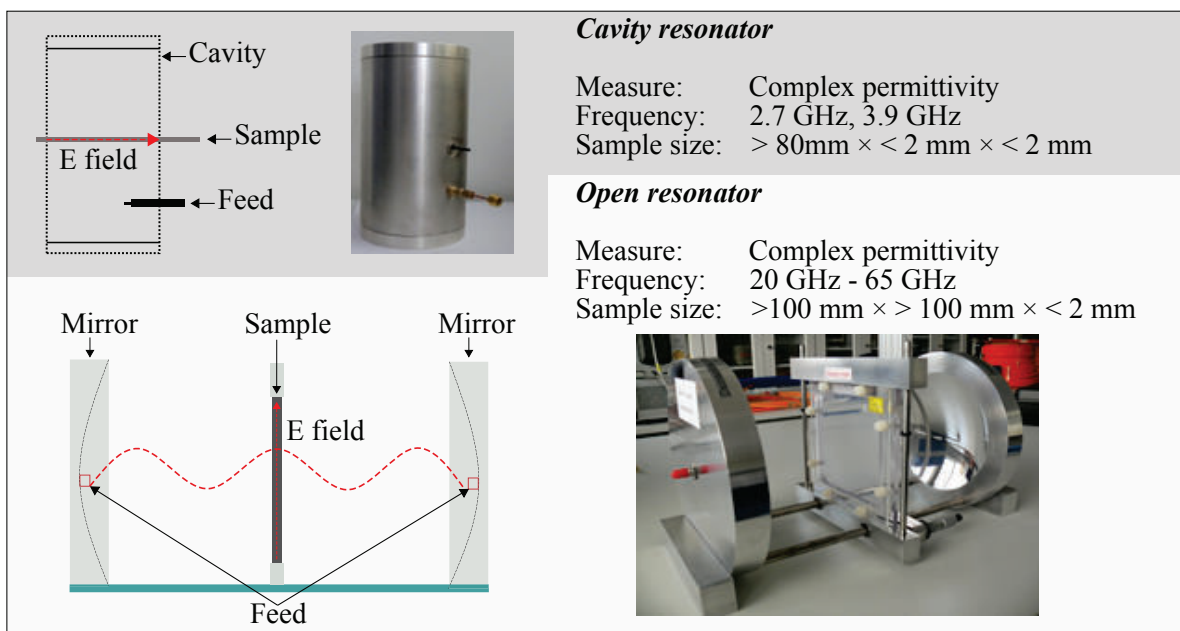
The third measurement technique is the resonator method as depicted in Fig. 2.11c. A cavity and a open resonator are used. The cavity resonator operates at



(a) Admittance method



(b) Waveguide method



(c) Resonator method

Figure 2.11 Dielectric material measurement setup used for characterisation of LDS plastic materials

$f = 2.67$ GHz which is the TE_{111} cavity resonance. The open resonator is operated at different resonances ranging from $f = 20$ GHz to $f = 65$ GHz. The cavity resonator measurements are evaluated according to [32]. The open resonator is evaluated using the commercial software provided by Damaskos, Inc. [33]. The complex dielectric constant can be calculated from the differences in resonance frequency and quality factor (Q-factor) for the loaded and unloaded resonator. For the cavity resonator, the samples are small rods with a cross-section of up to $w = h = 2$ mm and a length of about $l = 90$ mm. The rods are inserted through small holes at the side of the cylindrical cavity. The electric field is aligned parallel to the rod. The open resonator is loaded with thin plastic plates having an edge length of $w = l = 127.0$ mm. The sample is placed in the middle between two mirrors acting as reflector. The sample is aligned as accurately as possible. In doing so, the electric field in the plane of the sample is aligned vertically, parallel to the sample plate. The thickness of the plate or rod affects the accuracy of the resonator measurements. In order to achieve accurate measurements, the samples should be as thin as possible to minimise the disturbance of the field in the resonator. This applies in particular to lossy materials. In addition, the sample geometry should be well known. In case of the cavity, the width w and the high h influence the measurement result, while the length has no influence as long as the specimens are long enough to fit into the cavity. In the open resonator, the field is concentrated in the middle of the plastic plate. The accuracy of the edge length plays a minor role, while the thickness must be exactly known.

2.4.3 Dielectric Characterisation

The results described below are partly based on the publication [AF7]. Tab. 2.2 shows the LDS materials, which are characterised in the following, and their relevant properties. The materials are chosen in such a way that they cover a wide variety of available material types. This provides a representative overview of possible LDS materials that can be used for different RF applications. All materials are based on materials that are already used in industrial applications but which are not LDS-capable. The glass transition of all materials is above room temperature, so that this does not affect the dielectric constant. All test samples are produced by injection moulding as plates with a height of $h = 1.0$ mm to $h = 10.0$ mm. The dimensions in the x- and y-plane vary between $w_{\text{edge}} = 100$ mm and $w_{\text{edge}} = 120$ mm. Unless otherwise mentioned, all samples are injected at one

Name	Chemical Name	Filler	Anisotropy
Grilamid 1SVX-50H LDS	Polyamide (PA)	glass fibre	yes
Vectra E840i LDS	Liquid Crystal Polymer (LCP)	mineral	yes
VESTAMID HTplus M1033	Polyphthalamide (PPA)	glass fibre / mineral	yes
Xantar LDS 3720	Polycarbonate + Acrylonitrile Butadiene Styrene (PC/ABS)	no	no
Xantar LDS 3732	Polycarbonate (PC)	no	no

Table 2.2 Evaluated LDS materials with relevant characteristics

edge and with one to three injection points. For all manufactured test specimens, this ensures that the flowing direction can be assumed parallel to the plate surface. Based on these plastic plates, the suitable shape of the test specimens for the various measuring procedures are produced by milling. For anisotropic materials, this is done with an alignment defined by the flowing direction and thus the orientation of the filling materials. Unless otherwise specified, all measured values are given as arithmetic mean values of the measured quantity and the spread of the measured values as error bars.

2.4.3.1 Grilamid 1SVX-50H LDS

Grilamid 1SVX-50H LDS from EMS-Grivory is a black polyamide (PA) filled with glass fibres with 50% by weight. The glass fibres are short strand fibres with $l \approx 2$ mm in length. Due to the filling an anisotropy of the permittivity can be expected. Consequently, the sample preparation is done considering the flow direction. Grilamid 1SVX-50H LDS is a solderable material.

Admittance Cell

Due to the limitations of the sample geometry, an evaluation could only be carried out for an electrical field alignment in the z-direction, perpendicular to the glass fibers. Fig. 2.12 shows the measured arithmetic mean of the relative dielectric constant for 10 samples with a size of $w = l = 10$ mm and $h = 1$ mm.

As the admittance measurements do not allow to evaluate the loss tangent very exact these values are not considered.

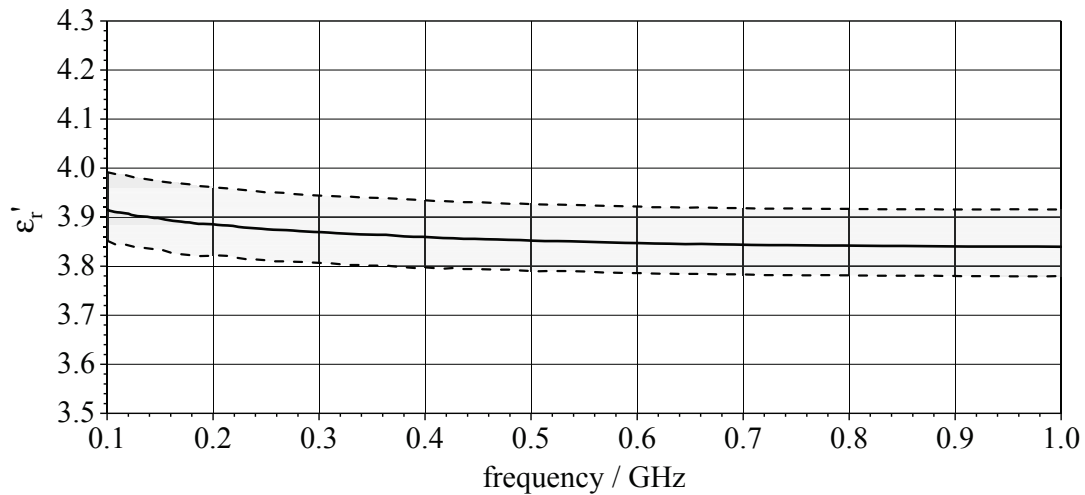


Figure 2.12 Relative permittivity of Grilamid 1SVX-50H LDS in z-direction measured with admittance method

Resonator

Both resonator methods allow for a measurement of the complex permittivity for a electric field aligned in y- and x direction with respect to the available sample geometry. For the cavity resonator the samples are rods with a length of $l = 100$ mm and cross section of $w = 1$ mm and $h = 1.5$ mm. The test samples used for open resonator measurements are plates with a height of $h = 1$ mm and an edge length of only $w = l = 100$ mm due to the fact that samples with larger edge length were not available. Fig. 2.13 shows the measured arithmetic mean value of relative permittivity and loss tangent for 6 samples.

Waveguide

There could not be performed valid measurements for Grilamid 1SVX-50H LDS with the waveguide methods. During the sample preparation in a milling machine, the material showed a very brittle behaviour causing small break off's on the edges of the test samples. These inaccuracies lead to high error tolerances

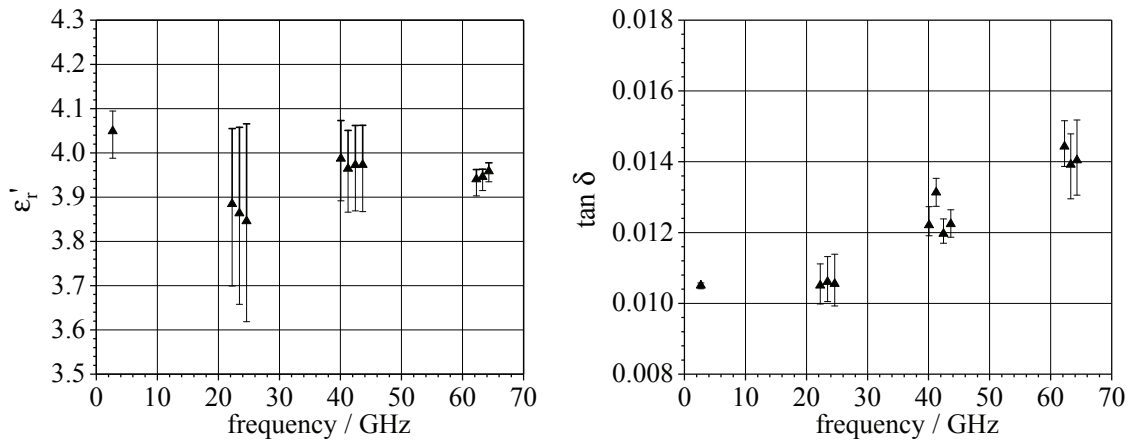


Figure 2.13 Complex permittivity of Grilamid 1SVX-50H LDS measured with the cavity - and open resonator in x-direction

in the measurements with the waveguide, so that these are not considered in this work.

Evaluation of Measured Results for Grilamid 1SVX-50H LDS

The measured values of the anisotropic LDS material Grilamid 1SVX-50H LDS show that the relative permittivity as well as the loss tangent are in a range as expected for this type of material [34]. The measured arithmetic mean of the relative permittivity at $f = 0.1$ GHz is $\epsilon'_{r,z} = 3.9$ decreasing down to $\epsilon'_{r,z} = 3.85$ at $f = 1$ GHz. These values are valid for an evaluation with the E-field aligned in z-direction.

The measured arithmetic mean values for an E-field alignment in x-direction at $f = 2.7$ GHz (cavity resonator) show a relative permittivity of $\epsilon'_{r,x} = 4.05$ and a loss tangent of $\tan \delta = 0.011$. At $f = 60$ GHz the measured values of the relative permittivity decrease down to $\epsilon'_{r,x} = 3.95$ and the loss tangent increases to $\tan \delta = 0.014$. The minimal and maximal evaluated values with open resonator show a spreading of the measured relative permittivity of about 10% at $f = 20$ GHz and 1.2% at $f = 60$ GHz.

No resonance effects due to the glass fibre filling could be observed in the evaluated frequency ranges. However, it should be noted that such effects can occur at certain frequencies in the millimetre wave range, so that this composite material appears less suitable as substrate material for these high frequency

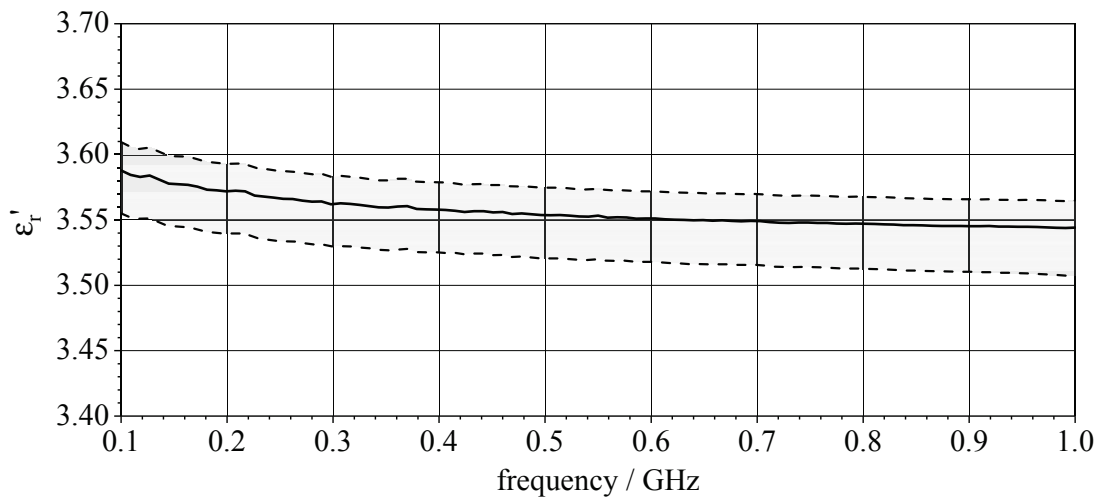


Figure 2.14 Relative permittivity of Vectra E840i LDS in z-direction measured with admittance method

ranges.

Comparing the values for each direction of E-field alignment shows that the overall anisotropy causes only a slight variation about 5% of the arithmetic mean of the relative permittivity. Compared to typical RF substrates Grilamid 1SVX-50H LDS has a relatively high dielectric loss tangent. Nevertheless, this may be acceptable, especially when the specific mechanical properties of this material are required.

2.4.3.2 Vectra E840i LDS

The liquid crystal polymer (LCP) Vectra E840i LDS from Celanese GmbH (former: Ticona GmbH) is a greyish, crystalline material with a mineral filling of about 40% per weight. Due to the filling an anisotropy of the permittivity can be expected. Consequently, the sample preparation is done considering the flow direction of the moulded plastic plates. This material is especially suitable for thin walled injection moulding and is solderable.

Admittance Cell

The admittance method is used only for electrical field alignment in the z-direction, perpendicular to the filler, due to limitations in the sample geometry.

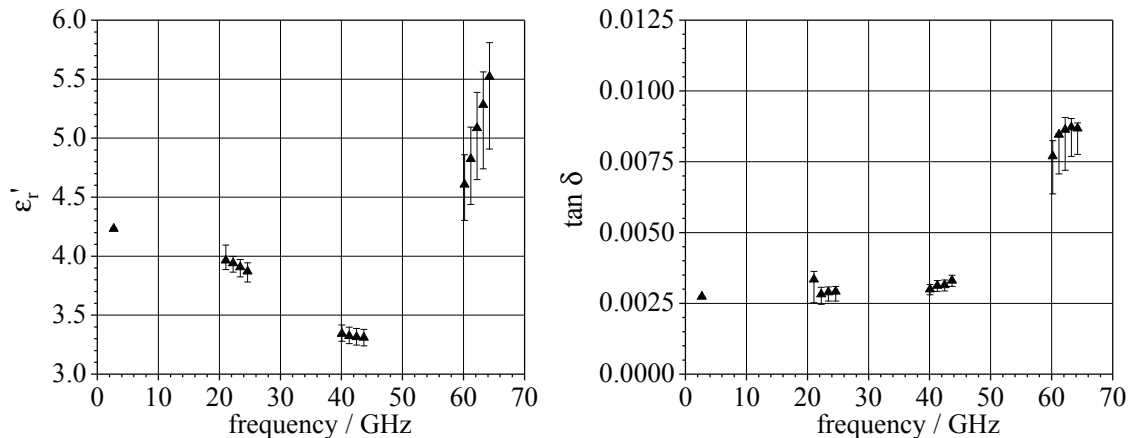


Figure 2.15 Complex dielectric constant of Vectra E840i LDS measured with the cavity - and open resonator for a mixture of x- and y-direction

Fig. 2.14 shows the measured arithmetic mean of the relative permittivity evaluated of 10 samples with a size of $w = l = 60$ mm and a height of $h = 1$ mm.

Resonator

The resonator based methods are used measuring the complex permittivity for a electric field aligned in x- and y-direction with respect to the available sample geometry. For cavity resonator the samples are thin rods with a length of $l = 80$ mm and cross section of $w = 1$ mm and $h = 2$ mm. The test samples used for open resonator are plates with a thickness of $h = 1$ mm and an edge length of only $l = 100$ mm due to the fact that samples with larger edge length were not available. The material samples are realised of injection moulded plastic plates with a size of $w = 100$ mm $l = 250$ mm and $h = 1$ mm with an injection point in the middle of the plate. This leads to a orientation of the filler that is not parallel to the edges of the sample in all areas as it is already shown in Fig. 2.9a. Especially, at the edges a mixed orientation of the filler occurs. The measured data obtained are consequently valid for a mixture of an electric field aligned in the y- and x-direction, but with a predominant orientation in the x-direction. Fig. 2.15 shows the measured arithmetic mean of the relative permittivity and loss tangent evaluated for 5 samples with both resonator methods.

Waveguide

There could not be performed valid measurements for Vectra E840i LDS with the waveguide methods. Due to limitations in the sample fabrication of this composite material, no samples with a sufficient thickness and a defined orientation of the filler were available.

Evaluation of Measured Results for Vectra E840i LDS

The measured values of the anisotropic LDS material Vectra E840i LDS show that the relative permittivity as well as the loss tangent are in a range as expected for this type of material. The material has a relative permittivity (arithmetic mean) of $\varepsilon'_{r,z} = 3.58$ at $f = 0.1$ GHz decreasing down to $\varepsilon'_{r,z} = 3.55$ at $f = 1$ GHz. These values are for an evaluation with the E-field aligned in z-direction.

The measurements for an E-field x-alignment at $f = 2.7$ GHz show a relative dielectric constant of $\varepsilon'_{r,x} = 4.25$ and a loss tangent of $\tan \delta_{r,x} = 0.0035$, both arithmetic averages. The differences in comparison with the values for the z-direction results show a high anisotropy for this material. This is also described in the product brochure provided by the manufacturer for the mechanical properties. The measured relative permittivity at $f = 20$ GHz is $\varepsilon'_{r,xy} = 3.9$ with a loss tangent of $\tan \delta_{r,xy} = 0.0035$ decreasing to $\varepsilon'_{r,xy} = 3.3$ and a loss tangent of $\tan \delta_{r,xy} = 0.004$ at $f = 40$ GHz. Between $f = 60$ GHz and $f = 65$ GHz the permittivity increases from $\varepsilon'_{r,xy} = 4.5$ to $\varepsilon'_{r,xy} = 5.5$ with a loss tangent increasing from $\tan \delta_{r,xy} = 0.007$ to $\tan \delta_{r,xy} = 0.009$. This may be an effect due to the filler of this composite material, as it is described in Sec. 2.4. The exact length of the filler particles of this material is unknown to the author, but the wavelength in the plastic at $f = 60$ GHz is approximately $\lambda_{\text{mat}} = 2.5$ mm. This is a length which is in a similar range to that of filler particles for plastics.

Vectra E840i LDS has a relatively low loss tangent comparable to typical RF substrates. This makes the material suitable for RF applications where low losses are required. Critical may be the high anisotropy of the material, especially for RF applications operating in higher frequency ranges. The anisotropy causes a variation of about 20% for an E-field alignment in z- and x-direction. In an injection moulding process the orientation of the filler may not be exactly predictable. Depending on the operating frequency range and geometric structure, this can lead to more or less pronounced fluctuations in the RF characteristics. As a further aspect, the structure of the composite material

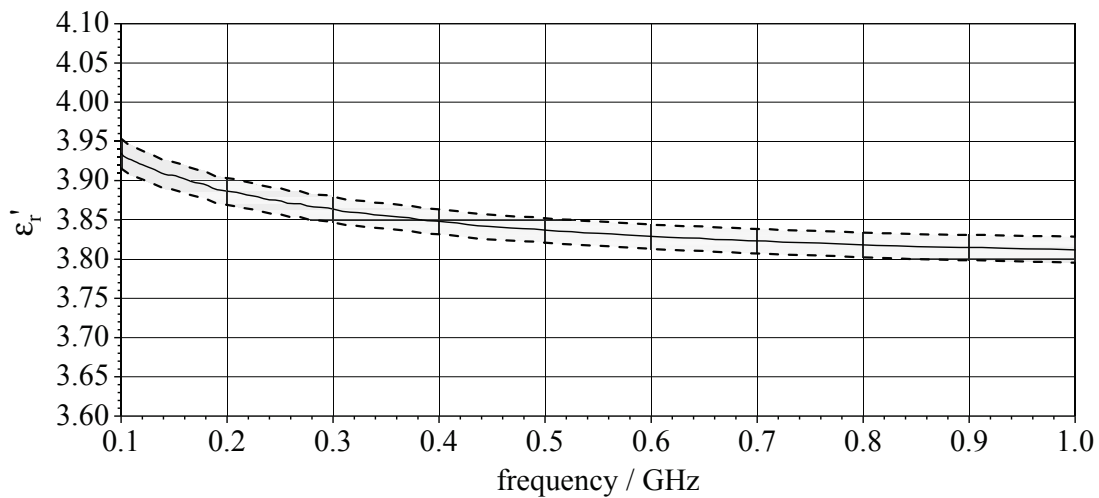


Figure 2.16 Relative permittivity of VESTAMID HTplus M1033 measured with admittance method

can lead to resonance effects occurring in the material at frequencies in the millimetre wave range, which makes this material seem less suitable for these applications.

2.4.3.3 VESTAMID HTplus M1033

VESTAMID HTplus M1033 by Evonik Industries AG is a semi crystalline polyphthalamide (PPA) with a glass fibre filling of about 30% per weight. The material is solderable. Due to the filling an anisotropy of the permittivity may occur. The sample preparation is done considering the flow direction of the moulded plastic plates. Test measurements with admittance method (z-direction) and both resonator methods (x- and y-direction) showed no considerable differences of the relative permittivity values. This may be due to the shape of the filler particles. This is the reason why the material is considered as isotropic.

Admittance Cell

The first evaluation is done with admittance measurement setup. Fig. 2.16 shows the measured relative permittivity evaluated of 10 samples with a size of $w = l = 20$ mm and a height of $h = 1$ mm.

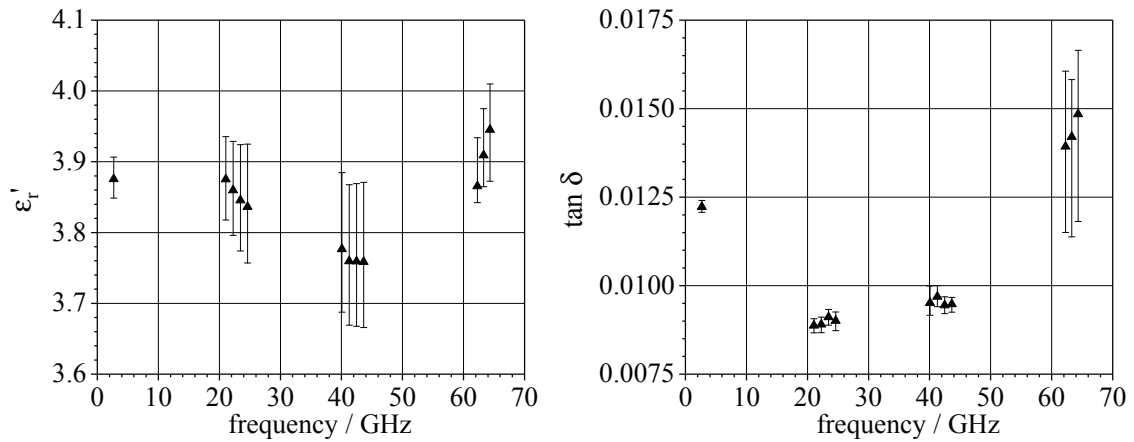


Figure 2.17 Complex permittivity of VESTAMID HTplus M1033 measured with the cavity - and open resonator

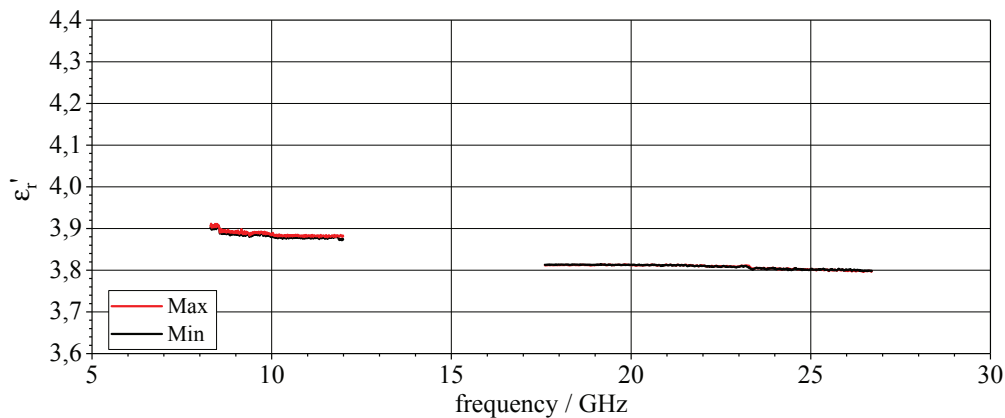


Figure 2.18 Relative permittivity of VESTAMID HTplus M1033 LDS measured with K- and X-band waveguide method

Resonator

Five test samples are measured with resonator methods. The corresponding results are shown in Fig. 2.17. The test samples for the open resonator are plastic plates with $h = 1$ mm and a length/width of $w = l = 127$ mm. For cavity resonator plastic rods are prepared by milling with a length of $l = 120$ mm and a cross section of $h = 1$ mm and $w = 1.5$ mm. The plastic plates showed a slight deformation due to mechanical tensions in the large and thin injection moulded plates. In the open resonator the plates are fixed in the sample holder. In doing

so the deformation is partially evened out. However, this slight deformations may increase the error tolerance.

Waveguide

As a third setup the relative permittivity is evaluated for two samples using the waveguide in X-band and K-band. Fig. 2.18 shows the measured relative permittivity for the two samples.

Evaluation of Measured Results for VESTAMID HTplus M1033

The results show that VESTAMID HTplus M1033 is a material with a filler showing no considerable anisotropy in the frequency range evaluated within this work. The relative permittivity is in a range of $\epsilon'_r = 3.95$ at $f = 100$ MHz decreasing down to $\epsilon'_r = 3.75$ at $f = 40$ GHz. At $f = 60$ GHz the relative permittivity increases from $\epsilon'_r = 3.85$ to $\epsilon'_r = 3.97$. This could also be observed for the other materials with mineral or glass fibre fillers. Even though the material showed no anisotropy in terms of an E-field alignment, effects due to the filling particles may occur in the millimetre wave range as it is described in Sec. 2.4. The loss tangent increases from $\tan \delta = 0.009$ at $f = 20$ GHz to $\tan \delta = 0.015$ at $f = 65$ GHz. The measurements with the K-band waveguide ($\epsilon'_r = 3.82$) and the open resonator ($\epsilon'_r = 3.85$) show comparable results for the frequency range around $f = 20$ GHz. The dielectric losses for VESTAMID HTplus M1033 are higher than those of typical RF substrates. This may be critical for applications requiring low losses, for instance in the millimetre wave range. Nevertheless, the higher losses may also be acceptable, especially when the specific mechanical properties of this material are required.

2.4.3.4 Xantar LDS 3720 and Xantar LDS 3732

Finally, two materials without filler are evaluated. Both materials are based on polycarbonate (PC). This type of material is already used in large scale productions of LDS antennas for mobile communication in consumer devices. Xantar LDS by MEP Europe B.V. is a material group available in different colours. Temperature resistivity of this material is around $T_{\text{res}} \approx 120$ C° making these materials not suitable for standard re-flow soldering processes. First

material evaluated is Xantar LDS 3720, a LDS-capable blend of Polycarbonate and Acrylonitrile Butadiene Styrene (PC/ABS). Having no filler this material can be evaluated without considering the flow direction of the injection moulding. While all other materials evaluated are coloured black or dark grey this material has a light greyish colour. The second material, Xantar LDS 3732, is a polycarbonate (PC) with an elastomer. Having no filler this material can also be evaluated without considering the flow direction of the injection mould process.

Admittance Cell

With the admittance method 10 samples with a size of $w = l = 20$ mm and a height of $h = 1$ mm are measured. Fig. 2.19 shows the measured arithmetic mean value of the relative permittivity for both materials.

Resonator

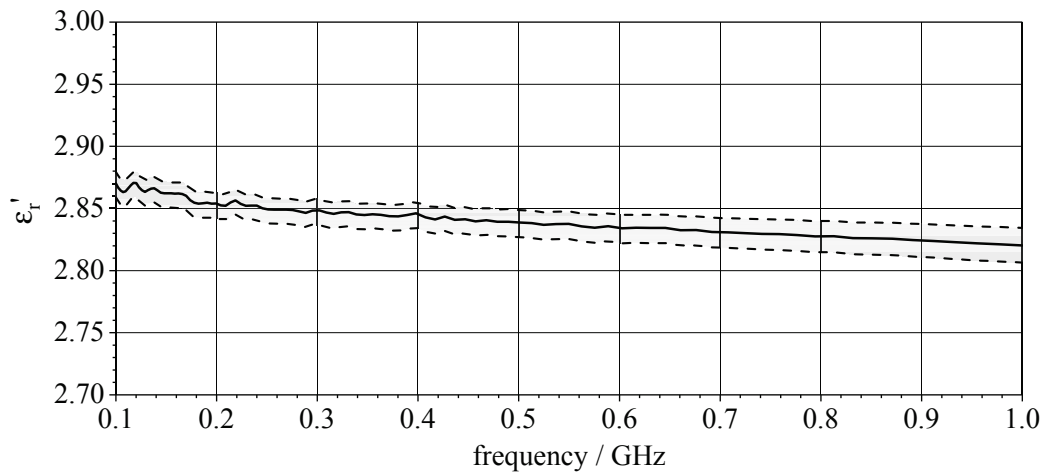
Five test specimens are measured with the resonator methods. The samples are plastic plates with $h = 1$ mm and an length/width of $w = l = 12.7$ mm. For cavity resonator plastic rods are prepared by milling with a length of $l = 120$ mm and a cross section of $h = 1$ mm and $w = 1.5$ mm. Fig. 2.20 shows the corresponding results.

Waveguide

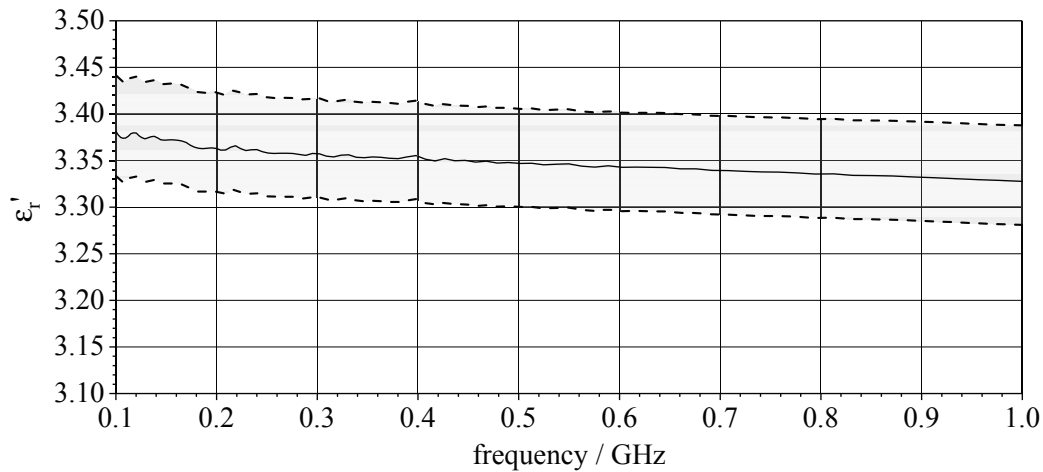
Finally, the relative permittivity is evaluated using the two waveguides in X-band and K-band. Fig. 2.21 and Fig. 2.22 show the relative permittivity measured. Since only two samples were available, no arithmetic mean is calculated and the measurement results are given separately for each sample.

Evaluation of Measured Results for Xantar LDS 3720 and Xantar LDS 3732

The measured values of the isotropic LDS material Xantar LDS 3720 show that the relative permittivity as well as the loss tangent are in a range as expected for this type of material. The material has a relative permittivity of $\epsilon_r' = 2.86$ at



(a) Xantar LDS 3720



(b) Xantar LDS 3732

Figure 2.19 Relative permittivity of Xantar LDS measured with admittance method

$f = 0.1$ GHz decreasing down to $\epsilon'_r = 2.83$ at $f = 1$ GHz. The measured arithmetic mean values at $f = 2.7$ GHz show a relative permittivity of $\epsilon'_r = 2.79$ and a loss tangent of $\tan \delta = 0.005$. The measured relative permittivity at $f = 20$ GHz is $\epsilon'_r = 2.78$ with a loss tangent of 0.005 decreasing to $\epsilon'_r = 2.76$ and a loss tangent of $\tan \delta = 0.005$ at 40 GHz. At $f = 65$ GHz the permittivity falls down to $\epsilon'_r = 2.6$ with a loss tangent of $\tan \delta = 0.0065$. Generally, it can be observed that all measurement data show a lower spreading compared to the reinforced LDS materials.

The measured values of the isotropic LDS material Xantar LDS 3732 show that

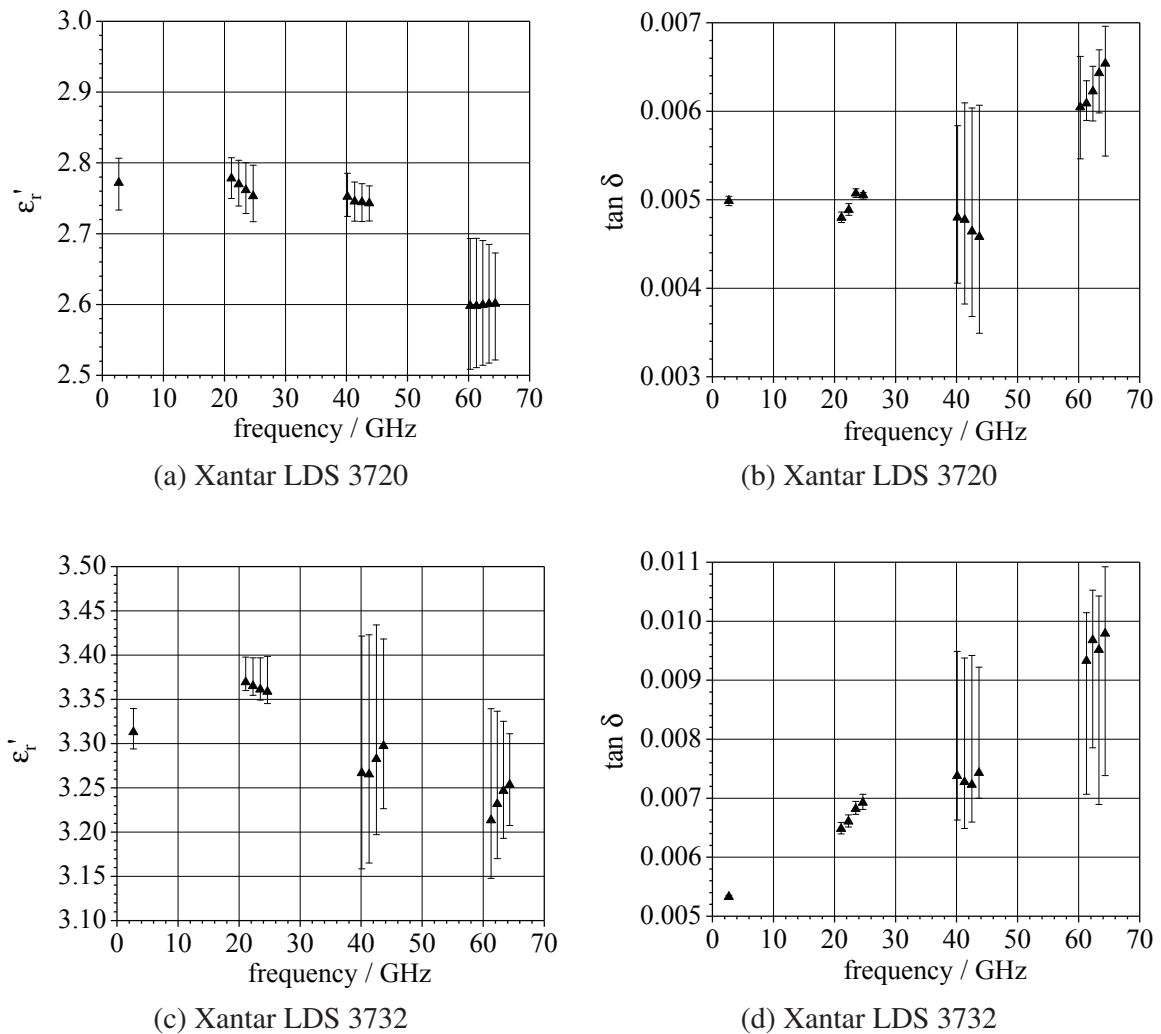


Figure 2.20 Complex permittivity of Xantar LDS measured with the cavity - and open resonator

the relative permittivity as well as the loss tangent are in a range as expected for this type of material. The material has a relative permittivity of $\epsilon'_r = 3.38$ at $f = 0.1$ GHz decreasing down to $\epsilon'_r = 3.34$ at $f = 1$ GHz. The measured values at $f = 2.7$ GHz show a relative permittivity of $\epsilon'_r = 3.32$ and a loss tangent of $\tan \delta = 0.0055$. The measured relative permittivity at 20 GHz is $\epsilon'_r = 3.36$ with a loss tangent of $\tan \delta = 0.0075$ decreasing to $\epsilon'_r = 3.28$ and a loss tangent of $\tan \delta = 0.0075$ at $f = 40$ GHz. At $f = 65$ GHz the permittivity falls down to $\epsilon'_r = 3.24$ with a loss tangent of $\tan \delta = 0.009$. The spread of the measurement values is higher than for Xantar LDS 3720. The samples showed no geometric deformations. Furthermore, the spreading can be observed for all measuring

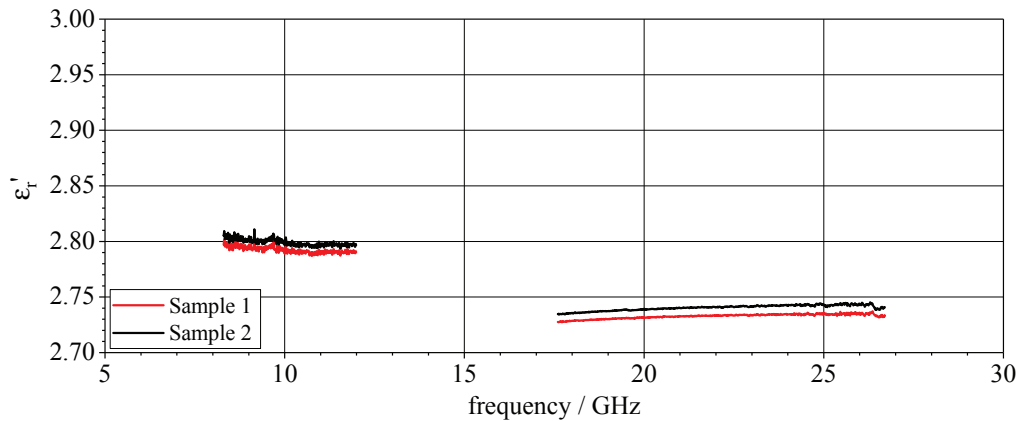


Figure 2.21 Relative permittivity of Xantar LDS 3720 measured with K and X-band waveguide method

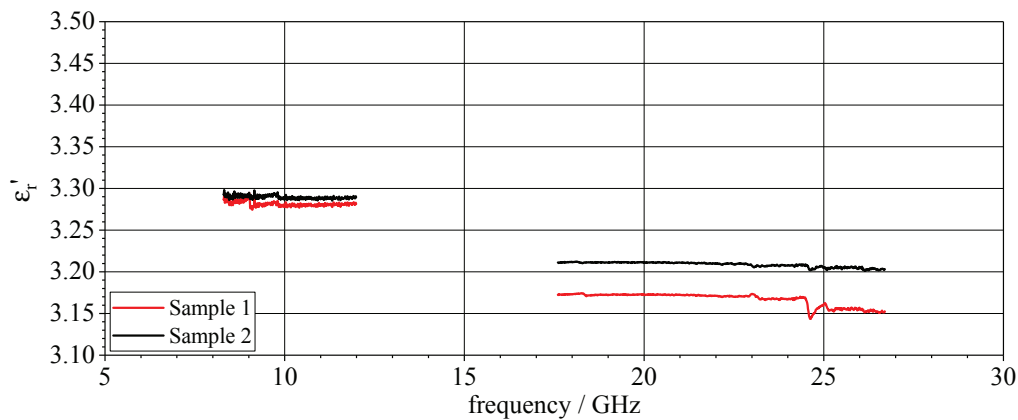


Figure 2.22 Relative permittivity of Xantar LDS 3732 measured with K- and X-band waveguide method

principles, which indicates that this is due to the specific material composition. The two isotropic XANTAR LDS materials have relatively low losses, comparable to typical RF substrates even at high frequencies ($f = 60$ GHz). Due to the isotropy of the material, it can be processed by injection moulding without taking the flow direction into account. This, together with the relatively low losses, makes Xantar LDS materials well suited for RF applications up to frequencies in millimetre wave range.

Condition	Width	Height	ϵ'_r	$\tan \delta$
Rogers 4003C without LPKF ProtoPaint	2512 μm	805 μm	3.54	0.003
Rogers 4003C with LPKF ProtoPaint	2583 μm	950 μm	3.43	0,0046
Calculated resulting values for LPKF Protopaint	71 μm	145 μm	2.7	0.13

Table 2.3 Evaluated values for LPKF ProtoPaint on Rogers 4003C with cavity resonator method at 3.9 GHz

2.4.3.5 LPKF ProtoPaint LDS

Due to the relatively high costs, it is not always possible to realise an injection mold to produce the 3D substrate for a prototype antenna. In these cases a stereographic part can be used, achieving the LDS-capability by applying LPKF ProtoPaint. Covering the surfaces results in a mixture of the dielectric properties of the 3D printed material and the LDS coating. Typical recommended thickness's for LDS ProtoPaint are about $t = 30 \mu\text{m}$. For most of the configurations at low frequencies only a slight influence can be expected. However, in narrow band applications (e.g. a patch antenna) or applications operating at higher frequencies, the influence should be considered in order to achieve a higher production accuracy.

Within this work different prototype antennas are fabricated using ProtoPaint. Therefore, the varnish is characterised concerning the complex permittivity. The varnish can not be processed to a measurable sample geometry. Therefore, the paint must be applied to a substrate to achieve a relatively uniform thickness. The cavity resonator is used for characterisation, since the thin rods can be covered evenly with ProtoPaint. Permittivity is calculated by dividing the measured values according to the ratios of the volume inserted. This method assumes that the field in the rod is evenly distributed, which applies to materials with dielectric values in a similar range. The measured results for ProtoPaint are shown in Fig. 2.3. As can be seen the relative permittivity is calculated to $\epsilon'_r = 2.7$ and the dissipation factor to $\tan \delta = 0.013$.

To define the effective dielectric constant of both components, the dielectric values of the 3D printed substrate and LPKF ProtoPaint must be known. The characterisation of the carrier material can be done as described above for the

LDS thermoplastics. The materials used for all LDS prototypes fabricated in this work are characterised in consideration of the specific operation frequency.

2.4.4 Conclusion

Summarising the dielectric characterisation of the LDS capable material carried out in this work Fig.2.23 shows the dielectric properties of all materials characterised with the resonator methods (open and cavity) for an alignment of the electric field in x-direction.

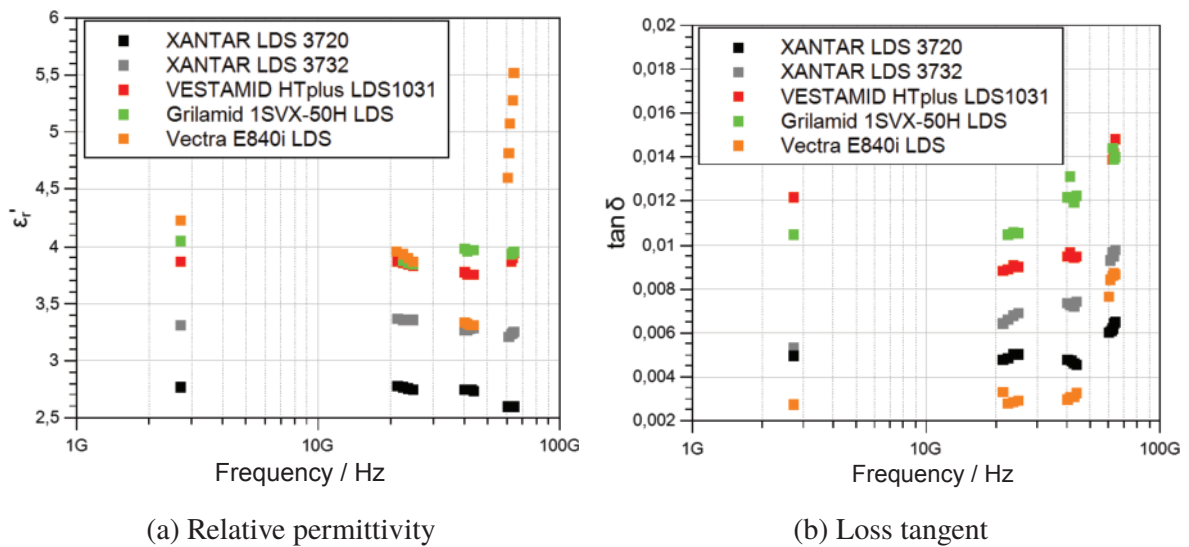


Figure 2.23 Overview of dielectric properties of LDS materials characterised with resonator methods in x-direction

The main observations concerning the RF properties of LDS substrate materials are:

- The relative dielectric constant of LDS-capable plastics is in a range comparable to typical RF substrate materials.
- For some LDS materials the loss tangent ($\tan \delta$) is higher than for typical RF substrates, but there are also materials with a loss tangent comparable to RF substrates.
- The LDS mixed metal oxide does not significantly change the dielectric properties of the base material.

- LDS plastics are partially filled for mechanical reasons. The use of fillers can lead to an inhomogeneity and anisotropy of the dielectric material properties, depending on the size of the filler particles.
- The filler particles can have a size in the range of wavelengths at millimetre wave frequencies. This can lead to resonances in the material that can unpredictably change the behaviour of an RF structure. For these applications a material without filler should be used.
- LDS materials are generally suitable to be used in RF applications. The decision as to which substrate material is used in an specific application must be made taking into account both RF and mechanical requirements.

2.5 RF Properties of LDS Metallisation

A further aspect that must be taken into account in order to determine the RF characteristics of an LDS-manufactured circuit carrier is the applied metallisation. In addition to the material properties of the metal layer, the macroscopic and microscopic geometric form must be taken into account, as they additionally influence the electrical properties. The geometric form contains on the one hand the form intended to realise the RF structure and on the other hand the unintentional variations due to the manufacturing process. These include, for example, imperfections in the form or the surface and edge quality due to laser structuring and plating. Some of the contents discussed in the following Section are based on the publications [AF3] and [AF4] (© IEEE 2016).

With regard to the material properties of the LDS metallisation, electrical conductivity and complex permeability are the most important influencing factors. As described in Sec. 2.2 the LDS metallisation frequently consists of more than one layer. These layers have different conductivities. In this case, the effective electrical conductivity is influenced by the current distribution which can be found on the cross section of the layer. The distribution of the current density in a metallic cross section is inter alia influenced by the operation frequency. With increasing frequency, the highest current density is located in the outer cross-section of a metal layer due to the skin effect. It should be clear that this is not automatically the outer surface of the metallised LDS part. The current density can also be displaced to the cross section connected to the substrate material or a combination of both. The skin depth for good conductors can be derived by using the following equation:

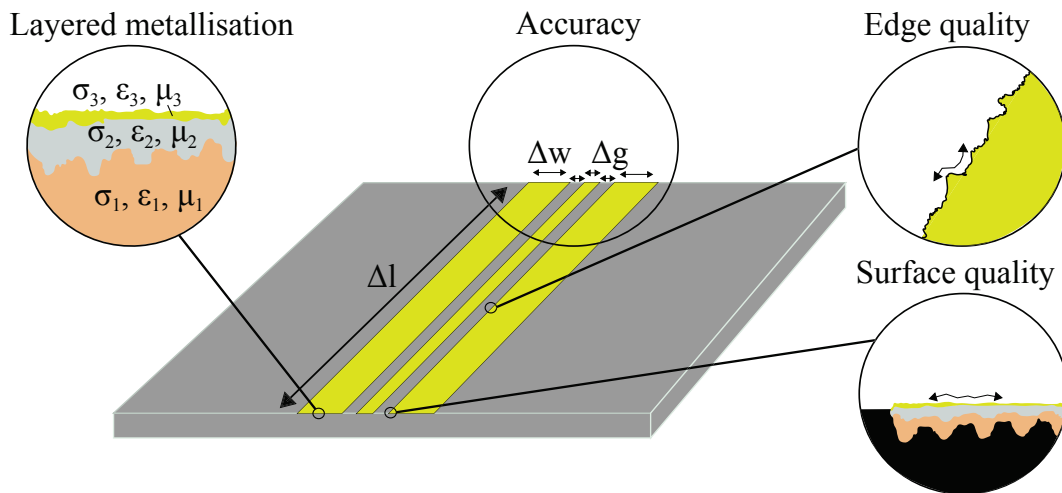


Figure 2.24 Influencing factors for the metallisation of LDS-manufactured samples

$$\delta = \sqrt{\frac{1}{\sigma\pi f\mu}} \quad (2.7)$$

which describes the penetration depth of a electromagnetic wave travelling along a PCB trace according to [35]. The skin depth depends on the frequency ω , the conductivity σ and the complex permeability μ . The skin depth is the penetration depth of the current density at which the value has decreased by $1e^{-1}$ or 0.37% compared to the current density on the surface of the conductor. Fig. 2.24 summarises the aspects influencing the RF properties of the metallisation of a LDS part using a coplanar waveguide as an example. In Sec. 2.3 the fabrication tolerances/accuracy are already discussed. All other aspects shown in Fig. 2.24 are covered in the following.

2.5.1 Layered Metallisation

The first aspect to consider when metallising RF structures using the LDS process is the layer metallisation usually used. As described in Section 2.2, the base layer consists of electroless copper with a typical layer thickness of $h_{\text{layer}} = 7\text{-}10 \mu\text{m}$. Surface finishing layers are applied onto this layer. These are mainly used for mechanical reasons and to protect the surfaces from oxidation. As mentioned above the effective conductivity of a layered LDS metallisation is determined by the current density in the metallic cross section. The distribution

Material	Conductivity	μ'_r	Skin depth @ 1 GHz	Skin depth @ 60 GHz	Typ. layer thickness
Copper (Cu)	35 MS/m	1	2.69 μm	0.35 μm	8-10 μm
Nickel/phosphor (NiP) (6%-8% phosphor)	1.5 MS/m	1	12.99 μm	1.68 μm	5-6 μm
Electro-deposited gold (Au)	25 MS/m	1	3.18 μm	0.41 μm	0.1 μm
Bulk silver (Ag)	63 MS/m	1	2.01 μm	0.26 μm	0.1 μm

Table 2.4 Skin depth and conductivity for different LDS metallization materials

of the current density in the metal layer is influenced, inter alia, by the skin effect.

Tab. 2.4 depicts the skin depth and the associated approximate conductivity values for metal layers that are used in the LDS process. The conductivity depends not only on the material, but also on the plating process itself. Consequently, values for the same material may vary with varying metallisation parameters. The conductivity of chemical nickel-phosphorus is specified in [21]. The phosphorus concentration can be varied from low to high phosphorous systems. The resulting conductivity of nickel-phosphorus metallisation depends heavily on the phosphorus concentration. All prototypes and test structures realised within the scope of this work are produced with a phosphorus concentration of 6% to 8%. For electroless copper, an approximate value for the LDS process is given in [22]. There was no value found for immersion gold and silver in literature. This is probably due to the fact that the layer of immersion gold/silver is very thin and cannot be characterised. For electro-deposited gold, an approximate value is given in [36]. For immersion silver it can be assumed that the conductivity is at least below the conductivity of the bulk material (63 MS/m). The calculated skin depth shows that the skin depth of silver has the lowest value due to its good conductivity. When using standard LDS metallisation with Nickel/Phosphorus and immersion Gold Finish (ENIG), the penetration depth for frequencies up to $f = 60$ GHz is significantly higher than the thickness of the Gold layer. This leads to reduced conductivity as the nickel/phosphorus conductivity is only about $\sigma = 1.5$ MS/m at a phosphorus concentration of 6% to 8%. For applications in the millimetre wave range, this poor conductivity might be critical. In these cases, a metallisation without nickel/phosphorus reduces the losses. This could e.g. be done with a coating of immersion silver.

2.5.2 Influences Due to Surface Quality

As shown in Fig. 2.24, another aspect that affects the RF characteristics of an LDS-manufactured RF device are the surface and edge texture. Fig. 2.25 shows the cross-sectional view of a coplanar LDS waveguide. As can be seen, the metal layer has a very rough surface texture, while the substrate that is not metallised is relatively smooth. This can be observed both on the top side of the metal layer and on the underside. As already evaluated and discussed in Sec. 2.3, this roughness is primarily caused by the laser structuring process. The laser generates a grooved surface in the direction of structuring. The exact shape of the surface depends on the width of the laser beam, the overlapping, the pulse repetition rate and the laser power used for structuring.

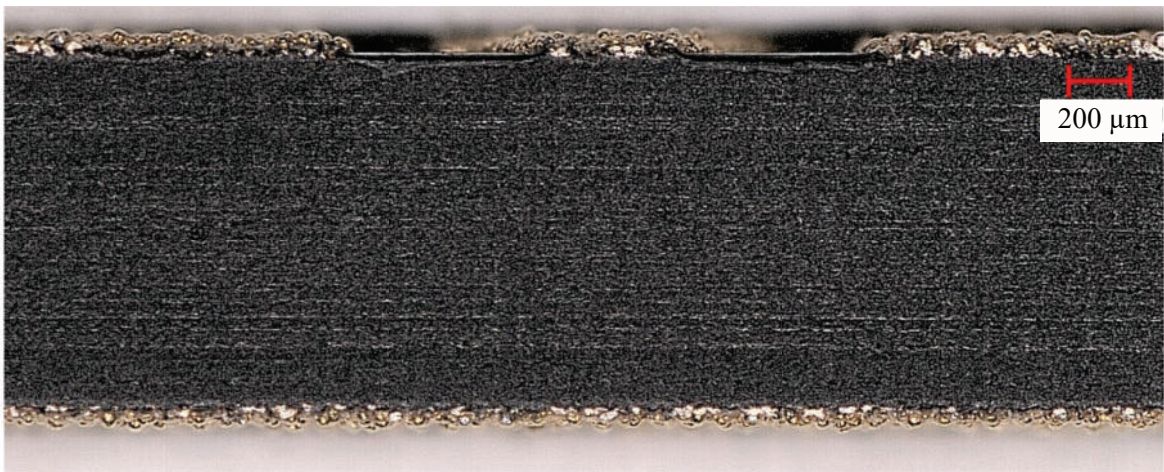


Figure 2.25 Cross sectional view of a LDS samples with Cu/NiP/Au metallisation

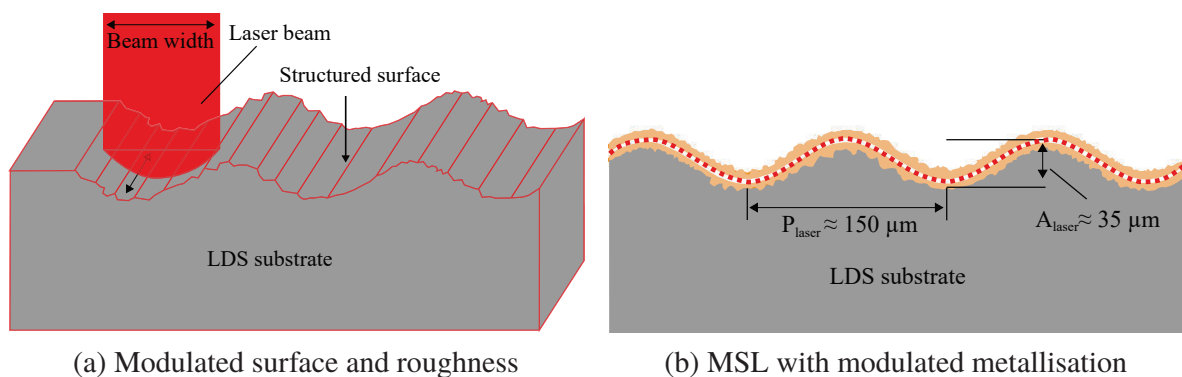


Figure 2.26 Model of a laser structured test sample with surface profile

In order to gain an insight into the effects on the RF properties, the surface texture induced by laser structuring can be interpreted as a modulation of the substrate surface. Fig. 2.26a shows a corresponding schema of the structuring process and the resulting surface. The surface can be approximated as a sinusoidal surface modulation in one direction. For the sample shown in Sec. 2.3, Fig. 2.6b the peak-to-peak amplitude can be approximated to $A_{\text{laser}} = 35 \mu\text{m}$ and the period is about $P_{\text{laser}} = 150 \mu\text{m}$. The repetition rate of the laser pulse leads to a variance in the depth of the lasered grooves. A change in laser power affects the overall depth of the grooves. Consequently, both parameters influence the amplitude of the surface modulation. The change in beam width or the overlapping of the laser structuring primarily influences the period of surface modulation. As described in Sec. 2.2, these laser parameters can be varied within limits for the same substrate material. Furthermore, the laser parameters are adjusted for different substrate materials. This results in different surface profiles, which depend on the material and the specific laser parameters of the sample. The variation of the surface structure can also be observed on the evaluated roughness values in Sec. 2.3. Besides the grooves in the surface the laser structuring additionally induces a roughness that overlies the surface modulation and that is randomly distributed. When depositing the metal layer, the resulting surface roughness on the bottom side of the conducting layer is influenced by the laser structuring and additionally by the electroless plating process. On the visible side of the metal layer the roughness is mainly influenced by the plating.

As depicted in Fig. 2.26 the laser induced grooves can be found on the upper and on the bottom side of the metal layer. The whole structure can be described as a rough metal layer with a thickness of $h_{\text{layer}} \approx 10 \mu\text{m}$ having a sinusoidal modulated shape.

As mentioned above the current density in the conductor is not evenly distributed over the cross-section due to the skin effect. Tab. 2.4 shows that the skin depth in LDS copper is approximately $\delta_{\text{skin}} = 2.69 \mu\text{m}$ at $f = 1 \text{ GHz}$. With a layer thickness of $h_{\text{layer}} = 10 \mu\text{m}$ a $\delta_{\text{skin}} = 2.69 \mu\text{m}$ thick area of the entire cross section carries 0.37% of the current density. With the frequency range considered in this work and the specific surface texture of the laser structured samples the effect on the conductor losses due to the laser induced surface modulation can be approximated as a lengthening of the conductor. This only applies to a wave-propagation transverse to the laser grooves. The lengthening of the conductor due to the surface modulation can be approximated by evaluating the arc length of a sinus function with the amplitude and period as derived in Sec. 2.3 ($A_{\text{mod}} = 35 \mu\text{m}$, $P_{\text{mod}} = 150 \mu\text{m}$). This results in a lengthening of about

2%. Since this is only a slight change with minor influence on the overall losses, it is neglected in the following.

A second source of loss in the conductor is the superimposed surface roughness. The losses due to this surface roughness can be calculated with the aid of surface roughness models. In the literature, various models describing the effects of the surface shape of a conductor on induced losses are discussed. Some of these models are based on correction factors like Groiss [37], Hammerstad [38] or Hall [39]. There are also models based on the microscopic evaluation of the surface, e. g. the model of Huray et al. [40]. Huray's model was evaluated on the basis of pictures taken with a scanning electron microscope (SEM) on electrolytically deposited copper foils as produced in the printed circuit board industry. The surface structures are very similar to the roughness of the electroless plated LDS surfaces. This implies that the model may also be applicable to the LDS-manufactured metallisation.

2.5.3 Influences Due to Edge Quality

Depending on the field distribution on the RF structure, the condition of the edges is another aspect that influences the losses induced. As evaluated in Sec. 2.3 the laser structuring also influences the edge quality. Structuring in line with the edge leads to a relatively smooth edge whose quality mainly depends on the roughness induced by the plating process. A structuring transverse to the edge causes a modulated edge structure similar to the modulated surface described above. This effect is again overlaid with a randomly distributed surface roughness that is mainly determined by the plating process. Regarding the losses that are induced in the metal layer the influences of the edge condition can be considered in the same way as described above for the LDS structured surface.

2.5.4 LDS Fabricated Transmission Lines

The observations gained in the last Sections indicates that the losses induced in a LDS fabricated metal layer can be expected to be lower than indicated by analysing the overall surface quality. The values typically used to describe the surface quality, like e.g. R_z / S_z , R_q / S_q and R_a / S_a are not sufficient to derive the losses induced in a LDS fabricated conductor. This is due to the specific shape of the surface that is slightly modulated due to the laser structuring. In

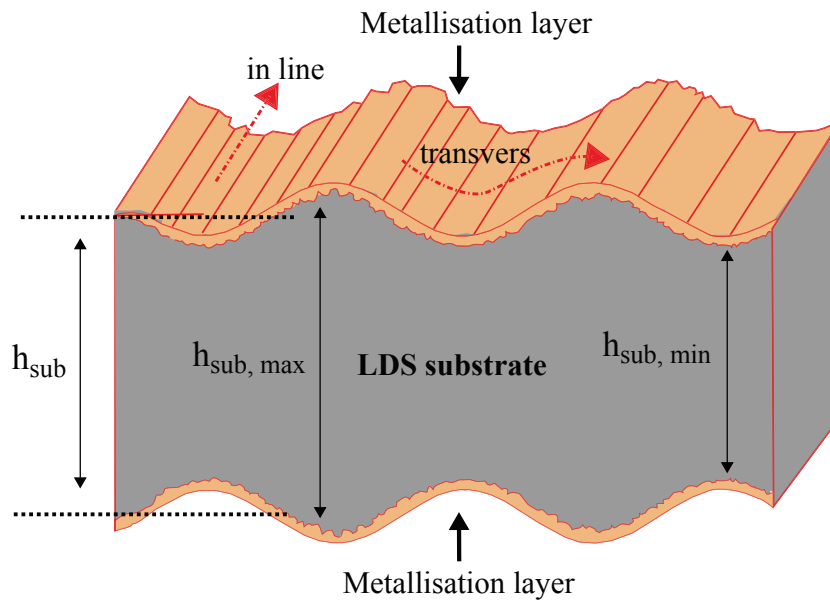


Figure 2.27 Schematic view of an LDS-metallised substrate with laser-induced surface modulation on the top and bottom.

the following Section this implication will be verified by the measurement of coplanar waveguides fabricated with different LDS metallisation compounds. Besides the lengthening of the current path, the surface modulation may influence the characteristic impedance of a transmission line. This applies in particular to transmission lines whose characteristic impedance is considerably influenced by the substrate height, e.g. microstrip lines. A structuring in the direction of the wave propagation leads to a sinusoidal variation of the metal layer over the width. Structuring transverse to the direction of propagation will lead to a continuous change of the impedance in the direction of propagation. Fig. 2.27 shows a schematic drawing of such a surface pattern on the top and bottom of a substrate.

Using the example of an MSL fabricated on Xantar LDS 3720 ($\epsilon_r = 2.77$ and $\tan \delta = 0.005$ at 24 GHz), a surface modulation in the direction of wave propagation with an amplitude of $A_{mod} = 35 \mu m$ on both sides of the substrate leads to a maximal variation in height of $h = h_{sub} \pm 35 \mu m$. In case of a MSL designed for $f = 24$ GHz and a substrate height of $h_{sub} = 500 \mu m$ this will result in a change of the line impedance from the designed $Z = 50 \Omega$ to $Z_{mod} = 50 \pm 2.5 \Omega$. This slight and continuous change will result in an effective line impedance averaged over the line width/length. As a result, considerable influences on the characteristics of the transmission line are not expected. In case of a coplanar line as evaluated in the following the height of the

substrate has even less influence on the line impedance. This is due to the field distribution concentrated in the gaps between the inner conductor and both ground conductors. In this case the structuring direction on the edges will have the dominating influence.

The characterisation of the dielectric properties and the evaluation of the surface quality of LDS fabrication allows to predict the induced losses. This is done in the following using ADVANCED DESIGN SYSTEM 2013.06 LineCalc. As described in the manual, the calculation of the characteristics of the CPW is done on the basis of [41] and the calculation of the conductor losses according to [42]. In LineCalc the losses due to the roughness are calculated with the Hammerstad model [38] on the basis of the RMS amplitude of a saw tooth pattern. Using LineCalc a CPW with the geometric dimensions as used for the following measurements is evaluated (Fig. 2.28). The RMS roughness is derived of the roughness values evaluated in Sec. 2.3. For a structuring transverse to the direction of wave propagation a filter is used to discard the components due to the surface modulation caused by the laser structuring. This results in a RMS roughness of $R_q = 5.9 \mu\text{m}$ while the RMS roughness without filtering is about $R_q = 11.4 \mu\text{m}$ (Tab. 2.1). For the samples that are structured in line the measured data obtained for the sample can directly be used.

Tab. 2.5 shows the calculated insertion loss obtained for Xantar LDS 3730 ($\epsilon_r = 2.9$ and $\tan \delta = 0.007$ at 60 GHz) with an LDS copper layer. As can be seen for the sample structured in the direction of propagation, the calculated insertion loss is $a = 1.32 \text{ dB/cm}$ taking into account the total surface texture in the roughness evaluation. Using the filtering to discard the wavelength of the laser induced surface modulation (P_{mod}) the calculated insertion loss is reduced down to $a = 1.1 \text{ dB/cm}$. For the sample with a structuring in line with the wave propagation the losses are calculated to $a = 1.08 \text{ dB/cm}$ which is nearly similar to the sample where the surface modulation is discarded. As a comparison, the losses are additionally calculated for the RF substrate Rogers 4003C with a rolled copper layer ($a = 0.81 \text{ dB/cm}$).

The calculated loss values as depicted in Tab. 2.5 are compared with the measurement results obtained for different LDS fabricated metallisation compounds evaluated in the following.

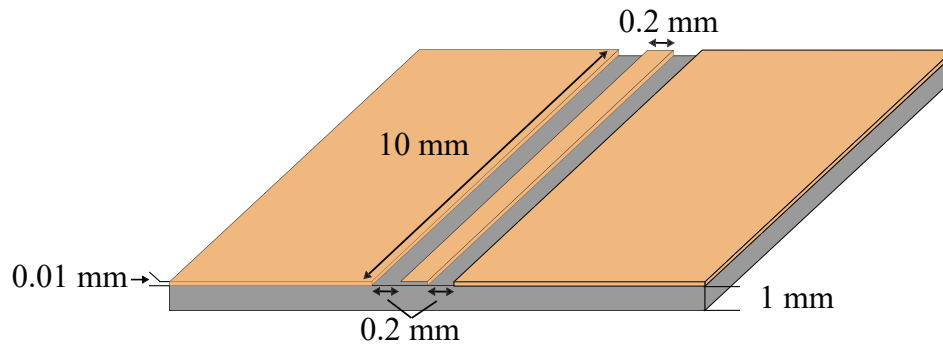


Figure 2.28 Dimensions of the model used for calculation of the losses of a CPW

Description	Conductivity	$\tan \delta$	R_q	Insertion loss
Xantar LDS 3730 with CU - struc. and eval. in line	35 MS/m	0.007	$5.6 \mu\text{m}$	1.08 dB/cm
Xantar LDS 3720 with CU - struc. and eval. transverse	35 MS/m	0.006	$11.4 \mu\text{m}$ (overall)	1.32 dB/cm
Xantar LDS 3720 with CU - struc. and eval. transverse	35 MS/m	0.006	$5.9 \mu\text{m}$ (filtered)	1.1 dB/cm
Rogers 4003C, rolled CU	58 MS/m	0.0027	$4.5 \mu\text{m}$	0.81 dB/cm

Table 2.5 Calculated insertion loss at $f = 60$ GHz of a CPW using ADS LineCalc

Metallisation	Layer thickness	Laser parameter	Qty.
Cu	10-12 μm	$\alpha = 45^\circ / 0^\circ$; 5.7 kHz; 5.75 W	2
glavanic Cu	-	$\alpha = 45^\circ / 0^\circ$; 5.7 kHz; 5.75 W	3
Cu/NiP	10-12 / 5-7 μm	$\alpha = 45^\circ / 0^\circ$; 5.7 kHz; 5.75 W	2
Cu/NiP/AU	10-12 / 5-7 / 0.05-0.1 μm	$\alpha = 45^\circ / 0^\circ$; 5.7 kHz; 5.75 W	2
Cu/AG	10-12 / 0.05-0.1 μm	$\alpha = 45^\circ / 0^\circ$; 5.7 kHz; 5.75 W	2

Table 2.6 Evaluated metallisation compounds with associated fabrication parameters

2.5.4.1 Measurement of Propagation Constant

Tab. 2.6 shows the configuration of the test samples fabricated and evaluated in the following. The manufacturing parameters are varied by the laser inclination angle (α), the direction of laser structuring and the composition of the metallisation layers. The laser power, laser spot width, overlap and pulse repetition rate remains the same for all test samples. The laser structuring for the LDS samples is done in the direction of propagation with a laser inclination angle of $\alpha = 45^\circ$ and $\alpha = 0^\circ$. By using different laser inclination angles the three dimensional fabrication process can be evaluated although a planar transmission line has to be used due to the limitations in the measurement setup. Each metallisation compound is based on a layer of electroless LDS copper. The current density of a CPW can be expected to be concentrated around both gaps of the CPW for the quasi TEM mode [43]. This indicates that the dominating layer influencing the induced conductor losses will be the outer, visible side of the sample. For comparison, the CPW produced by a photolithographic process metallised with a rolled copper layer on Rogers 4003C is characterised.

Each sample consists of four transmission lines with different length (l_x), a short and an open line (Fig. 2.29b). This configuration allows for a multiline TRL calibration [44]. The dielectric substrate is a injection moulded plastic plate of Xantar LDS 3730 (MEP Europe B.V.) with a height of $h = 2$ mm and a relative permittivity of $\epsilon_r = 2.9$ and a loss tangent of $\tan \delta = 0.007$ both measured at $f = 60$ GHz. There are five samples fabricated and 2 up to 3 measured of each configuration.

Fig. 2.29a depicts the measurement setup with a test sample positioned on the wafer prober and the measurement tips on the left and right side. The

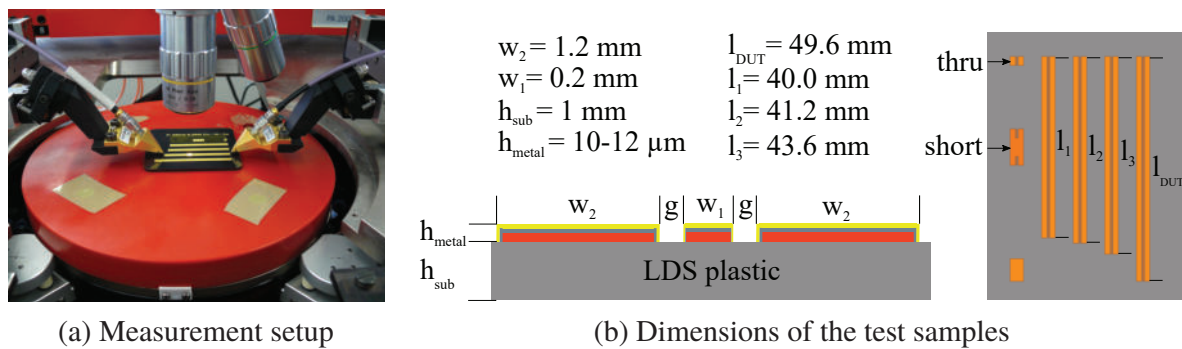
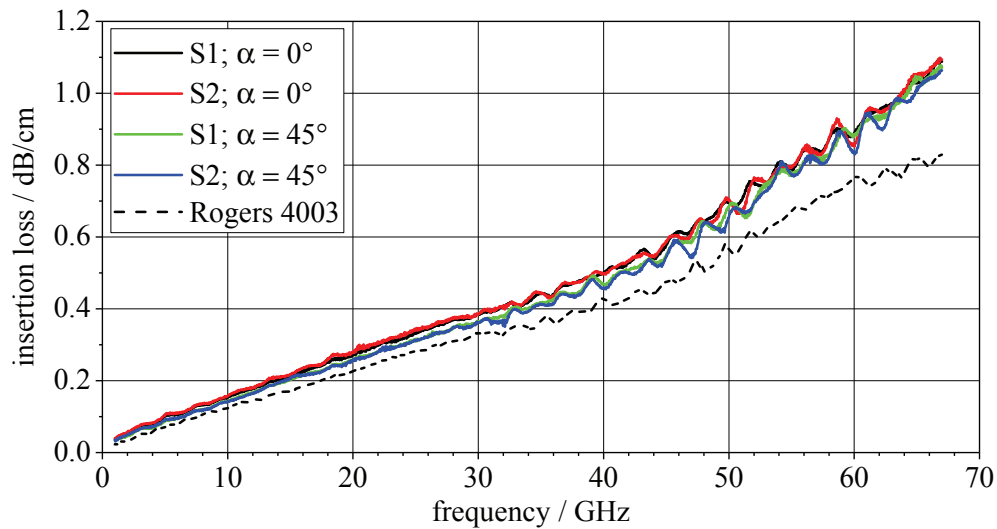


Figure 2.29 Configuration of test setup for evaluation of LDS fabricated coplanar waveguides

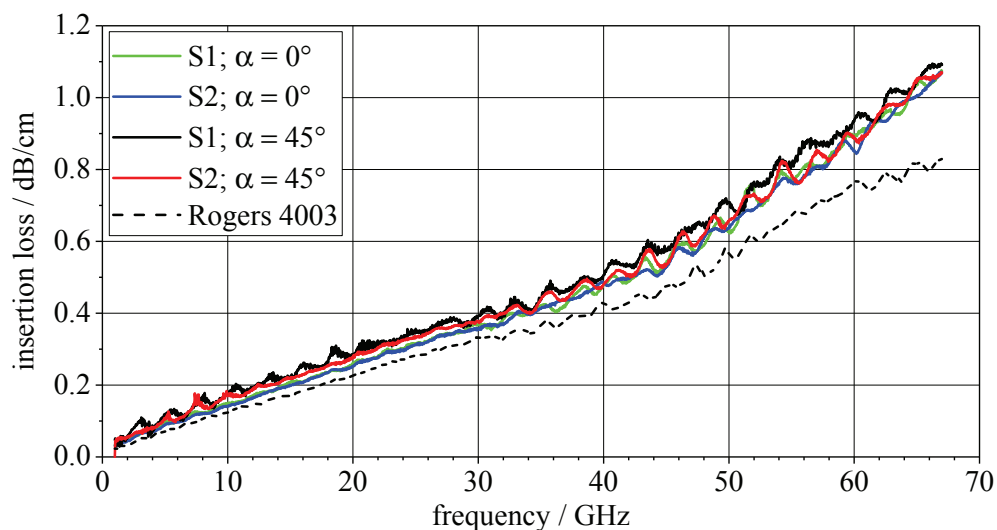
measurement probes are GSG (ground-signal-ground) probes with a pitch of $400 \mu\text{m}$ ($|Z|$ Probe 1MX, Ni, 67GHz, GSG, 400um, Cascade Microtech GmbH). The complex scattering parameters are measured and subsequently processed with StatistiCAL Version 1.1.76. StatistiCAL allows to calculate a statistical average of different measurements to compensate the variations resulting of the positioning of the measurement tips on the metal surfaces. Each test sample is measured placing the probes three times on each transmission line and short/thru standard, respectively. The frequency range evaluated is $f = 1 \text{ GHz}$ to $f = 67 \text{ GHz}$.

Firstly, the test samples plated with electroless and galvanic copper are evaluated. Two test samples with electroless copper and three samples with galvanic copper plating are analysed. Fig. 2.30 shows the insertion loss (a) in dB/cm. The measured insertion loss of the galvanically and electroless plated samples is nearly the same. For the varied laser inclination angles the insertion loss for $\alpha = 45^\circ$ (blue and green line) seems to be slightly lower. This may be due to a slight reduction of the surface roughness. The laser structuring with a laser inclination angle of $\alpha = 45^\circ$ causes a widening of the laser spot. This influences the surface texture of the metallised surface. Additionally, the measured insertion loss shows a slightly oscillating characteristic over frequency. This is due to variations of the measurement configuration during the Multiline TRL calibration process. One reason for such slight variations is that the LDS copper layer is relatively soft and the measurement probes can sink into it. Consequently, the measurement configuration varies each time the probes are placed. As can be seen in the following measurements of the LDS samples with NiP, this effect is significantly reduced by the harder NiP surface.

Fig. 2.31 shows the insertion loss a in dB/cm for the evaluated test samples plated with electroless Cu/NiP and with Cu/NiP/Au. The curves show a smoother



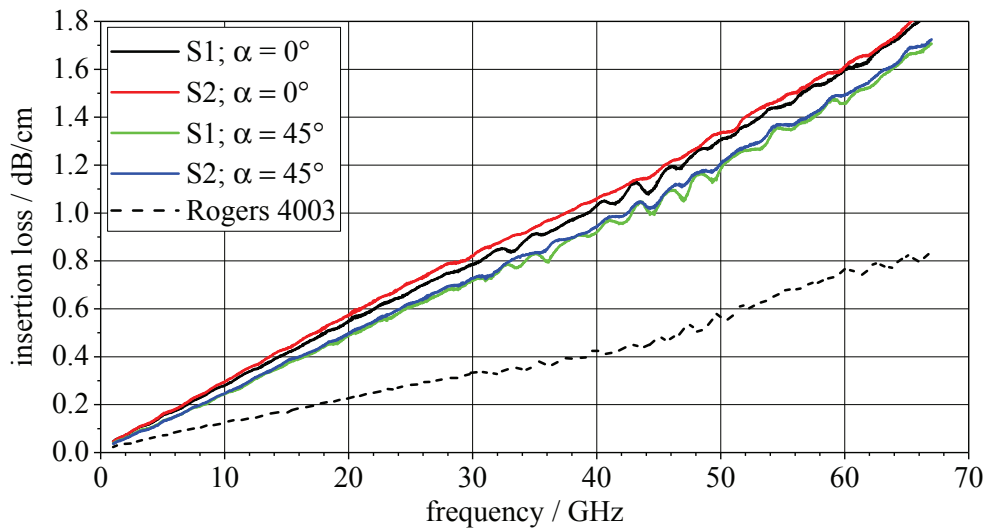
(a) electroless



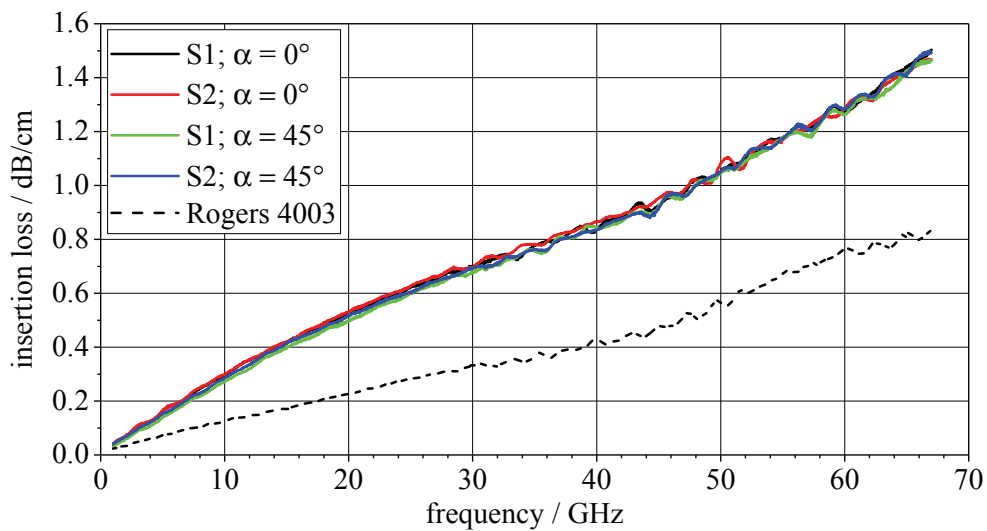
(b) galvanic

Figure 2.30 Measured insertion loss for LDS test samples plated with copper (Cu)

shape due to the harder surface of the NiP allowing for a more precise calibration procedure. In case of the Cu/NiP compound the effective layer in terms of conductivity is the nickel layer. The conductivity of the electroless plated nickel (NiP with $\approx 8\%$ Phosphorous) is only about $\sigma = 1.5 \text{ MS/m}$. This is the reason for the high insertion loss of about $a = 1.6 \text{ dB/cm}$ at $f = 60 \text{ GHz}$ for a laser inclination angle $\alpha = 0$. The insertion loss for a laser inclination angle of $\alpha = 45^\circ$ is again slightly reduced to $a = 1.5 \text{ dB/cm}$. In case of the Cu/NiP/Au



(a) Cu/NiP



(b) electroless Cu/NiP/Au

Figure 2.31 Measured insertion loss for LDS samples plated with copper and nickel-phosphorus

metallisation the effective layer is the gold and the nickel layer. Due to the fact that the gold layer has a layer thickness of only $h_{\text{layer}} \approx 0.1 \mu\text{m}$ the nickel layer has a considerable influence on the effective conductivity. This is also reflected in the measurements. The insertion loss is slightly reduced from $a = 1.5 \text{ dB/cm}$ for the NiP layer to $a = 1.3 \text{ dB/cm}$ with an immersion gold layer on top. Especially, for applications in millimetre wave range such high losses may not be acceptable. Consequently, other metallisation compounds have to be used.

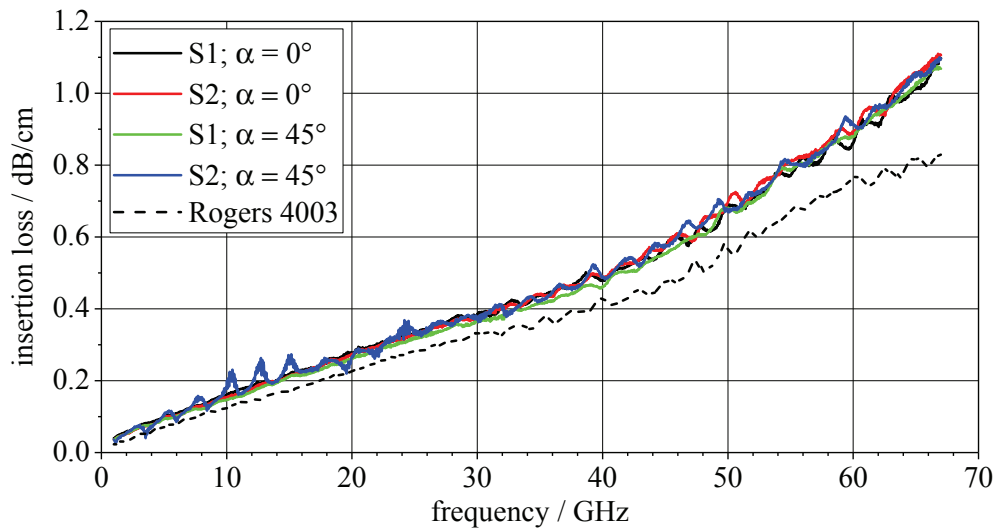


Figure 2.32 Measured insertion loss for different LDS test samples plated with Cu/Ag

Fig. 2.32 shows the insertion loss a in dB/cm for the evaluated test samples plated with electroless copper and immersion silver (Cu/Ag). Two test samples are evaluated. At different laser inclination angles, no differences in the measurement data can be found. The insertion loss is the same as for the copper samples although the silver layer has a higher conductivity. This is due to the thin layer thickness of the immersion silver layer. The skin depth is higher than the layer thickness of the silver layer as with the immersion gold layer. The main purpose of the covering layer is to protect the copper surface from oxidation. This makes this metallisation compound a good alternative to standard LDS metallisation with NiP/Au.

Comparing all measured results with the sample fabricated on Rogers 4003 substrate the losses induced at $f = 60$ GHz are about $a = 0.75$ dB/cm for the Rogers sample and $a = 0.9$ dB/cm for LDS plated samples with Cu or Cu/Ag. It has to be considered that the higher losses of the LDS samples are not only due to higher conductor losses. The LDS substrate used has a loss tangent of about $\tan \delta = 0.005$ at $f = 20$ GHz while the Rogers 4003C has a loss tangent of about $\tan \delta = 0.0027$ at $f = 10$ GHz as specified in the data sheet. Consequently, the higher losses are not only due to conductor losses but also due to the higher dielectric losses. Furthermore, the rolled copper layer has a higher conductivity close to bulk copper ($\sigma = 58$ MS/m) while the LDS sample has a conductivity of only $\sigma = 35$ MS/m.

Finally, two LDS fabricated samples are compared. One sample is structured

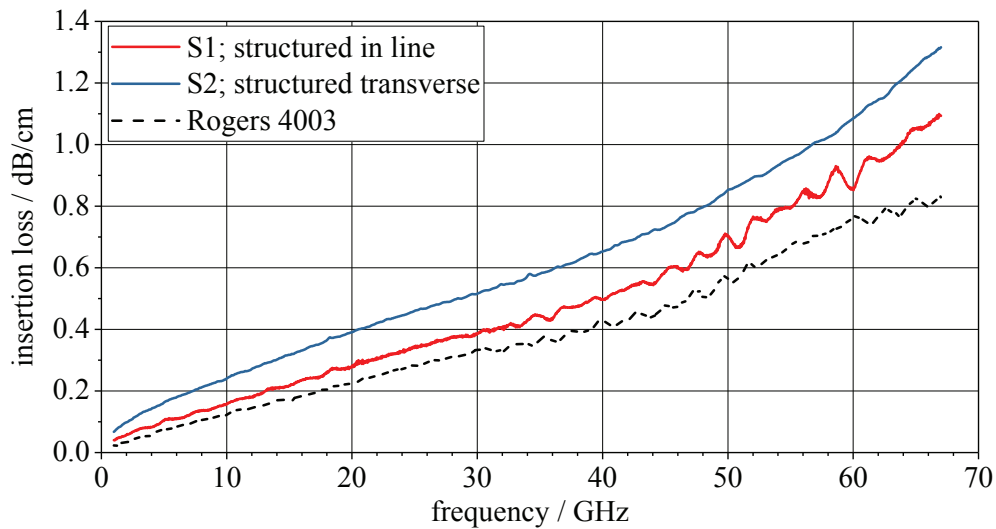


Figure 2.33 Measured insertion loss for LDS test samples structured in line and transverse plated with Cu

in line and the other transverse. The sample that is structured transverse to wave propagation is characterised using the same measurement procedure as described above. The values are plotted in Fig. 2.33. The insertion loss for the sample that is structured transverse is $a = 1.08$ dB/cm while for the sample structured in line only $a = 0.9$ dB/cm are measured. It has to be considered that both samples measured were not fabricated in the same batch. Thus, there might also be slight differences due to the influences of the specific fabrication parameters. Nevertheless, the results indicate that the losses induced in an LDS fabricated metal layer can be influenced by the process parameters, like the direction of structuring.

Comparing the measured results with the calculated values using ADS LineCalc as shown in Tab. 2.5 a similar behaviour can be observed. Especially, the measured values for a structuring in line and transverse to the direction of wave propagation agree very well with the calculated results. This shows the suitability of the aforementioned approach to describe the RF properties of an LDS fabricated metallisation.

2.5.5 Conclusion

Concluding, the main observations concerning the properties of LDS fabricated metal layers are:

- An LDS metallised layer can be described as a surface modulated metal layer with an overlaying surface roughness.
- Evaluating the surface roughness of an LDS fabricated metal layer without considering the specific surface condition may lead to an overestimation of the losses induced.
- The conductor losses can be influenced by considering the direction of wave propagation in the structuring process.
- The laser inclination angle ($\alpha = 0$ deg and $\alpha = 45$ deg) slightly influences the induced losses.
- The losses induced can be considerably influenced by the metallisation compound used especially in terms of the conductivity.

The following section discusses briefly the main aspects of the electromagnetic field simulations carried out for the design of the antenna systems that are discussed in the following chapters. Using a field simulation software the settings as well as the discretization and the exact setup of the models may influence the accuracy of the simulation results and the simulation time. Depending on the method used for field simulation the modelling and simulating 3D surfaces can influence the efficiency of the calculation considerably.

Parameter	Value
Maximum delta S	0.01-0.02
Number of converged passes	2-3
Maximum refinement per pass	30%
Maximum refinement	100000
Order of solution function	mixed order
Solution type	driven modal
Sweep type	discrete
Boundary conditions	radiation (ABC)

Table 3.1 Main settings used for electromagnetic simulations with HFSS

For all EM Simulations done in the following ANSYS HFSS 14.0 and 16.0 is used. This software is based on a frequency domain solver. The discretization is done using the automatic adaptive meshing function of the software. Tab. 3.1 lists the setting of the parameters defining the calculation of the EM properties. These are the standard values used for the EM field simulations carried out for the design of the antenna systems described in this work. Depending on the status of the design some of the parameters are refined for selected models.

Depending on the complexity of the substrate the CAD modelling is partially done in the MCAD software SOLIDWORKS, Version 2012 or directly in HFSS. The application of the 3D metal sheets is done in HFSS using the boolean operation "intersect". Therefore, the structure to be realised is drawn as polygon. This sheet structure positioned in parallel to the surfaces the metal sheet should be applied on. Afterwards the sheet structure is thickened by using the "thicken sheet" function. By creating a sheet of the surfaces of the 3D substrate the 3D metal sheet should be applied on and doing an boolean intersect with both, the 3D metallisation can be created. The slight distortion due to the application of the metal structure on the 3D surface is compensated in the electromagnetic design process.

As not otherwise mentioned the metal structures are modelled as sheets with an finite conductivity of $\sigma = 35 \text{ MS/m}$ as for LDS electroless plated copper. All dielectric materials are modelled with their full resolution using the material properties evaluated in the dielectric material characterisation as described in Sec. 2.4.

As not otherwise mentioned the evaluation of simulated and measured radiation characteristics is done as partial realised gain for the specific polarisation of the designed antenna.

3D Antenna Concepts for Vehicle Integration

Integrating radio services into a vehicle different trends can be observed. One aspect is the increasing number of RF applications that have to be integrated. This means in detail that the number of antennas is increasing. Some radio services allow or require additionally multiple antenna systems (MIMO), which can further increase the space required for antenna installation. In contrast, limitations in terms of vehicle design have a significant impact on the spaces available for antenna integration. In past times protruding antennas on the vehicle roof were accepted, like e.g. rod antennas. Modern vehicles are expected to have the RF systems integrated inconspicuously in the vehicles design. An example of such an integration is the plastic housing of the BMW roof antenna module, a fin-shaped design element that covers several antenna systems underneath. Current vehicle antennas for broadcasting, cellular and satellite communication cover frequencies from a few megahertz up to $f = 6$ GHz, as shown in Figure 4.1. For operating frequencies below $f = 700$ MHz on glass or short rod antennas are used. For vehicles such as convertibles or vehicles with metallised windows, an installation on glass is not possible. In these cases the bumpers, wheel cases or boot lid are used. Alternatively, shortened monopole rod antennas are used for convertibles, e.g. on the cowl [OK1].

Antennas operating above $f = 700$ MHz are often integrated underneath plastic parts installed on the vehicle roof, like e.g. a roof antenna module. Fig. 4.2 shows the plastic part used to cover such an antenna system, on the example of a BMW (sedan type vehicle). The communication systems integrated underneath are either for terrestrial or satellite communication. This results in different requirements concerning the radiation characteristic. For terrestrial RF systems an omnidirectional radiation pattern in the horizontal plane is required. This may apply to the single element or in case of a MIMO antenna system for the superimposed radiation pattern. The polarisation for all current terrestrial vehicle RF systems is linear. For satellite communication, a directive radiation characteristic with main radiation directed to the sky is required. The exact

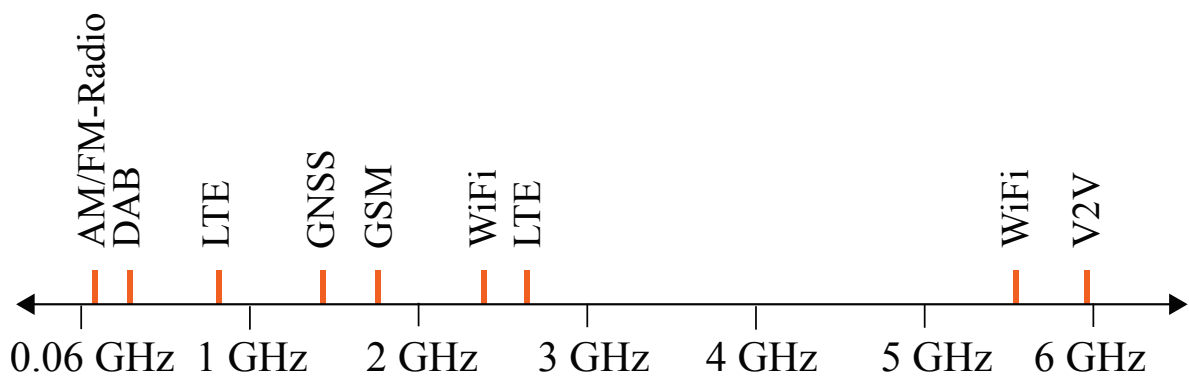


Figure 4.1 Schematic frequency spectrum covered by current automotive RF systems (not exhaustive)

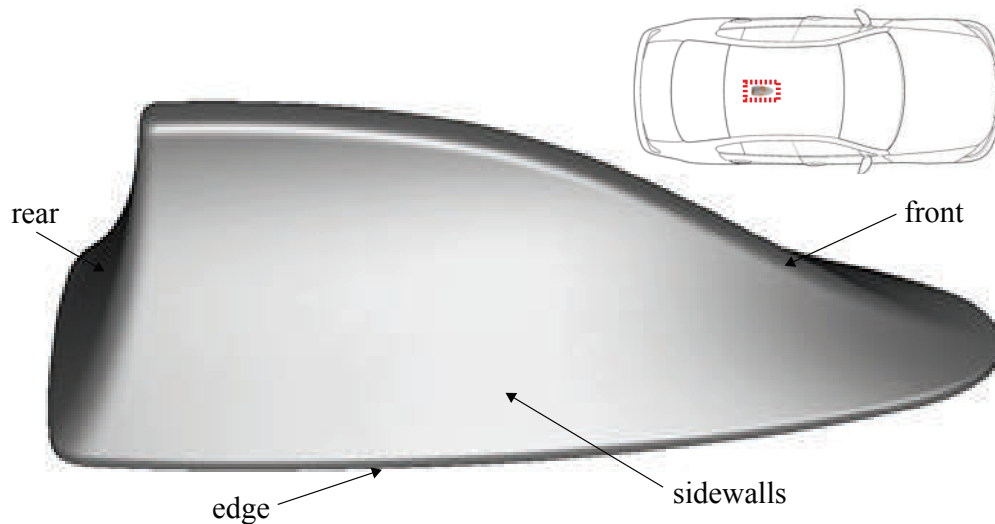


Figure 4.2 Roof antenna module as installed on BMW (sedan type vehicle)

angular coverage varies for different satellite communication standards as for example the global navigation satellite system (GNSS) or the North American satellite radio (SDARS). The polarisation primarily used for such applications is circular.

Considering the boundary conditions on the plane metallic surface of a vehicles roof, monopole structures are used for terrestrial services. These are realised as circuit boards often with additional matching networks. In case of a roof antenna module as shown in Fig. 4.2 these antennas are installed in the middle of the plastic cover, which is installed on the vehicle roof. In doing so the maximum possible height can be used. For satellite communication patch antennas are primarily used. These planar antennas are in many cases integrated on high permittivity substrate materials. The high permittivity leads to a reduction of

the antennas dimensions. Due to the low signal strengths an additional low noise amplifier is installed at the feeding point. This often requires the integration of an additional circuit board.

The plastic cover (Fig. 4.2) has a maximal height of $h_{\text{cover,max}} = 62.7$ mm at the rear. Considering the wavelength of lowest frequency band ($\lambda_0 = 380$ mm at $f = 790$ MHz) that has to be covered by these antenna systems, it becomes clear that integrating a monopole, with $\lambda/4 = 95$ mm, is impossible. Considering that a MIMO antenna system often requires two or more of these antennas to be integrated under this plastic part, the design challenges become clear. In MIMO systems a high coupling of the antenna elements leads to a reduced performance [45]. Positioning the individual antennas further apart is one way to reduce coupling, but this in turn requires more space for installation. Summarising, it can be said that an efficient usage of the available space seems to be one main factor in the vehicular antenna development.

For future vehicle antenna systems, design aspects on the one hand and the technical requirements on the other hand require an analysis of alternative installation spaces. Resulting of the digital dividend II the frequency range will be decreased to lower frequencies down to $f = 690$ MHz ($\lambda/4 \approx 110$ mm). These longer wavelengths lead to an increase of the antenna dimensions. Under the plastic cover currently used for the roof antenna system, an integration of these antennas is difficult or even impossible, especially with regard to the required bandwidth. In addition to the changes in established communication systems, new radio standards must also be taken into account in the development of vehicle communication systems. One of those future RF application is the autonomous driving functionality. This requires a vehicle-to-vehicle (V2V) communication and additionally suitable sensors must be integrated, e.g. radar sensors. These systems make particularly high demands on the function of the single antenna. This is due to the fact that these systems are safety relevant and require a very high reliability. This means e.g. that the antenna characteristics have to cover the environment properly without a degradation due to effects of the integration. With regard to the electromagnetic function, this fact contradicts the demand for highly integrated antennas, as they arise for installation spaces such as the roof antenna module.

Besides the aspects of the available space for the installation, another important point is the data processing. Depending on the transceiver architecture a centralised antenna design approach as well as a distributed approach is conceivable from the vantage point of the present. A centralised design

approach integrates all antennas in one installation space. This will cause a high integration level that leads to integration effects, for instance high mutual coupling or pattern degradation. A considerable influence on the performance can be expected. Thus, decoupling is an increasingly important design goal for centralised design concepts. Furthermore, the antenna design should consider the compensation of occurring pattern degradations. For antenna systems using a distributed approach the single antenna elements are positioned distributed over the vehicle body. Positioning the antennas in that way leads to specific demands concerning the antenna radiation characteristics and polarisation. Radiation characteristics for terrestrial radio services in a distributed design may not be omnidirectional in horizontal plane, as it is often required for current antenna systems which are installed on the roof-top. In distributed architectures, the radiation characteristics that can be generated are more dependent on the respective installation space. Developing such an antenna system all single radiation characteristics have to be designed to complement one another. In summary, the different requirements resulting from the transceiver architecture require a high flexibility in the antenna development.

As already mentioned, not only the function of the antenna system but also the vehicle design is increasingly important. If possible, the communication system should be integrated into a space already defined by the vehicle design. Additional integration spaces, such as the roof antenna system (Fig. 4.2) currently used, may be not available for future designs.

The following findings on the development of vehicle antenna systems can be derived from the aforementioned:

- An efficient usage of the available space is one main factor to meet the functional requirements.
- Design constraints require a development process that takes into account existing installation spaces or better directly incorporates them.
- Requirements arising, for instance, from the transceiver architecture require a high flexibility in the development process of a vehicular antenna system.

3D manufacturing allows for a selective 3D metallisation of nearly arbitrary shaped plastic parts. This results in a high flexibility and volume efficiency in the development process of electronic devices. Furthermore, 3D manufacturing

methods inherently include mechanical parts in the design process, so that already existing parts can be utilised for a further, electric or electromagnetic function. These aspects motivate the evaluation of the use of 3D LDS manufacturing for vehicular antenna systems carried out in the following.

The investigation is divided into two steps. Firstly, the installation space underneath the roof-top antenna module, shown in Fig. 4.2, is evaluated. The results will be compared to a reference system in Sec. 4.1. For future antenna systems an analysis of the vehicle body is carried out. Possible installation spaces are defined considering the requirements on future RF systems in Sec. 4.2.1. Based thereon, a concept for a centralised antenna system is developed using the possibilities of 3D manufacturing in Sec. 4.2. The system is fabricated with the LDS process, characterised and further evaluated in Sec. 4.2.3.

4.1 3D Roof-Top Antenna System

As described above, a common installation space for vehicular antenna integration is under an plastic cover which is installed on the vehicle roof, as shown in Fig. 4.2. In this case the antennas are usually implemented as planar structures on printed circuit boards, which are installed as shown in Fig. 4.3. The feeding is done via circuit board connectors and routed through an opening in the metallic vehicle roof. RF services that are currently covered by such an antenna module are cellular mobile services (e.g. LTE, GSM), WiFi and satellite communication (e.g. GPS). MIMO antenna systems which consist of two single radiators are frequently used for mobile communications and WiFi.

The antenna development discussed in the following is partially based on the contents published [AF8] (© IEEE 2013) and [AF6] (© Springer Vieweg 2014). The usable installation space is determined by the external dimensions of the plastic cover of the currently used roof antenna module of a BMW sedan type. The inner dimensions of the plastic part can be modified as needed for the application but considering the manufacturability. The antenna system should consist of two two-antenna systems to allow for MIMO communication. One system for cellular mobile communication (LTE) and a second system for V2V communication. The operating frequencies of both systems cover the lowest and the highest frequencies currently used in connection with the roof antenna module. The underlying requirements on both systems are depicted in Tab. 4.1. The main objective of the development is using the design scope of the 3D manufacturing to optimise the antenna performance regarding the radiation

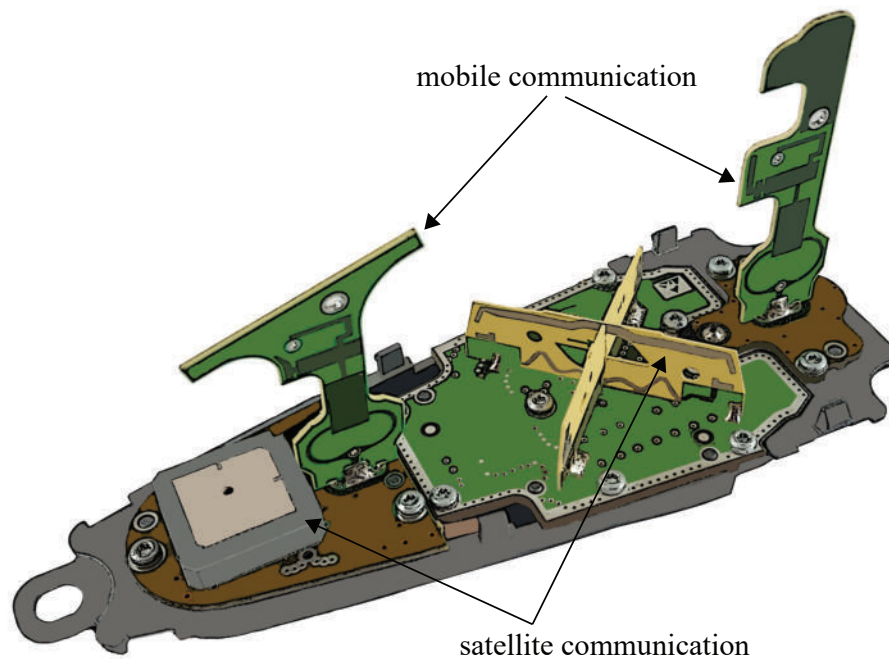


Figure 4.3 Vehicle roof-top antenna system

characteristic and inter-element decoupling.

To efficiently develop the antenna system in terms of space utilisation, the area in which the antennas are placed is chosen as the outside of the plastic cover. Installing the antenna elements on the outer side of the plastic cover maximises the space utilisation on one hand. On the other hand, this would require additional coating of the plastic part. Instead of the outer surface the antennas can also be integrated on the inner side of the plastic part. This would only slightly reduce the space for installation. The plastic cover installed on current vehicles is modified to be manufacturable in a injection moulded process using LDS thermoplastics. In addition, the plastic part is designed to allow the antennas to be properly connected on the inside. The plastic part designed for the following antenna development must be suitable for mounting on the respective production vehicles. This is especially important for a test drive subsequent to the antenna development.

With the metal roof as boundary condition and the requirement for an omnidirectional radiation pattern in the horizontal plane, a monopole antenna is used as the basic model. This approach appears to be suitable for both systems, cellular mobile and V2V communication. For mobile communication a broadband monopole is used for operating frequencies from $f = 1700$ MHz to $f = 2700$ MHz.

Description	Mobile communication	V2V
Operating frequency	791 MHz - 862 MHz 1710 MHz - 1880 MHz 2520 MHz - 2690 MHz	5875 - 5905 MHz
Input reflection (S_{11})	< -10 dB	< -10 dB
Coupling (S_{12})	< -12 dB	< -12 dB
Radiation characteristic	omnidirectional in horizontal plane	omnidirectional in horizontal plane

Table 4.1 Requirements on 3D roof antenna system

To cover the LTE band at $f = 800$ MHz, an additional resonant arm is installed, considering the height of the plastic cover. Routing this arm only vertically like it is done for a $\lambda/4$ -monopole is not possible due to the fact that the maximal height of the plastic cover is only $h_{\max} = 62.7$ mm. Consequently, the arm has to be shaped horizontally to provide the required electrical length.

In the next step the antenna is applied on the outer side of the plastic cover. Firstly, the antennas are positioned opposite to each other on the long side walls of the plastic part. The antennas are aligned inverse and with an offset to each other in order to optimise decoupling. The limiting factor for the positioning of the antennas is the rear edge of the plastic cover, where the height is at its maximum. For the antenna in the front, the sloping edge which leads to a reduction of the height of the plastic cover, is the limiting factor.

As a further configuration, one antenna is placed onto the rear surface of the plastic part while the other antenna is installed on one side wall. The influences on the decoupling and the radiation characteristics are investigated. Since an additional antenna system has to be integrated for V2V communication a configuration leaving one side wall of the plastic cover as space for installation seems to be advantageous. For that reason, this configuration is used in the following.

The two antennas for V2V communication are integrated on the side wall opposite to the LTE antenna in the front. As a result of the functional requirements and boundary conditions, two monopole antennas are developed. Particular attention had to be paid to the feeding. Using a monopole antenna that is very short due to the small wavelength at $f = 5.9$ GHz a feed line must be routed from

the inner edge of the plastic cover to outer surface. Due to the inclination of the roof, an integration of the antenna directly at the lower edge of the plastic part would lead to the antennas being shaded in the driving direction. This can not be accepted, especially for the V2V antenna system with safety relevance. Therefore, a coplanar feed line is used to install the antennas upwards on the side wall of the plastic part. A possible shading of the LTE antennas and vice versa is additionally considered. Since the coplanar lines with their relatively wide ground conductors are located very close to the LTE antenna in the front, a compromise has to be found between the shading effects and the radiation properties of the V2V antennas. To assess the influence of both antennas on each other, the V2V antenna system is placed at different positions on the side wall and the radiation characteristics of both antennas are evaluated. This evaluation showed that the shading effects are low when the V2V antenna system is arranged at a maximum height of $h = 15$ mm from the lower edge of the plastic cover. The distance between the V2V antennas is selected ensuring that the decoupling meets the requirements described in Tab. 4.1.

Fig. 4.4 shows the associated CAD model of the developed antenna system. In addition to both antenna systems, two parasitic elements are installed. The two stripes act as shorted dipoles at $f = 2600$ MHz to influence the radiation characteristic of the LTE antenna integrated in the front. They allow to achieve a higher realised gain of the front antenna in the backward direction (-x). The simple installation of additional parasitic elements to optimise the radiation pattern is a further example of the advantages of 3D fabrication.

In all simulations a simplified model of the SMA connectors which are later used to connect the antennas is already considered. This is required due to the fact that the antennas are fed on a sharp bend on the lower edge of the plastic cover. This has a considerable influence on the input impedance of the antenna. The simulated results are discussed together with the corresponding measurement results of the realised prototype antenna in the following Section.

4.1.1 Prototypical Realisation

The antenna system discussed in the last Section is realised on a thin walled ($t = 1$ mm) injection moulded plastic part using the LDS material Vectra E840i LDS, a liquid crystal polymer, especially suitable for this kind of thin walled injection moulding. The material has a relatively strong anisotropy due to mineral filler as discussed in Sec. 2.4. Due to the thin walls of the

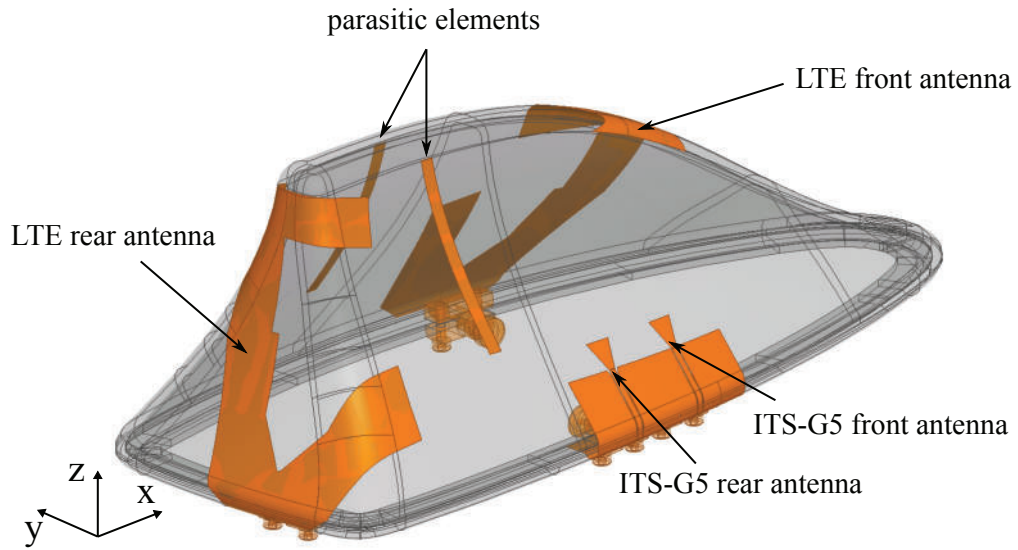


Figure 4.4 Simulation model of the 3D roof antenna system



Figure 4.5 Realised prototype of the 3D roof top antenna system

injection mould the flow direction of the mineral filler can be estimated. The injection point is on the rear of the plastic housing. The thin walls lead to an alignment of the filler parallel to the side walls. The other aspect to be considered in this context is the direction in which the electric field penetrates the filled plastic material. This depends on the electromagnetic structure and may additionally vary for different areas of this structure. Consequently, only approximate values of the effective permittivity can be derived. This is a suitable procedure for the operating frequency range of the antenna system presented here, since the plastic wall is thin in comparison to the wavelength and small variations of the dielectric constant have a minor influence. The permittivity values used for simulations are set to $\epsilon'_r = 3.9$ with $\tan \delta = 0.003$ using the values measured with the cavity resonator at $f = 2.7$ GHz for an electrical field alignment perpendicular to the filler as described in Sec. 2.4. The metallisation is done with Cu/NiP/Au. As derived in Section 2.5.4.1 the losses in Cu/NiP/Au plating are in a similar range to pure LDS copper in the operating frequency range of the antenna system.

Fig. 4.5 shows the realised prototype. A SMA connector is installed on the inner edge, as shown in Fig. 4.6a. One small-sized pair of screws fixes the connector to the edge of the plastic housing and the other pair connects the whole structure with the ground plane/vehicle roof. All simulations and measurements in the anechoic chamber are carried out on an aluminium plate with an edge length of $1\text{ m} \times 1\text{ m}$ and a height of $h = 2$ mm as shown in Fig. 4.6b.

In the following, the measurement results are compared to those obtained by an EM simulation with Ansys HFSS 14.0. First, the scattering parameters of both antenna systems are investigated. The results for the magnitude of the input reflection coefficient are shown in Fig. 4.7. The measured results are plotted with continuous lines and the simulated results with dashed lines. The simulated and measured values for both LTE antennas show a good agreement indicating the suitability of the electromagnetic modelling. This includes the material characterisation and estimation of the permittivity value explained in the last Section. Furthermore, the good match indicates the accuracy of the subsequent fabrication process of the 3D shaped plastic part. The input reflection coefficient is $|S_{11}| \leq -10$ dB in all operating frequency ranges as required.

The measured and simulated magnitude of the transmission coefficient is shown in Fig. 4.8. The transmission coefficient is $|S_{21}| < -12$ dB for all antenna elements operating above $f = 1700$ MHz. For the frequency range at $f = 800$ MHz the transmission between both LTE antennas is $|S_{21}| = -11$ dB (measured) and $|S_{21}| = -9.5$ dB (simulated). The antenna system does not exactly meet the

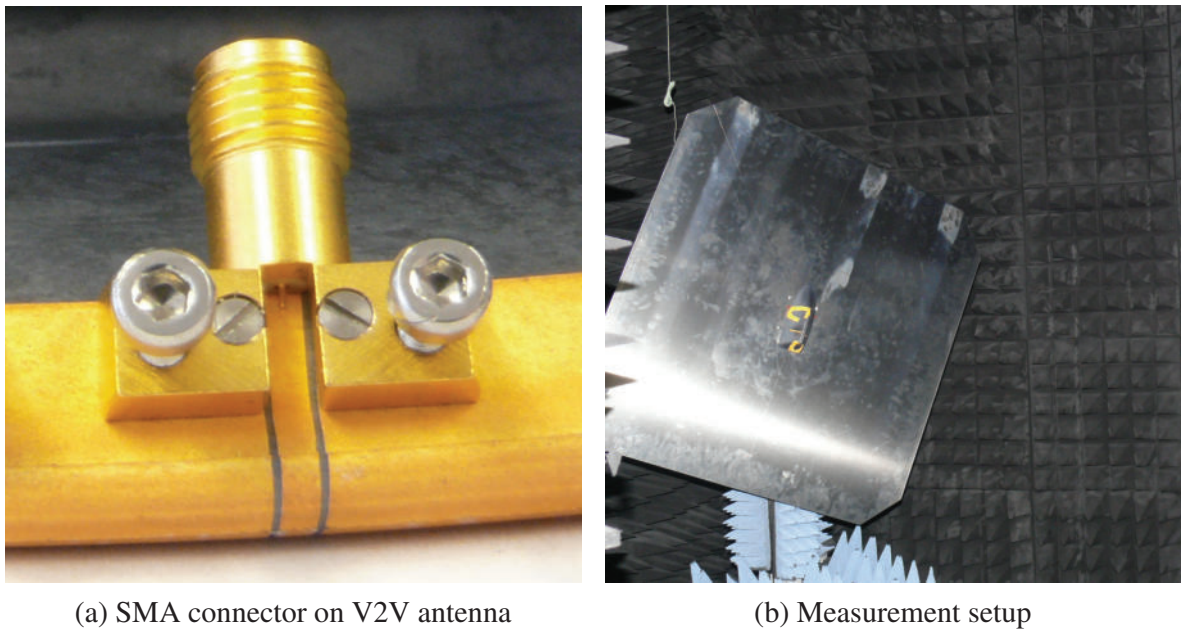


Figure 4.6 Mechanical configuration of realised prototype of 3D roof antenna system

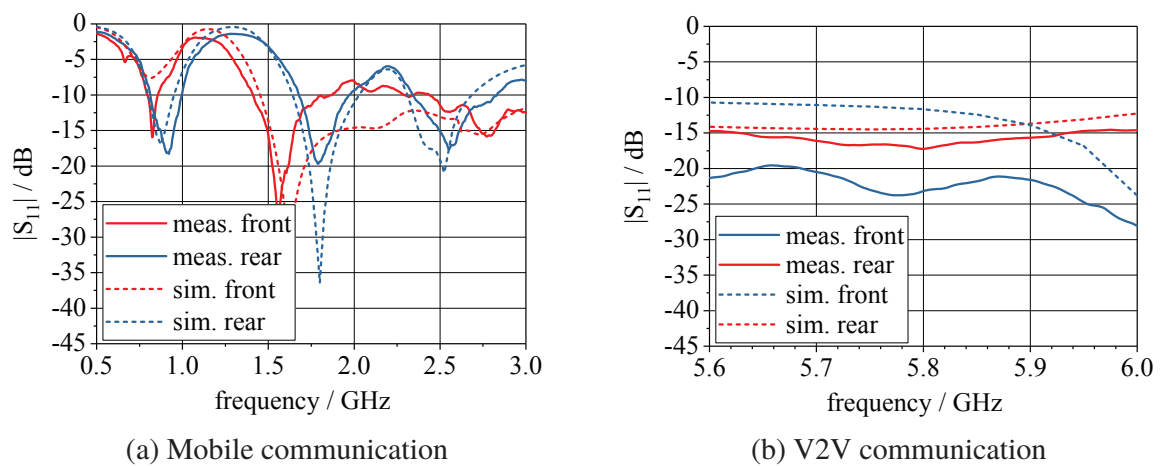


Figure 4.7 Simulated and measured magnitude of the input reflection coefficient for 3D vehicular roof antenna system

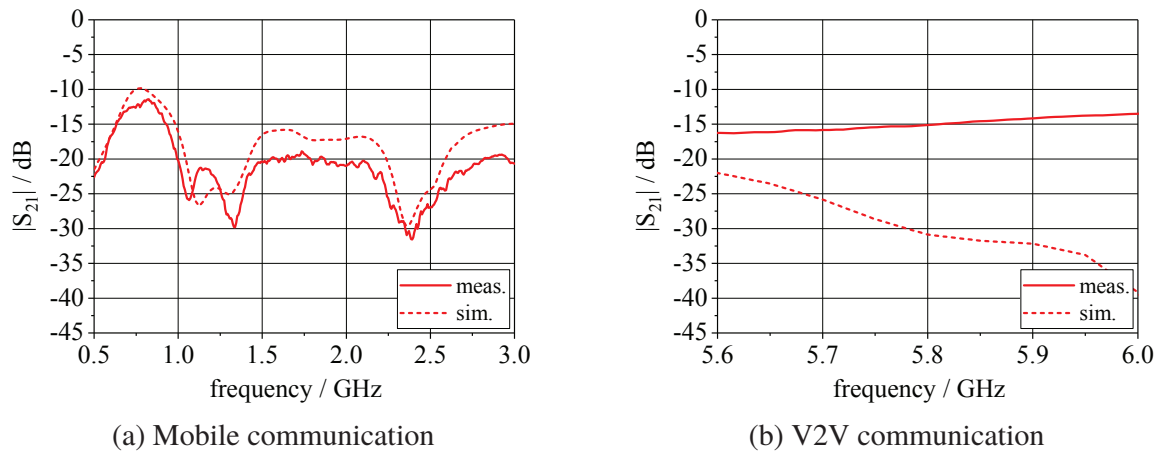


Figure 4.8 Simulated and measured magnitude of the transmission coefficient for 3D vehicular roof antenna module

requirements for decoupling described in Tab. 4.1. However, taking into account the size of the installation space in comparison to the wavelength, the result is sufficient and therefore not further optimised.

For the V2V antenna system, there are differences between the measured and simulated results in both, the reflection and transmission coefficients. This may be due to deviations of the effective dielectric constant, but also to differences in the mechanical installation of the SMA connector. These effects can be expected to have a stronger influence at higher operating frequencies ($f = 5.9$ GHz). Nevertheless, all specifications are met by the antenna system.

The radiation pattern of the antennas are measured in an anechoic chamber. The measurement setup is depicted in Fig. 4.6b. The measured and simulated radiation characteristics are shown in Fig. 4.9 and Fig. 4.10. The measured data are plotted with continuous lines and the simulated with dashed lines. The evaluated elevation angles are $\vartheta = 90^\circ$ and $\vartheta = 80^\circ$, since the radiation properties in and near the horizontal plane are the most critical for a monopole on a finite-sized vehicle roof. As can be seen for both LTE antennas at $f = 800$ MHz and $f = 1800$ MHz the radiation characteristic is omnidirectional. At $f = 2600$ MHz the radiation characteristic shows a reduced gain, especially in the direction in which the other antenna elements are installed. A reduced gain can be observed around $\varphi = 0^\circ$ for the front antenna and around $\varphi = 210^\circ$ for the antenna positioned on the rear wall. The V2V antennas show a nearly omnidirectional

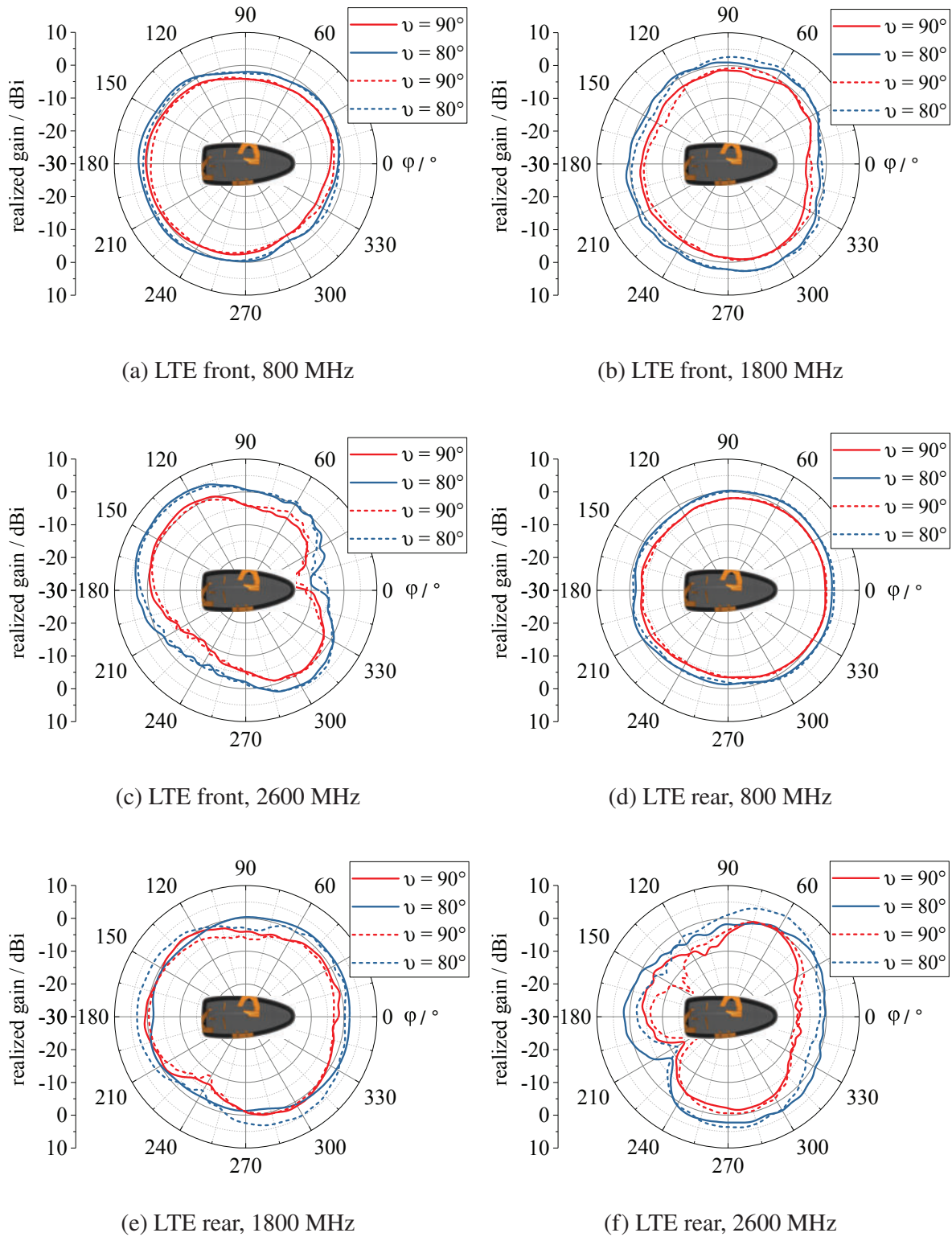


Figure 4.9 Measured (—) and simulated (-----) radiation characteristic of the 3D roof antenna system (LTE)

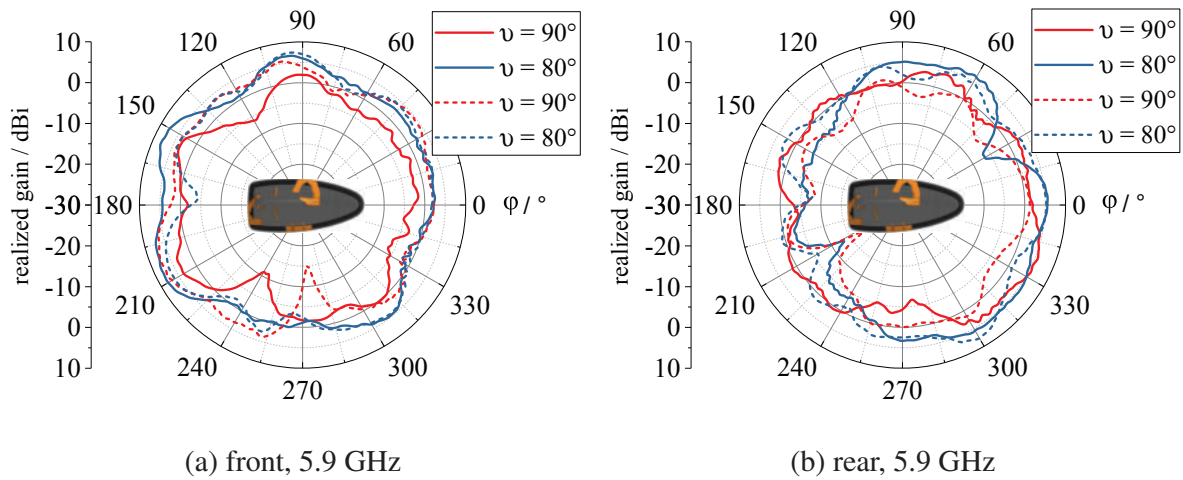


Figure 4.10 Measured (—) and simulated (- - -) radiation characteristic of the 3D roof antenna system (V2V)

behaviour. As for the measurements of the scattering parameters the differences between measurements and simulated data is higher in comparison with the LTE antennas. As described above this may be due to variations of the effective dielectric constant, the mechanical installation of the SMA connector. Since the results in the horizontal plane at $\vartheta = 90^\circ$ show a stronger deviation than at $\vartheta = 80^\circ$, another aspect to consider is the measurement setup. During the measurements the antennas are mounted on the aluminium plate attached to the rotating measuring tower (Fig. 4.6b). When measuring in the horizontal plane, the edges of the aluminium plate and the mounting parts as well as the measuring tower are directed towards the reference antenna. This can lead to reflections, but also to variations due to the radiation at the edges of the aluminium plate, which can not be fully included in the simulations.

The results obtained for the 3D fabricated antenna system on the basis of the measurements of radiation pattern and scattering parameter are not sufficient to describe the performance a possible user can expect. To evaluate the overall performance, parameters based on the system level are more suitable, as described in [46]. Thus, the next Section discusses the evaluation of these system parameters for the proposed 3D antenna system installed on the vehicle roof.

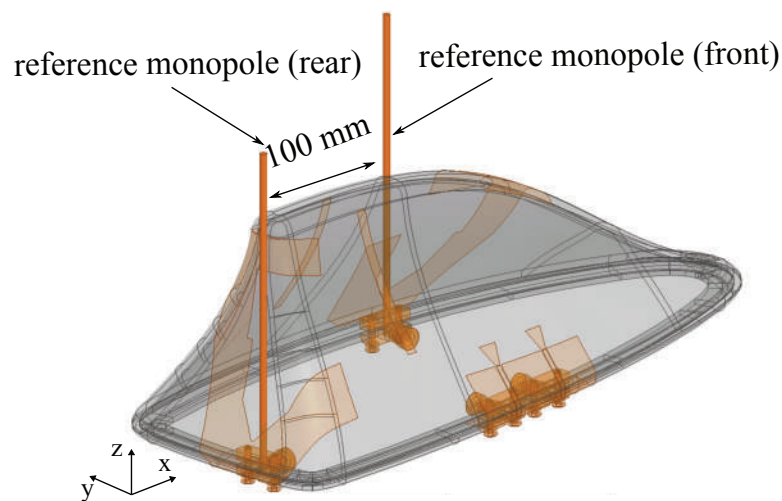


Figure 4.11 Reference antenna system used for performance evaluation of 3D roof antenna module at 800 MHz LTE band ©IEEE 2014 [AP1]

4.1.2 System Level Evaluation of the Integrated 3D Roof Antenna Module

The measurements discussed in the last Section have only limited significance for assessing the performance of the entire radio system integrated on the vehicle. The following measurements are published in the co-authored paper [AP1] (© IEEE 2014). As a first factor influencing the antenna system, the vehicle body as mounting surface will lead to changes in the radiation characteristic and scattering parameters. Furthermore, the scenario the antennas are used in influences the performance of the entire system. Test drives are a suitable way to allow a statistical averaged evaluation of the system performance. For the performance evaluation of a MIMO System the antennas with high coupling are decisive. This is the reason why the following evaluations are carried out for LTE at the $f = 800$ MHz frequency band. To enable an evaluation of the 3D roof antenna system regarding the performance with relation to the utilisation of the available space, a reference system is derived for comparison. The reference antennas are installed at the same feed point, having a separation of $d = 100$ mm. This ensures that the effects due to integration such as positioning on the rooftop or roof insets are also considered. The reference system consists of two $\lambda/4$ -monopoles. The centre frequency is set to the frequency of evaluation $f = 796$ MHz.

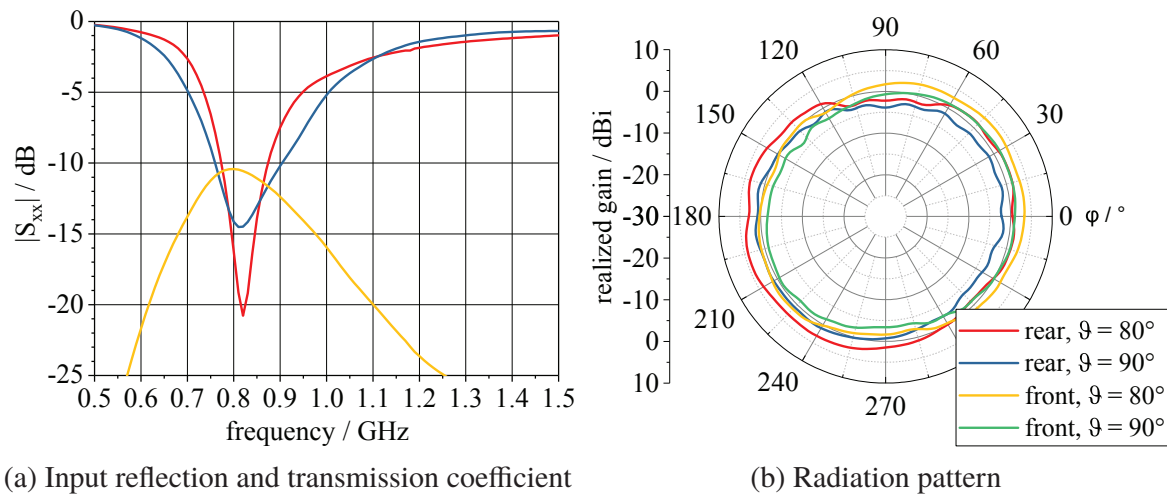


Figure 4.12 Simulated results of the reference antenna system on ground plane © IEEE 2014 [AP1]

Fig. 4.11 shows a model of the reference setup with the plastic cover for comparison. As can be seen the $\lambda/4$ reference monopole antennas are significantly longer than the height of the 3D roof antenna system on the plastic cover. Fig. 4.12 shows the simulated input reflection and transmission coefficient of the reference antenna on a ground plane ($1 \text{ m} \times 1 \text{ m}$). As can be seen, the input reflection of reference and 3D LTE antennas is approximately the same at the frequency of examination. This applies to the magnitude of the transmission coefficient of both antenna systems. Considering the fact that the 3D antenna requires a smaller space for installation, but provides approximately the same low coupling, indicates the advantages of the 3D design approach.

In addition to the evaluation of the RF characteristics, both antenna systems are evaluated in a test drive scenario on a predefined track in Munich. Fig. 4.13 shows both antenna systems installed on the vehicle for the test drives. Both antennas are connected through an opening in the roof. To include the influences of mobility and the effects due to varying channel conditions, the measurements are carried out in an dynamic environment. The test track of 9 km length is in the city of Munich, Germany. The measurement procedure is proposed in [46]. The values evaluated are the system level indicators, channel capacity and condition number. The concrete measurement setup is discussed in detail in [AP1] (© IEEE 2014). The measured complementary cumulative distribution function (ccdf) of the channel capacity C and cumulative distributions function (cdf) of the condition number κ are depicted in Fig. 4.14a-b. According to the

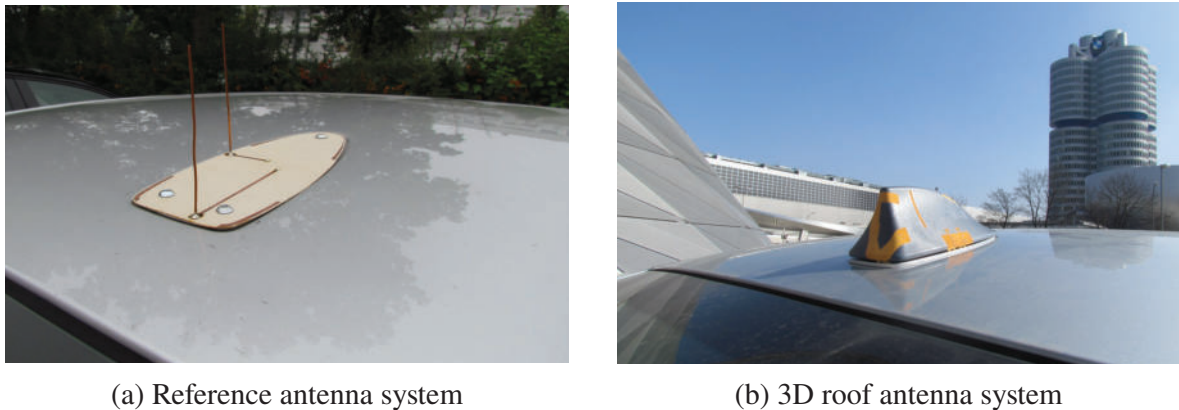


Figure 4.13 Antenna systems integrated on sedan type vehicle © IEEE 2014 [AP1]

measurement and evaluation method described in [46] for the ccdf of the channel capacity, higher values indicate better performance. For the cdf of the condition number, lower values indicate better performance.

The results in Fig. 4.14 show a better performance for the 3D roof antenna module. The 3D antennas mean condition number is decreased by 1.42 dB to $\kappa_{\text{mean}} = 15.95$ dB, which proves the good performance regarding its overall MIMO efficiency [46]. Concerning the channel capacity, the 3D roof antenna system shows an improvement of mean channel capacity by 1.55 bit/ (s Hz) to $C_{\text{mean}} = 6.52$ bit/ (s Hz). These measurements show a better overall performance of the 3D roof antenna systems compared to the reference setup. The main difference in the radiation characteristics of both antennas is that the reference antenna has a low gain at low elevation angles $0 \leq \vartheta \leq 35$ due to the zero in the radiation pattern of the monopole. Because of the top loading of the 3D antenna system the antenna shows a higher radiation for low elevation angles. In addition, the 3D antenna not only provides vertical polarisation as the reference antenna, but also horizontal polarisation due to the top-loading.

The investigations indicate that the design scope gained of 3D manufacturing can be useful to develop antenna systems. The antenna system discussed above shows the utilisation of an already existing installation space. In the following Section, new approaches for vehicular antenna integration on the basis of 3D manufacturing are investigated.

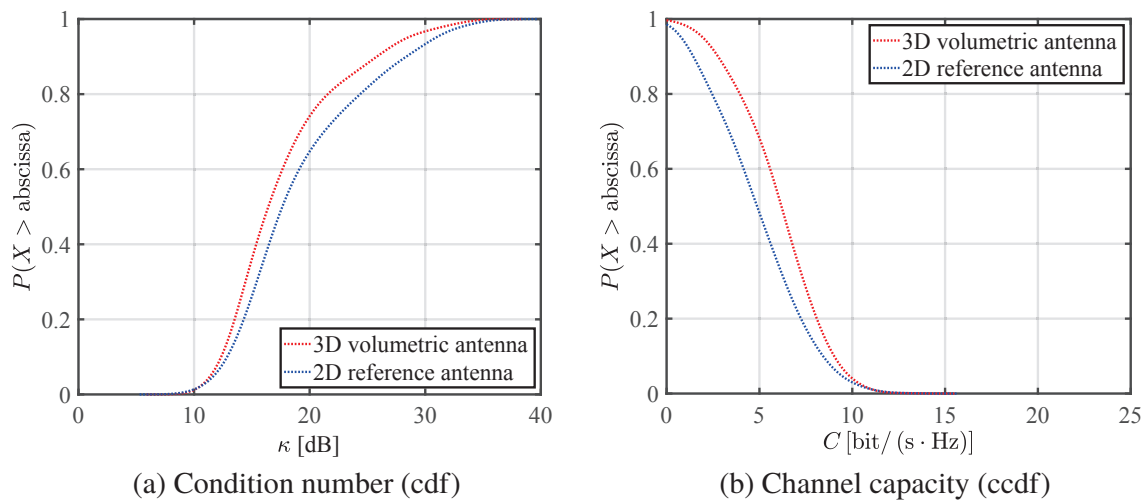


Figure 4.14 Measured system level parameters for reference and 3D antenna system for test drives on a sedan type vehicle © IEEE 2014 [AP1]

4.1.3 Conclusion

The main insights gained by the development of the 3D antenna system on the basis of a roof antenna module as discussed above are:

- LDS fabrications allows for an integration of the antenna using a given space efficiently. This is achieved by applying the antennas on the surface of a plastic part that surrounds the whole or only a part of the installation space which is designated for antenna integration. In doing so, the maximal volume can be used for integration.
- The application of several antennas on one plastic part takes into account the other antennas inherently in the development process. This is particularly important in order to obtain a proper function with regard to the MIMO performance.
- The integration of antennas on one plastic part allows to use additional metallised elements on the surface to compensate integration effects like e.g. a pattern degradation. These metallised elements can be applied causing no considerable expense.

Description	LTE/GSM	V2V	WiFi
Operating frequency	791 MHz - 862 MHz	5875 - 5905 MHz	2450 - 2550 MHz
	1710 MHz - 1880 MHz		5400 - 5500 MHz
	2520 MHz - 2690 MHz		
Input reflection (S_{11})	< -10 dB	< -10 dB	< -10 dB
Coupling (S_{12})	< -12 dB	< -12 dB	< -12 dB
Radiation	omnidirect. in horizontal plane	omnidirect. in horizontal plane	omnidirect. in horizontal plane

Table 4.2 Requirements on vehicular antenna system for a conformal integration

4.2 3D Antenna System for a Conformal Integration

The following Section discusses the development of an conformal integrated antenna system using 3D LDS fabrication. The functional requirements are depicted in Tab. 4.2. Compared to the roof antenna system discussed in the last Section, the system should also cover WiFi communication. This functionality should be realised together with the V2V communication as a single antenna system. The antenna system should use multiple antennas (MIMO) as it is defined in the specific communication standard. For cellular mobile communication (LTE) a four-antenna system should be developed, while for the WiFi and V2V communication a two-antenna system is to be designed. All antenna systems are for terrestrial radio services. Consequently, a radiation pattern with an omnidirectional characteristic in the horizontal plane is required. In addition, the antenna system should be integrated into a joint installation space to allow efficient data processing.

4.2.1 Vehicle Integration Spaces for Conformal Antenna Integration

First of all, an investigation of possible installation spaces for conformal antenna integration is carried out. Assessing the suitability of installation spaces for RF applications, the prevailing boundary conditions will have the main influence, as they have a decisive influence on the electromagnetic properties of the an-

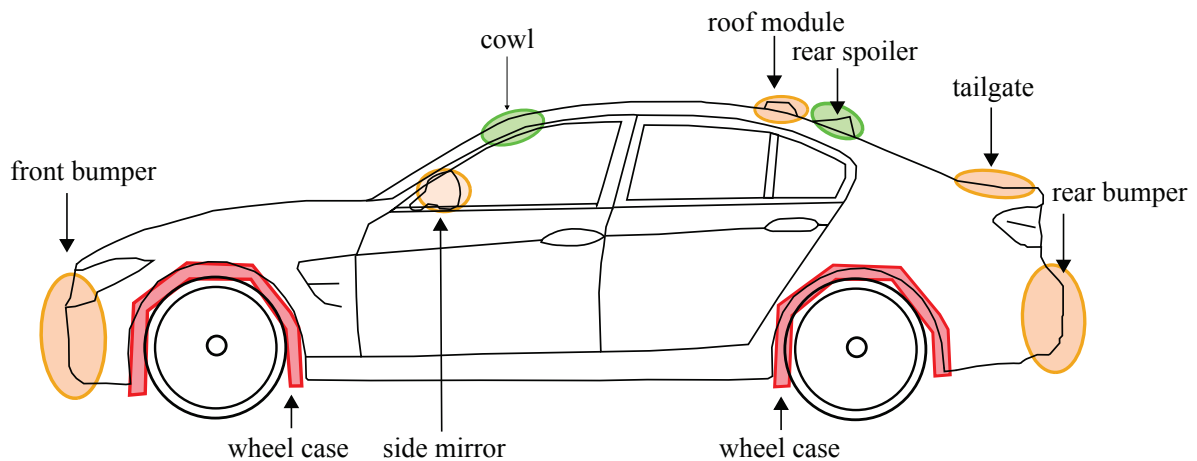


Figure 4.15 Possible vehicle integration spaces, marked according to their suitability for antenna integration using a central integration approach

tennas. If an installation space offers suitable boundary conditions for antenna integration depends on the type of antenna used, the operating frequency and the required radiation characteristic. The vehicle body typically consists of different metal parts. Since metal enclosing an radiating element would shield the electromagnetic waves, the installation of the antennas must concentrate on spaces that allow for a proper radiation. Besides metal body parts there are additionally non metal parts, like the glass windows, plastic bumpers, side mirrors and plastic parts covering, for instance the cowl or a spoiler.

Considering possible antenna types that involve relatively large metal sheets as ground plane, monopole or microstrip antennas are a possible solution. Both antennas require a ground plane that can be provided by the vehicle body parts. From the perspective of vehicle design, the antenna should be mounted as inconspicuously. This is why an integration under or on dielectric parts is intended. In case of a monopole the dielectric plastic part can e.g. be used to route the antenna above the ground plane, the vehicle body. For a planar microstrip antenna the dielectric parts may be used directly as carrying substrate or to cover the antennas.

Based on these fundamental considerations, Fig. 4.15 depicts a vehicle where possible integration spaces are marked which meet the requirement of having dielectric parts covering or closing metallic body parts. The geometric dimensions of such an installation space depend on the vehicle derivative. Additionally, there are some integration spaces that cannot be found on each derivative. Convertibles for example, will not provide an integration space on the roof or inside the rear spoiler. There are also integration spaces that can be found

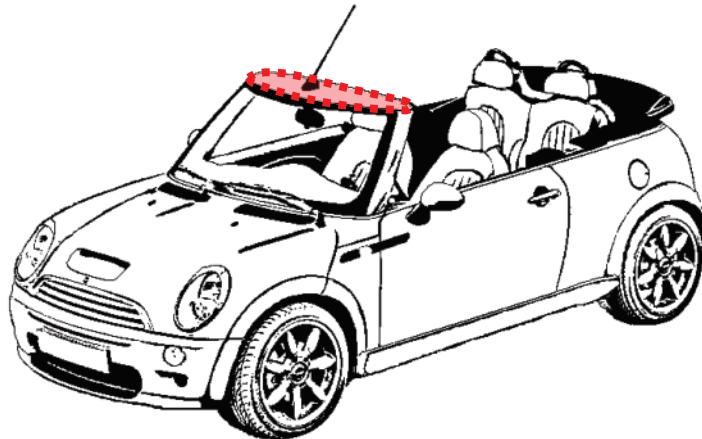


Figure 4.16 Target vehicle with space for installation in MINI convertible (F57)

on each vehicle derivative. Bearing in mind that reducing the complexity of a vehicular RF systems is one way to reduce costs, the antenna integration approach should be independent of the derivative or at least efficiently adaptable. In consideration of these aspects possible integration spaces can be derived.

A further aspect which has to be considered is the radiation characteristic that can be achieved in principle in a specific installation space. For the following antenna development omnidirectional radiation characteristics are required. In the rear and front bumpers the antennas are shielded in the front/rear view. The exterior mirrors only provide good antenna radiation conditions for the right/left side. This also applies to the wheelhouses. Consequently, these positions are not suitable for terrestrial services using a centralised approach for antenna integration. These restrictions for terrestrial services lead directly to integration spaces nearby the vehicle roof. There are plastic parts installed for some derivatives in the front on the cowl or in the back as a rear spoiler. The radiation conditions for terrestrial services seem to be adequate for both of these positions. To integrate all antennas in one installation space sufficient space is required, as it can be found in the cowl as well as in the rear spoiler. Furthermore, these installation spaces have nearly the same size. The developed concept can thus be used for both installation spaces.

The target vehicle for the antenna system developed in the following is the MINI convertible (F57). Consequentially, the cowl is the only possible installation space for this derivative. Fig. 4.16 shows a model of the MINI convertible (F57) with the integration space marked in red.

Fig. 4.17 shows the schematic model of the body panel of the cowl and the

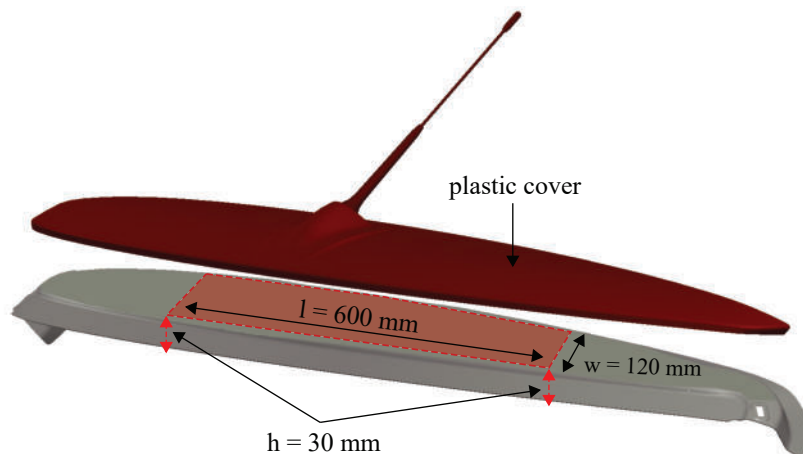


Figure 4.17 Close up of the defined installation space in MINI convertible (F57)

covering plastic part. As current vehicles of this type use a rod antenna for AM/FM reception, a rod can be seen on the plastic cover. The length of the current metal part is about $l = 1.20$ m. The width in the middle is about $w = 20$ cm. The height measured between the metal parts supporting the plastic cover of the current body part varies. In the middle the height is about $h = 30$ mm in an area of about 200 mm \times 120 mm. On both sides the height is only $h = 25$ mm. For the integration of the antenna system developed in the following, the body part currently used is modified taking into account the external dimensions. The resulting space for antenna integration is defined to a recess with 600 mm \times 120 mm \times 30 mm that is integrated in the cowl as marked in red in Fig. 4.17.

4.2.2 Antenna Development

Due to the dimensions of the installation space defined in the last Section, the main objective of the subsequent development process is to reduce the height of the antenna for LTE communication. Besides the limitation in the height ($h_{\max} = 30$ mm) a further aspect is the integration in the vehicular installation space providing a minimal degradation of the antenna characteristics and a low mutual coupling. Furthermore, the cost efficiency of the manufacturing and flexibility to adapt the antenna system on different vehicle derivatives should be considered.

First, some general considerations are made regarding the development of the

antennas in order to design the 3D Substrate mechanically. With the requirement of an omnidirectional characteristic in horizontal plane and the boundary conditions that can be found in the metallic recess, an antenna that is based on a monopole is again a suitable concept. The limited height of $h_{\max} = 30$ mm will lead to a operating frequency of about $f = 4$ GHz for a $\lambda/4$ -monopole. The lowest operating frequency band starts at $f = 791$ MHz. An antenna that is based on a monopole has to be shortened for the underlying installation space. To provide the electromagnetic length the monopole can be routed partially horizontally like it is done for the roof antenna module discussed in the last Section. This is widely known as top-loading and a method frequently used. With the possibilities of 3D manufacturing and the installation space discussed here such a horizontal routing could be done conformal to the plastic cover of the cowl, for example. In doing so the available space is utilised efficiently. To induce a resonance which allows a $\lambda/4$ -monopole antenna operating at $f = 800$ MHz (LTE) $3/4$ of the length has to be routed horizontally. The large capacitance to the ground plane generates an input impedance with a very low real part and a highly capacitive imaginary part. This leads to a high input reflection coefficient in a 50Ω system.

One approach to compensate such a large top-load is using a shorting post. Shorting the top-load reduces the capacitive imaginary part. By placing the shorting post at a suitable position on the surface of the top-load, the antennas input impedance can be matched to 50Ω . Additionally, the resonance frequency and the bandwidth can be varied within limits. In addition to the placement of the shorting, the shape of the top load may have an influence on the antenna characteristics. On the basis of a simplified model different shapes for the top-load are evaluated. These investigations show that the shape of the top-load has only a minor influence as long as the dimensions of the area covered remains the same. In concern of the 3D design scope, this allows to adapt the top-load efficiently on the available installation space. Besides the operating frequency band around $f = 800$ MHz the antenna system has to cover frequencies around $f = 1800$ MHz and $f = 2600$ MHz. To cover these operating frequencies, an additional arm can be added to the monopole that provides a broadband behaviour for frequencies above $f = 1720$ MHz.

On the basis of these general investigation of the antenna concept, a 3D substrate is developed using a MCAD tool. Fig. 4.19 a shows the corresponding model of the developed plastic part. The 3D substrate consists of a vertical part on which the broadband monopole is routed. By a 3D surface modulation in undulating form more length is obtained. The specific form of vertical surface modulation

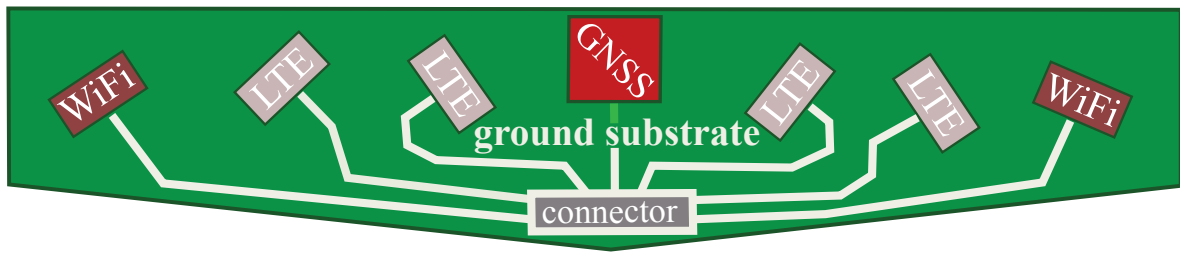


Figure 4.18 Schematic sketch of 3D substrate integrated on ground substrate with centralized feeding area

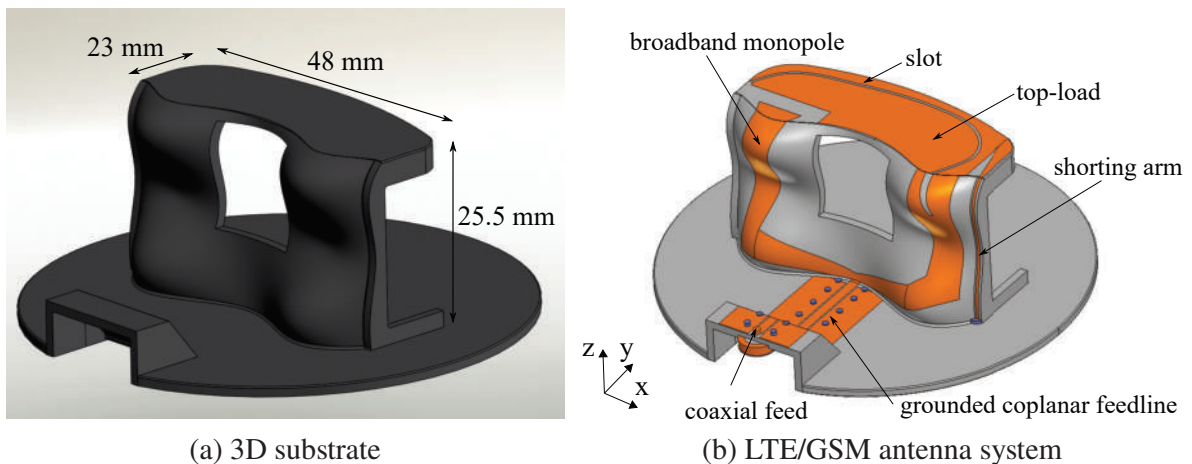


Figure 4.19 3D substrate part of the antenna system for integration in coil of convertible

is chosen as just one example of the use of 3D manufacturing. A horizontal planar surface is added to the vertical substrate to route a possible top-load on. The top-load is not shaped conform to the plastic cover of the cowl because of limitations in the fabrication of the prototype antenna. For the prototypical realisation of this antenna an additional circular ground plate is added. An area to mount a connector for circuit board installation, which is slightly higher than the ground plate, is integrated at the edge. In doing so, a SMA cable can be easily connected without a protruding connector.

The circular ground plate can be replaced by installing the 3D antennas of the entire system directly on a common ground substrate. Connecting the 3D antennas with the ground substrate can be done, e.g. with a clamp. Using a planar transmission line all antenna connections can be routed to a central point on the ground plane to be connected to a data processing unit, for example. Fig. 4.18 illustrates such a configuration.

With a view to possible mass production, the 3D antenna substrate must be

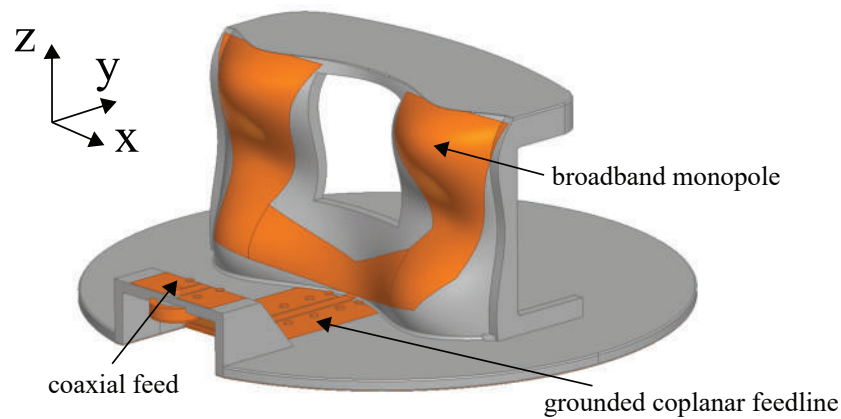


Figure 4.20 CAD model antenna for WiFi/V2V communication as used for EM simulations

efficiently processable by injection moulding. A further aspect that has to be considered is the efficiency of the subsequent LDS structuring. The developed 3D antenna substrate (without the circular ground plate) must be repositioned during structuring once at the most. This reduces the processing time and eases the handling. Using the same substrate to integrate the LTE and WiFi/V2V antenna reduces the part count and complexity additionally.

Fig. 4.19b shows the model of the finally optimised LTE antenna. The different parts of the antenna are marked. The antenna is a broadband monopole covering frequencies from $f = 1700$ MHz (GSM) to $f = 2600$ MHz (LTE). To cover the frequencies at $f = 800$ MHz (LTE), a top-load is added which is short-circuited on the ground plate. From the aspect of manufacturability, routing the shorting along the front of the antenna seems to be the most efficient solution. Routing the short directly beside the monopole arm that feeds the top-load turned out to require the smallest area for the top-load.

Due to the fact that the bandwidth achieved is very small, different methods to enhance the bandwidth are further investigated. It turned out that the combination of the resonance induced by the top load with the resonance of a slot is a solution to achieve an increase of the bandwidth by tuning both resonances close to each other. The slot is routed across the surface of the top-load down on the feeding antenna arm as shown in Figure 4.19b.

For WiFi/V2V communication an antenna is developed on the basis of a broadband approach using a widened monopole. The CAD model is shown in Fig. 4.20. The antenna is routed only on the vertical part of the 3D substrate because a top-loading as with the LTE/GSM antenna is not required, as the lowest operating frequency is $f = 2450$ MHz (WiFi).

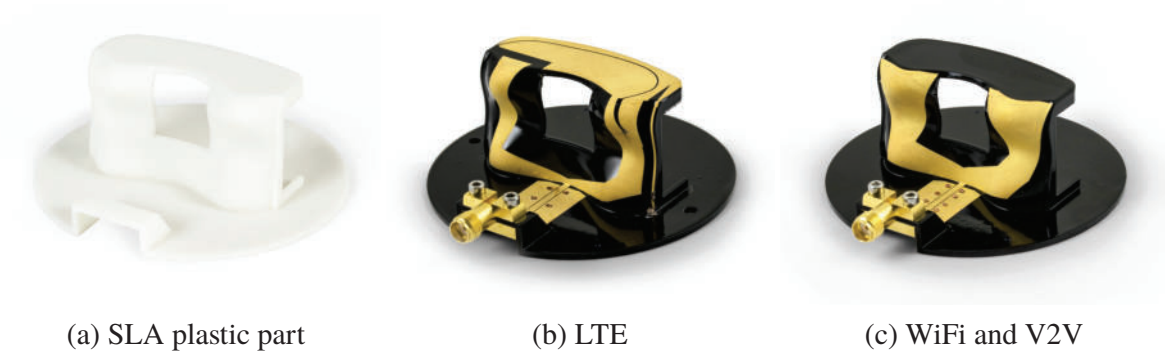


Figure 4.21 LDS fabricated prototype antennas developed for an installation in the cowl of an MINI convertible (F57)

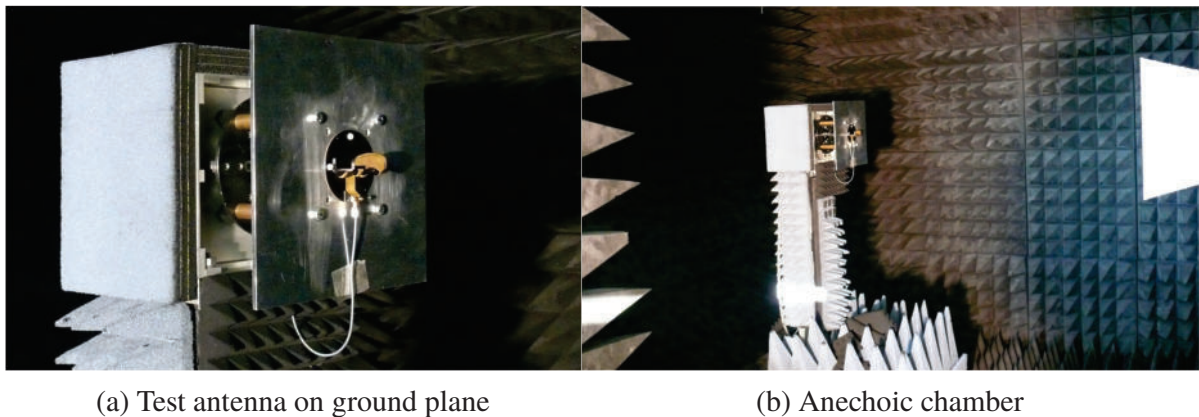


Figure 4.22 Measurement setup for antenna characterisation

4.2.2.1 Prototypical Realisation

Both antennas discussed above are realised using LPKF ProtoPaint LDS. The manufacturing of the plastic substrate part is done using a SLA epoxy resin SL-EP 9000 from SL PROFI - Jörg Grießbach. Fig. 4.21 shows the realised prototype antennas in two different manufacturing steps, the SLA substrate and as metallised antenna prototype. The plastic part of the ground plate is metallised with the same feeding structure for both antennas, LTE and WiFi/V2V. It consists of a grounded coplanar waveguide that feeds the antenna from the heightened plastic part on the edge of the ground plate. A SMA PCB connector is installed, which contacts the antenna for all measurements. By installing the single antennas on a joint metallic ground plate arbitrary antenna combinations

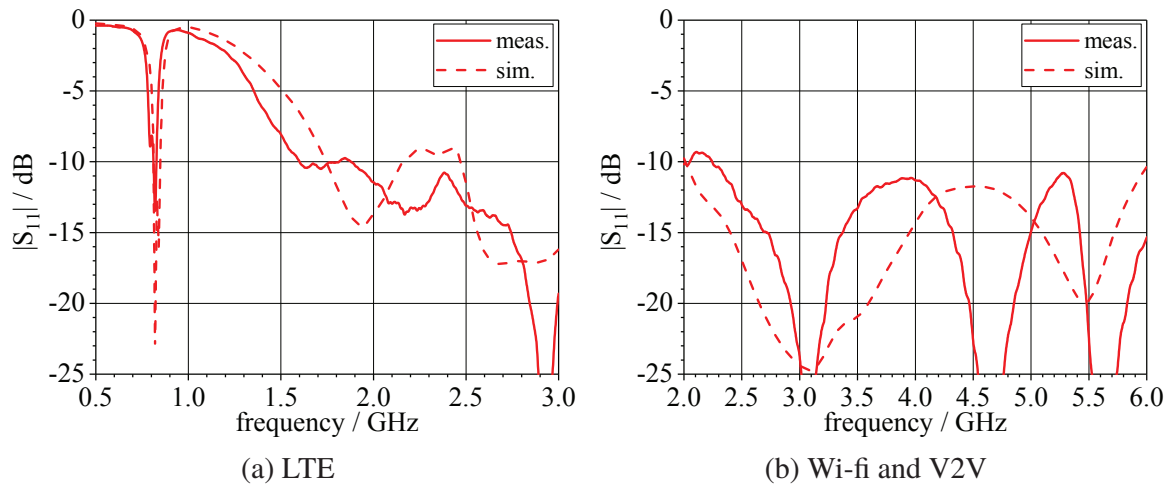


Figure 4.23 Input reflection coefficient of LDS fabricated prototype antenna

can be realised. In that way multiple antenna systems can be evaluated. The RF characterisation and associated EM simulations are performed for both antennas installed on a ground plate with a size of $250 \text{ mm} \times 250 \text{ mm} \times 3 \text{ mm}$ as shown in Fig. 4.22a. The measurement setup with the antenna installed in the anechoic chamber is depicted in Fig. 4.22b.

The measured and simulated input reflection coefficient of both antennas is shown in Fig. 4.23. For the LTE antenna the measured and simulated data show an adequate agreement. The resonance at $f = 800 \text{ MHz}$ as well as the lower band edge of the broadband range show a slight shift to lower frequencies. This may be due to slight changes of the permittivity values of the varnished SLA part. Furthermore, the SMA connector is not considered in the simulations and may also induce slight variations. For the WiFi/V2V antenna there are also differences between the simulated and measured data. Especially, for higher frequencies the influences of the installation of the SMA connector will be more dominant and can cause this deviations. Since the behaviour of the broadband antenna does not change in general, the input reflection coefficient can be found always below $|S_{11}| \leq -10 \text{ dB}$ in all operating frequency ranges.

Fig. 4.24 shows the measured radiation pattern of the LTE antenna in the horizontal plane for elevation angle $\vartheta = 90^\circ$, $\vartheta = 80^\circ$ and $\vartheta = 70^\circ$. As can be seen, the radiation characteristic is omni-directional in horizontal plane for all operating frequency ranges. A good match between simulated and measured data can be obtained for the LTE antenna. For $f = 800 \text{ MHz}$ the partial realised

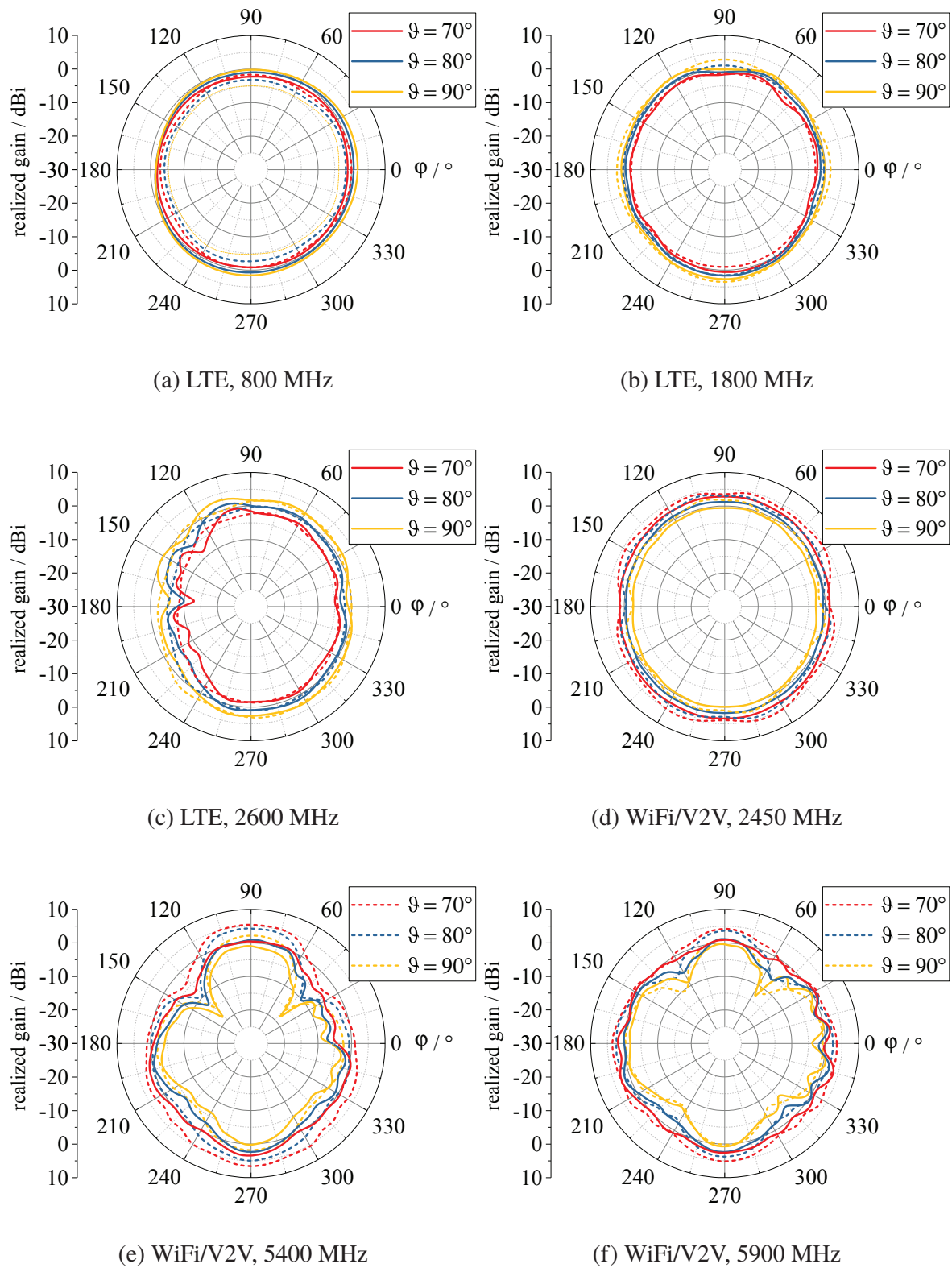


Figure 4.24 Measured (—) and simulated (---) radiation pattern for LTE and WiFi/V2V antennas

gain at an elevation angle of $\vartheta = 90^\circ$ is slightly reduced. This is due to the geometric configuration of this antenna. The antenna has to be routed in the horizontal direction, to reduce the height to $h = 25$ mm. The horizontal routing causes the radiation pattern to be directed to lower elevation angles.

Fig. 4.24 d-f shows the measured radiation pattern of the WiFi/V2V antenna for the elevation angle $\vartheta = 90^\circ$, $\vartheta = 80^\circ$ and $\vartheta = 70^\circ$. As can be seen, the pattern is nearly omnidirectional in the horizontal plane at all operating frequency ranges. At $f = 5400$ MHz and $f = 5900$ MHz the measured partial realised gain is slightly reduced at an elevation angle of $\vartheta = 90^\circ$ and at $\varphi = 60^\circ$ and $\varphi = 120^\circ$. This is the direction of the corners of the metal ground plate where the connecting cable is routed in the middle, as it is shown in Fig. 4.22a. This may cause such variations in comparison to the simulations, especially when measuring in or close to the horizontal plane.

4.2.3 Evaluation of the Conformal Integrated 3D Antenna System

Since the vehicle body mainly defines the boundary conditions of a vehicular antenna in the next step the optimised prototype antenna system is integrated into the vehicular installation space defined above. The evaluation is done on basis of an EM simulation considering the main influencing vehicle body parts. The antenna system consists of a four-antenna system for mobile communication and a two-antenna system for WiFi/V2V communication. The antennas are integrated in a recess in the middle of the cowl as depicted in Fig. 4.25. The evaluation is discussed on the example of the LTE 1 antenna. However, the simulation model takes into account the entire configuration as shown in Fig. 4.25. All orange coloured parts are metal parts, while the grey components are the antenna substrates. The simulations are performed for the MINI Convertible (F57) with the roof opened. In doing so, the metallic cowl is arranged protruding from the rest of the vehicle by the two A-pillars. The effective ground plane for the antennas is thus limited to the cowl.

Fig. 4.26a shows the scattering parameters for the LTE 1 antenna. The reflection coefficient of the antenna on the aluminium plate ($250 \text{ mm} \times 250 \text{ mm} \times 3 \text{ mm}$) is plotted for comparison as dashed lines. As can be seen, the input reflection coefficient is only slightly changed due to the integration. The bandwidth at $f = 820$ MHz is slightly reduced. This indicates that the resonance of the slot and the shorted top-load are shifted closer together as it is described in the last Section. By varying the slot length this effect can be compensated. In

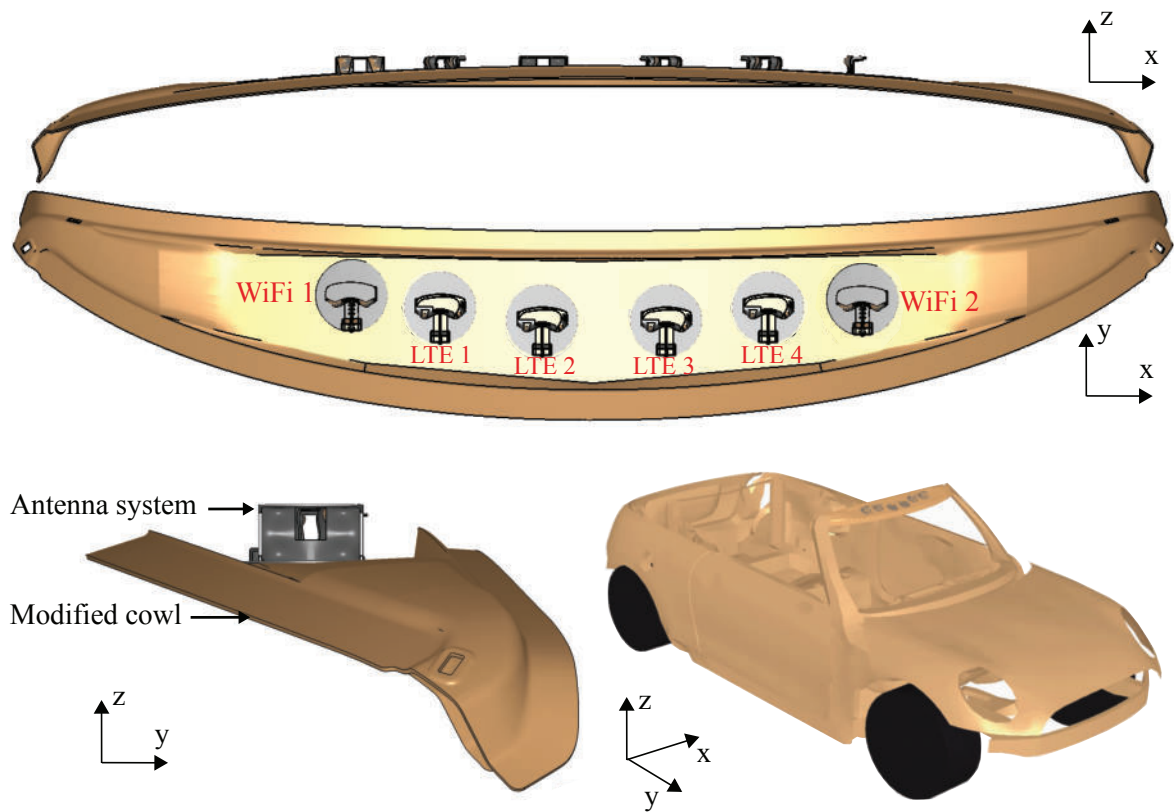
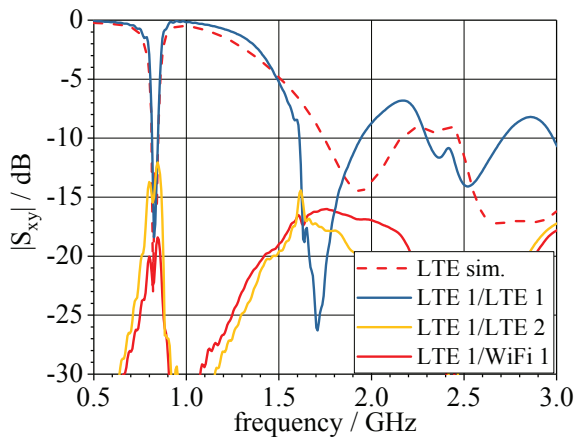


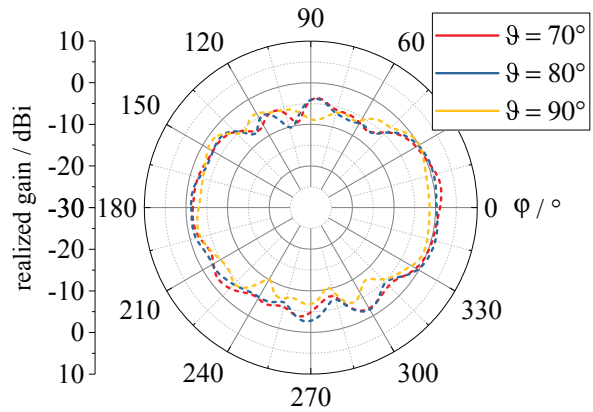
Figure 4.25 Simulation model of the modified cowl with integrated LTE and WiFi antenna systems

the broadband frequency range starting at $f = 1720$ MHz, the lower edge of the band is shifted to lower frequencies, but the principal shape of the curve is not affected. The magnitude of the transmission coefficient is always below $|S_{xy}| \leq -10.5$ dB at all operating frequencies. Fig. 4.26 depicts the radiation characteristic in the horizontal plane for the LTE 1 antenna. The elevation angles depicted are $\vartheta = 90^\circ$, $\vartheta = 80^\circ$ and $\vartheta = 70^\circ$. The radiation pattern at $f = 820$ MHz, $f = 1800$ MHz and $f = 2600$ MHz show an omnidirectional characteristic in the horizontal plane for all elevation angles. At $f = 820$ MHz the radiation characteristic is shaped slightly elliptically due to the shape of the cowl acting as ground plane for the monopole. Furthermore, the partial realised gain is slightly reduced due to the integration in the recess of the cowl.

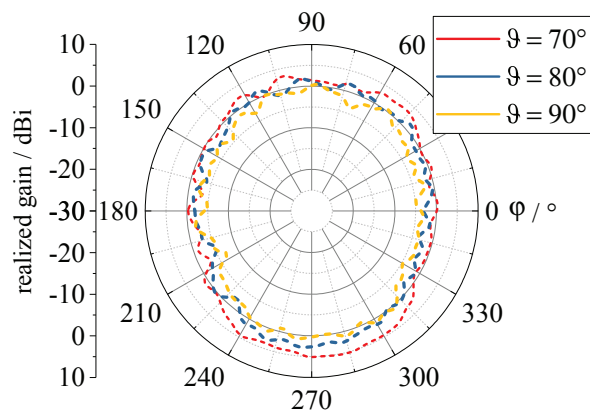
The simulated results of the prototype antenna system show that the integration in the cowl of a MINI convertible does only slightly change the characteristic of the LTE antenna developed and described in the last Section. The antennas are integrated into a recess with a depth of about $d = 12$ mm in the middle. The height of the antenna is $h = 26.5$ mm. The simulations indicate that a suitable shaping of the edges of a recess an antenna system can be installed conform in



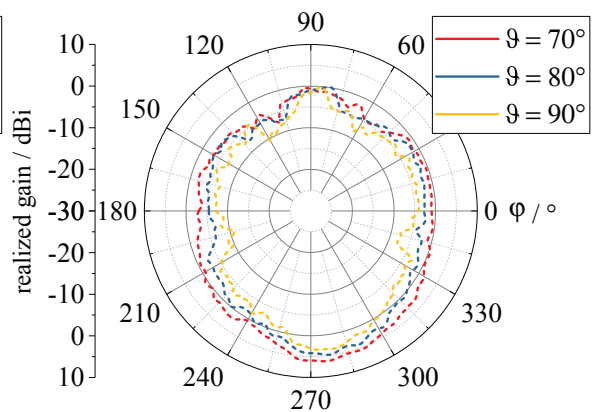
(a) LTE 1, Reflection and transmission coefficient



(b) LTE 1, 820 MHz



(c) LTE 1, 1800 MHz



(d) LTE 1, 2600 MHz

Figure 4.26 Simulated characteristic of the LTE 1 antenna integrated in the modified cowl of a Mini convertible (F57)

the cowl of a convertible, providing an adequate function.

4.2.4 Conclusion

The main insights gained by the development of the conformal integrable 3D antenna system discussed in this Section are:

- For future RF systems that are to be integrated conformal to the vehicle body, installation spaces that are located on the outside and covered by dielectric parts are suitable installation spaces.

- Using 3D fabricated substrates that are especially developed for the antenna allows to influence and thus optimise the antennas characteristic.
- The possibilities of arbitrary shaped 3D substrates allow for an efficient adaptation of the substrate on the specific installation space e.g. an dielectric cover.

3D Fabrication for Microstrip Antennas

The following Section deals with the use of 3D LDS manufacturing possibilities for microstrip antennas. Starting from the basic electromagnetic function of a microstrip antenna, different possibilities for an antenna modification based on 3D manufacturing are discussed in Sec. 5.1. Selected methods are investigated on basis of EM field simulations in Sec. 5.2. These findings are applied on the design of an active GPS antenna system. A prototype antenna is fabricated with LDS method and characterised in Sec. 5.2.2.

5.1 Characteristics of Microstrip Antennas

One main characteristic of microstrip or patch antennas is their low profile, which is frequently designed planar, as this allows the antennas to be manufactured very cost-effectively and in large quantities. Microstrip antennas are used in a wide range of applications [47]. The general structure of patch antennas consists of an infinitely extended or finite ground plane and a metallic, arbitrarily shaped metal patch arranged at a distance h above the ground plane. Due to fabrication matters in a practical realisation the space between ground plane and patch is often filled with a dielectric material with a relative permittivity ϵ_r' and a loss tangent $\tan \delta$. Fig. 5.1 shows the general structure with the geometric and material parameters.

In literature various shapes for the patch can be found [48] [49] [50] [51]. A typical shape is the rectangular patch, or as a special case of this, the quadratic patch (Fig. 5.1b). The investigations carried out in the following uses a rectangular shaped patch as a reference. The results obtained may be adapted on other patch configurations, due to the fact that the electromagnetic principle of radiation of such a structure is similar. The current distribution that can be excited on a patch antenna depends on the respective boundary conditions. Similar to waveguides, the field distributions are referred to as modes and specified according to their sinusoidal solution functions. To excite a specific

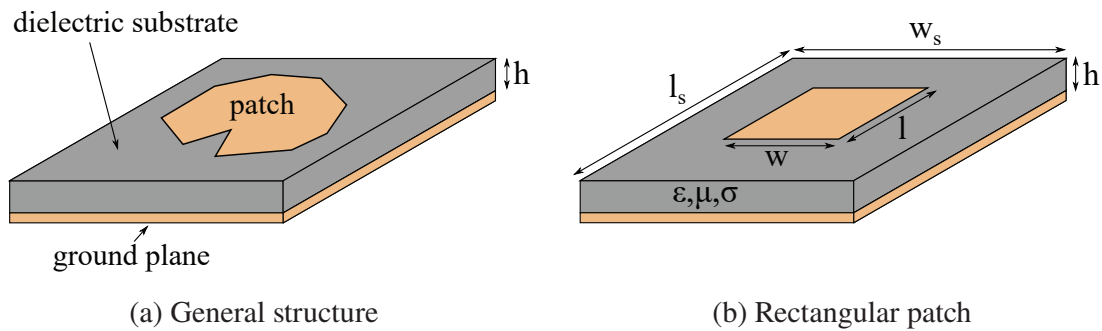


Figure 5.1 Structure of a microstrip antenna

mode on the patch, the feeding must be configured accordingly. Typical feed structures used are coaxial, microstrip or aperture coupled feeds as described in [52]. The type of feeding and its exact position on the patch can be used to influence the input impedance of the antenna for a specific mode. For all investigations discussed in the following a coaxial feed is used. The dimensions and feed position are adapted to the respective antenna configuration. The results gained may be adapted with some exception to other feeding structures. In case of a rectangular patch excited with its fundamental mode the coaxial feed has to be positioned as marked in Fig. 5.2a on the symmetry plane along the x -axis. A shift of the feed along the x -axis varies the input impedance. In this way the antenna can be matched to the feed line [52].

To describe the radiation principle of patch antennas different analytic models are used. This is for example the transmission line model as described in [53]. Another model frequently used is the cavity model as discussed in [54] or [47]. Both models are suitable to describe the main radiation principle and give an understanding on the electromagnetic behaviour. Fig. 5.2b shows a schematic diagram of a rectangular patch with finite substrate and ground plane. The antenna shown is operated in fundamental mode TM_{10} and the associated field distribution in the slot between ground plane and patch are shown.

Along the length l the electric field distribution on each side of the patch shows a sinusoidal distribution. Using the cavity model as described in [47] it can be shown that the far-field due to the fields in this resonating slot is cancelled out in the E- as well as in the H-plane. The currents along the width w are assumed as a constant distribution. Along the width of the patch, the electric field in the slot has a component, which is constructively superimposed in the far field and represents the radiating part. Consequently, the resonating edge l is

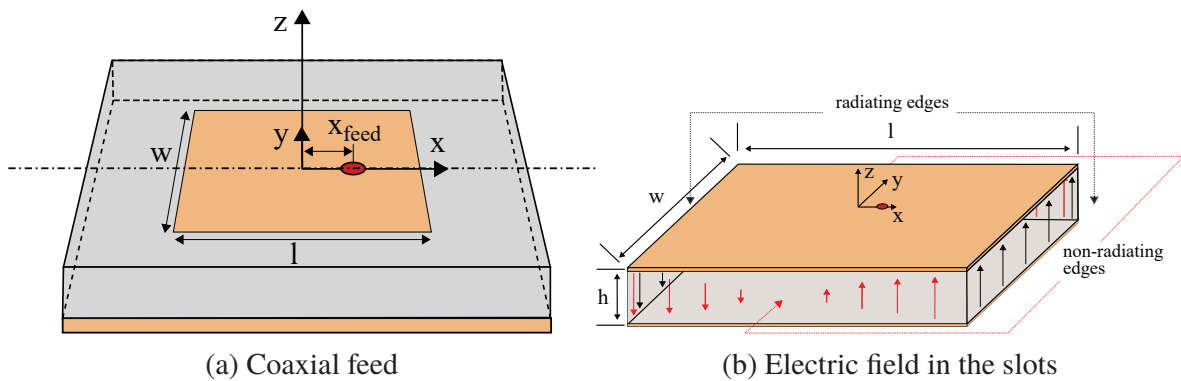


Figure 5.2 Feeding and radiation principle of a rectangular patch excited with its fundamental mode

often called non-radiating edge and the edge along the width w the radiating edge. It has to be borne in mind that this is only a simplified description not considering all occurring physical effects. Nevertheless, it is sufficient to gain a basic understanding in order to be able to derive the principal effects of 3D shaping in the following investigations.

With regard to the 3D modification of microstrip antennas excited with the fundamental mode, the functional principles described lead to the following assumptions:

- An asymmetry of the feed due to a 3D shaping can influence the occurring mode on the patch.
- A modification including the resonating edges may have a major influence on the resonance frequency.
- A modification along the radiating edge (w) may have a major influence on the radiation characteristic.
- Modifications only including the inner area of the metallic patch may be used to influence the mode that is excited on the patch.

In the following evaluations a square patch antenna operating at $f = 5.8$ GHz (ISM band) is used as reference model. The substrate material is Xantar LDS 3720 ($\epsilon_r' = 2.9$, $\tan \delta = 0.005$). The metallisation of the patch and the ground plane are modelled as sheets of perfect electric conductor. The results can be adapted to other frequencies scaling the geometric dimensions of the antenna. Fig. 5.3a shows the geometric dimensions of the reference antenna with $w = l = 14.4$ mm,

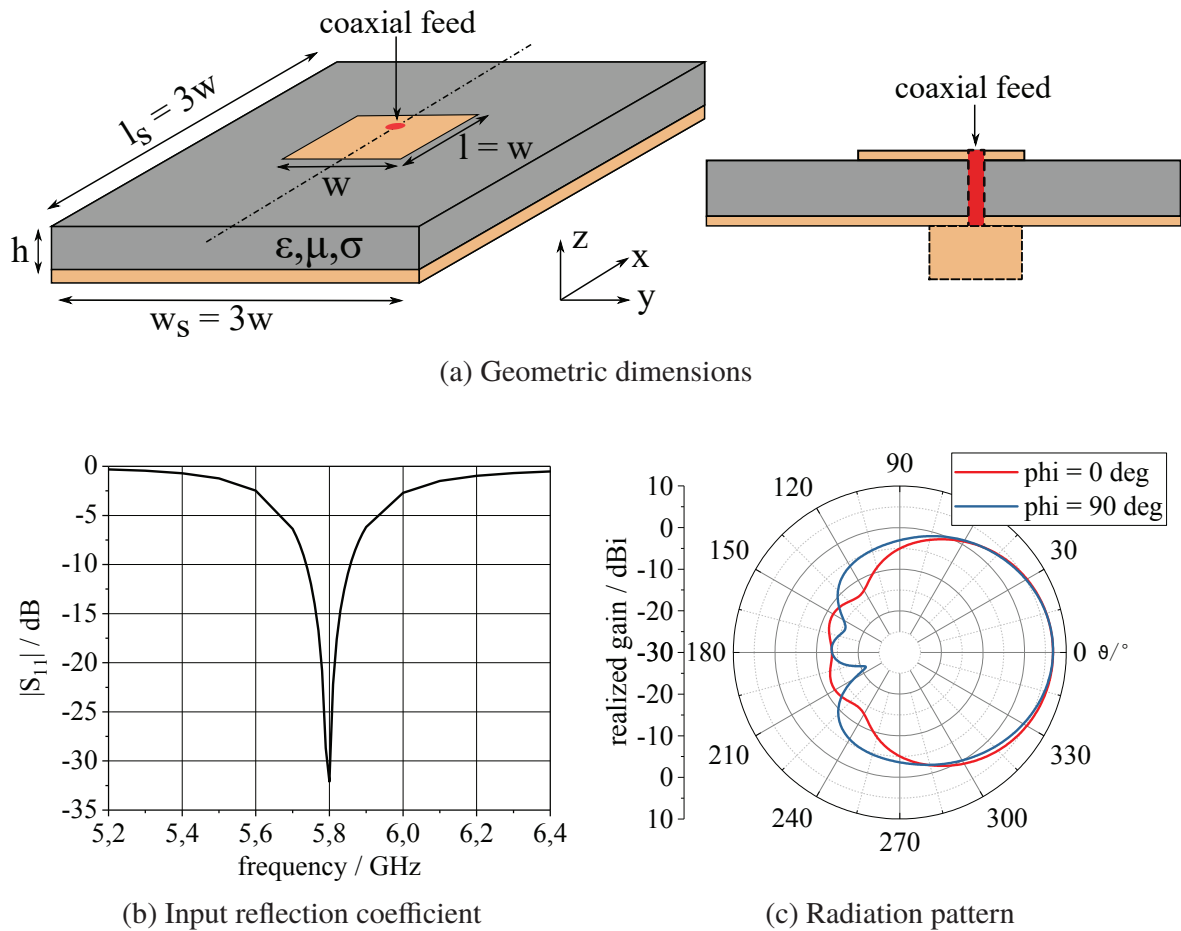


Figure 5.3 Characteristics of a rectangular patch excited with its fundamental mode

$h = 1$ mm and $x_{\text{feed}} = 2.1$ mm.

The associated simulated input reflection coefficient and radiation pattern is plotted in Fig. 5.3b. The 10 dB bandwidth is about $BW_{10 \text{ dB}} = 120$ MHz implying a relative bandwidth of about $BW_{10 \text{ dB, rel}} = 2\%$.

To investigate the effects of a 3D modification, the antenna should be modelled in a way that changes in antenna characteristics by other effects than the 3D shaping are reduced or are at least known. Therefore, the reference antenna configuration is evaluated with regard to the effects of a changed substrate thickness and different values of the substrate/ground to patch edge length prior to the investigation of a three-dimensional shaping.

One effect which influences the characteristic of a patch antenna are surface waves in the substrate. Pozar discusses the influences of surface wave excitation on microstrip antennas in [55]. As described by Pozar surface waves are always excited on patch antennas as the first mode (TM_0) has a cut-off frequency which is

zero. By increasing the height of the substrate, higher order surface wave modes can be excited. In case of an infinite ground plane the excited surface waves are guided on the substrate's surface. In case of a truncated substrate/ground plane the surface waves are partially radiated at the edges of the substrate and superimposed constructively or destructively, influencing the radiation characteristic and the radiation efficiency of the microstrip antenna. Increasing the height of the substrate or the distance between patch and ground plane additionally increases the bandwidth of the microstrip antenna [52]. As an increase of the bandwidth may be a goal of an antenna optimization, a balance between surface wave excitation and increase of the bandwidth has to be found. To keep the surface wave excitation within limits Garg et al. [56] defines the maximal height to:

$$h \leq \frac{0.3\lambda_0}{2\pi\sqrt{\epsilon_r}} \quad (5.1)$$

Evaluating Eq. 5.1 for the reference antenna used in the following leads to a limiting height of $h_{\max} = 1.42$ mm. The reference antenna has a height of $h_{\max} = 1.0$ mm, not exceeding the limit defined by Garg et al.

As described above the lowest order surface wave mode is excited to a certain degree even on microstrip antennas with very low substrate heights. For an antenna with a truncated substrate, the surface waves are radiated at the edges of the substrate and influence the radiation characteristic depending on the ratio of the edge length l of the patch to the length of the substrate l_s . This ratio is referred to as p ($p = l_s/l$) in the following. The ratio is evaluated in [57] with its influence on the directivity of a rectangular patch. These investigations showed significant variations of the peak directivity. Due to the fact that the specific configuration of the antenna influences this characteristic, the influence of the ratio p on the realised peak gain is evaluated for the reference antenna in Fig. 5.4b.

As can be seen, the realised peak gain changes considerably over p . The curve shows a sinusoidal behaviour. The realised peak gain values vary between $G_{\text{real, peak}} = 2$ dBi and $G_{\text{real, peak}} = 7$ dBi. In case of having a ratio on the rising or falling edge of the curve even slight changes of p can cause considerable changes of the realised peak gain. Thus, for the following evaluations p is set to $p = 3$. At this point, the maximum of the sine, the peak gain values are relatively steady for slight changes of p .

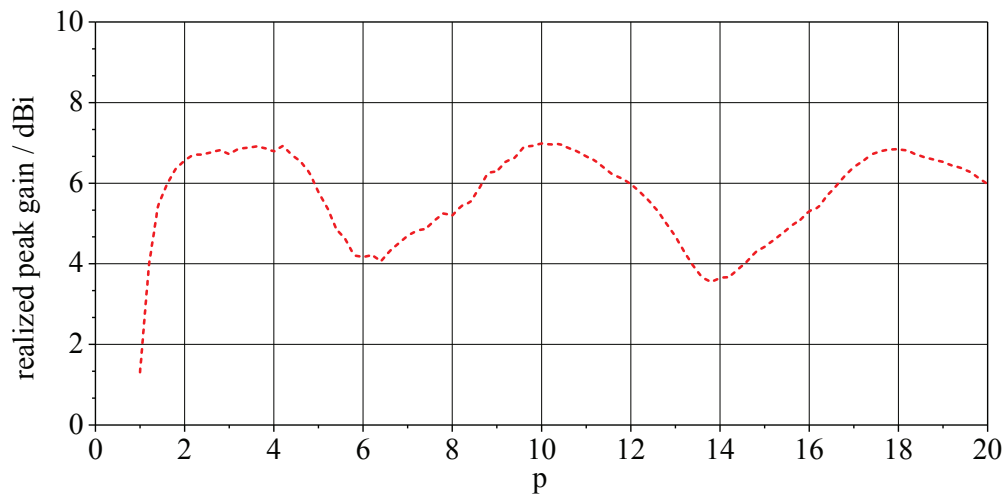


Figure 5.4 Simulated realised peak gain of the reference antenna with varied substrate/ground plane length p

The insights gained for the following investigations of 3D surface shaping of microstrip antennas are:

- Surface waves are excited on microstrip antennas even at low substrate heights
- Provided that the length of the substrate/ground plane of a microstrip antenna is finite, the surface waves excited in the substrate are radiated at the edges of the substrate/ground plane.
- Depending on the ratio of substrate/ground plane to patch edge length, the radiated surface waves can lead to considerable variations in the peak gain achieved. The dependency shows a sinusoidal behaviour. In order to achieve comparable results, the ratio should be kept constant.

5.2 3D Modification of Microstrip Antennas

There are different methods to influence the characteristics of patch antennas concerning radiation, bandwidth or polarization. Frequently, the shape of the patch or the ground plane is modified using specific edge shapes, cut outs, slots or parasitic coupled patches [58]. These modifications are not influencing the planar structure of the antenna. The possibilities gained of 3D fabrication

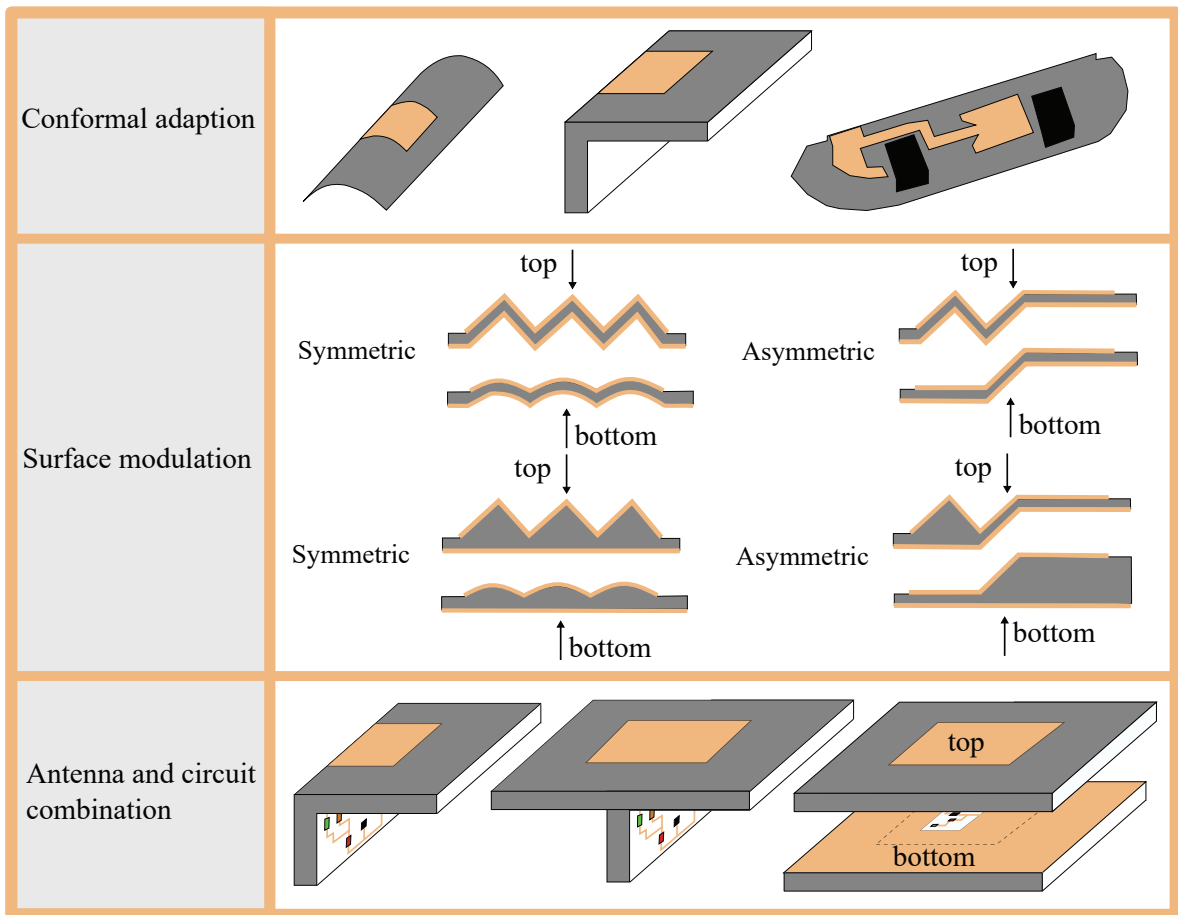


Figure 5.5 Examples for 3D shaping of patch antennas using 3D manufacturing methods

methods allow for a modification of microstrip antennas by shaping the substrate. Fig. 5.5 shows an overview that classifies some types of the possible modifications that can influence the characteristic and geometric dimensions of a patch antenna.

One possible application of 3D shaping is the conformal application of the antenna on or in a given installation space. On the example of an conformal antenna integration on an aircraft this is described in [59]. Another possibility is the use of arbitrarily shaped plastic forms, e.g. a cylinder in [60]. These antennas are only slightly bent and only in one direction. This is due to the specific shape of the installation space on one hand and presumably due to the limitations in the fabrication on the other hand. This configurations are well known as conformal antennas and evaluated in several scientific publications e.g. in [61–64]. This is why these configurations are not further discussed within this work.

By using injection moulding to fabricate the antenna substrate, a more pronounced shape can be achieved. This could for example be a modulation of the substrate in a sinusoidal or triangular shape as discussed in the following Sec. 5.2.1. Such a modulation may include or exclude the ground plane as shown in Fig. 5.5 (middle). A further possibility to use the design scope of 3D manufacturing for microstrip antennas is the combination of the antenna with a circuitry as depicted in Fig. 5.5 (bottom). This aspect is further discussed in Sec. 5.2.2.

5.2.1 3D Surface Modulation

A 3D shaping of a microstrip antenna can be done initiating a modification of the geometric dimensions e.g. to adapt the antenna on an installation space. As an example, the antenna can be formed folding the whole substrate of the antenna including the patch and the ground plane. For this configuration the distance between patch and ground plane remains the same. The position, at which the structure is bend, will influence the antenna differently. As an example, a bend in the inner patch area will have another effect as a bend that only involves the substrate and the ground plane outside the patch area. An example of such a modification with one bend in the inner area of a rectangular patch can be found in [14]. A further example with several bends in the inner patch and outer ground/substrate area can be found in [65].

Another way to modify a patch is to shape the substrate by varying the thickness of the substrate between patch and ground plane. An example was evaluated by Poddar et. al. in [66]. The substrate of a patch is configured wedge-shaped and the influences on the input impedance are shown. Another configuration with varied substrate height can be found in [67]. In this publication a circular patch with a conical recess is discussed focused on a bandwidth enhancement. A further example can be found in [68]. The author discusses a rectangular patch with one to two ridges or grooves added to the substrate. The modification is done transverse to the non-radiating edge and leads to different substrate heights. Filling the space under a modulated surface as it is done in the publications described lead to thick substrates. Depending on the operating frequency such kind of substrates are difficult to be fabricated in a injection moulding process. Therefore, only the 3D shaping of the entire substrate without changing the substrate height is considered in the following.

As evaluated in [14] for a single bend on the non-radiating edges of a rectangular

patch antenna, a bend leads to a disturbance of the field in the slot between patch and ground plane. This causes a shift of the resonance to higher frequencies due to the capacitive effect of the bend. Concerning the radiation characteristic the antenna with one bend has a lower peak gain but radiates more power in the lower half space. This may be explained by the radiating edges that are directed downwards.

In the following the reference patch antenna shown in Fig. 5.3 is shaped with a symmetrical triangular surface modulation as depicted in Fig. 5.5. Since this is a very pronounced modification with sharp bends, this configuration is investigated as one example of a 3D shaping of microstrip antennas. The edges of the substrate/ground plane are positioned in the same plane as for the planar patch. The patch to substrate/ground plane ratio p is set to $p = 3$ for the reference antenna. This results in a edge length of $l_s = 38.4$ mm of the entire antenna. The length l_s is kept the same for all surface modifications. This leads to slight variations of the ratio p which only slightly influences the realised peak gain as evaluated in Sec. 5.1.

Firstly, a modulation that includes the edges of the patch is investigated. In doing so the current path of the patch can be increased using more space in the height. This configuration can e.g. be used for installation spaces in which the space of base area should be reduced. The configuration evaluated is a surface modulation with a triangular shaping as it is depicted in Fig. 5.6a. The shaping is done symmetric to the x- and y-axis. The maximal height of the modulation $h_{\text{mod}} = 5$ mm results in a overall height of $h_{\text{res}} = 6$ mm with a substrate height of $h = 1$ mm. Due to the surface modulation the feed point is slightly adapted for configurations $h_{\text{mod}} = 4$ mm and $h_{\text{mod}} = 5$ mm to achieve an input matching to 50Ω . The feeding position is shifted from $x_{\text{feed}} = 2.3$ mm to $x_{\text{feed}} = 2.1$ mm. Fig. 5.6b shows the input reflection coefficient for the different configurations. As can be seen, all configurations show an input reflection $|S_{11}| \leq -10$ dB at their specific centre frequency. The centre frequency is decreased with increasing height of the modulation h_{mod} . The bandwidth decreases from $BW_{\text{rel}} = 2.1$ % at $f = 5.8$ GHz with $h_{\text{mod}} = 0$ mm down to $BW_{\text{rel}} = 1.54$ % at $f = 3.89$ GHz with $h_{\text{mod}} = 5$ mm.

Fig. 5.6c-d shows the radiation characteristic as partial realised peak gain over frequency and as partial realised gain pattern for $\varphi = 0^\circ$ and $\varphi = 90^\circ$. As can be seen the modulation leads to a slight reduction of the realised peak gain. The realised gain decreases from $G_{\text{real}} = 7$ dBi for reference antenna down to $G_{\text{real}} = 5.2$ dBi for $h_{\text{mod}} = 5$ mm with a centre frequency of $f = 3.89$ GHz. As can be seen the shift of the centre frequency is maximal for the configuration with

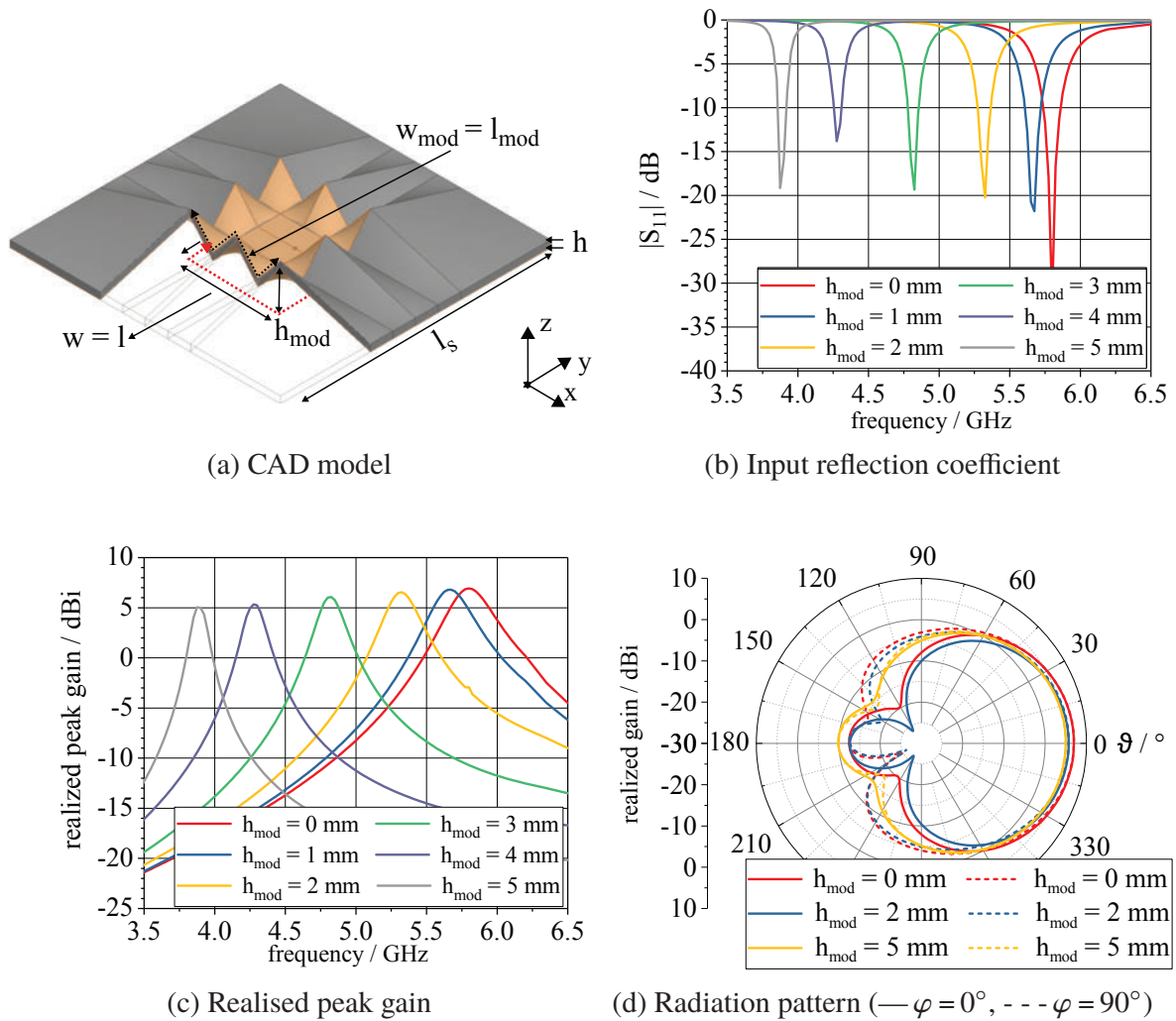


Figure 5.6 Simulated data for triangular modulated edges of patch antenna operating at 5.8 GHz

$h_{\text{mod}} = 5 \text{ mm}$.

The reduction of the realised gain can be explained by the arrangement of the radiating slots using the cavity model as it is e.g. described in [47]. As shown in Fig. 5.7 the electric field and the associated equivalent current densities in the slots of the modulated triangular substrate can be divided into two components, a y-component and z-component. Both z-components are directed in the opposite direction. Consequently, these components cancel each other when superimposing equivalent magnetic currents according to cavity model. This can also be observed when evaluating the radiation efficiency. The reference model has an simulated radiation efficiency of about $\eta = 90 \%$ while for the modulated

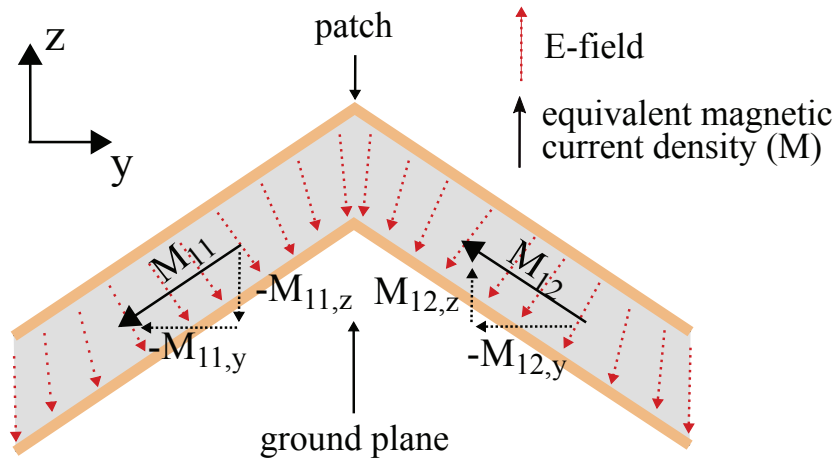


Figure 5.7 Schematic diagram of the E-field and the associated equivalent magnetic current densities in the radiating slot of a patch antenna with triangular modulated substrate according to the cavity model as described in [47]

patch with $h_{\text{mod}} = 5$ mm the radiation efficiency decreases to $\eta = 72$ %.

Next, the size of the modulated patch antenna is reduced until the operating frequency is $f = 5.8$ GHz as for the reference setup. The configuration with $h_{\text{mod}} = 5$ mm and $h_{\text{mod}} = 4$ mm are not considered because the size reduction required to shift the centre frequency back to $f = 5.8$ GHz leads to a shape that intersects with itself. This is why the configuration with $h_{\text{mod}} = 3$ mm is used in the following. The size reduction leads to an edge length of the base area of $w = l = 11.16$ mm and $l_s = 23.88$ mm. The size of the base area is reduced by the factor of 1.3 compared to the reference antenna. The simulated input reflection coefficient and the associated radiation pattern are depicted in Fig. 5.8. The input reflection coefficient is similar to the values obtained for the reference antenna. Compared to the modulated antenna operating at $f = 4.8$ GHz the bandwidth is increased from $BW_{10, \text{dB, rel}} = 1$ % at $f = 4.8$ GHz to $BW_{10, \text{dB, rel}} = 1.5$ % at $f = 5.8$ GHz. This is due to the fact that the effective substrate height h is increased by shifting the centre frequency to $f = 5.8$ GHz. Compared to the reference antenna the relative bandwidth is slightly reduced caused by the 3D surface shaping. The radiation characteristic (Fig. 5.8b) shows that the realised peak gain is still reduced for the 3D shaped configuration in comparison with the reference antenna. This is because of the specific arrangement of the radiating edges due to the 3D shaping of the antenna as described above.

Secondly, a modulation in the inner patch area is investigated. In doing so the edges of the patch are the same as for the reference antenna. The surface

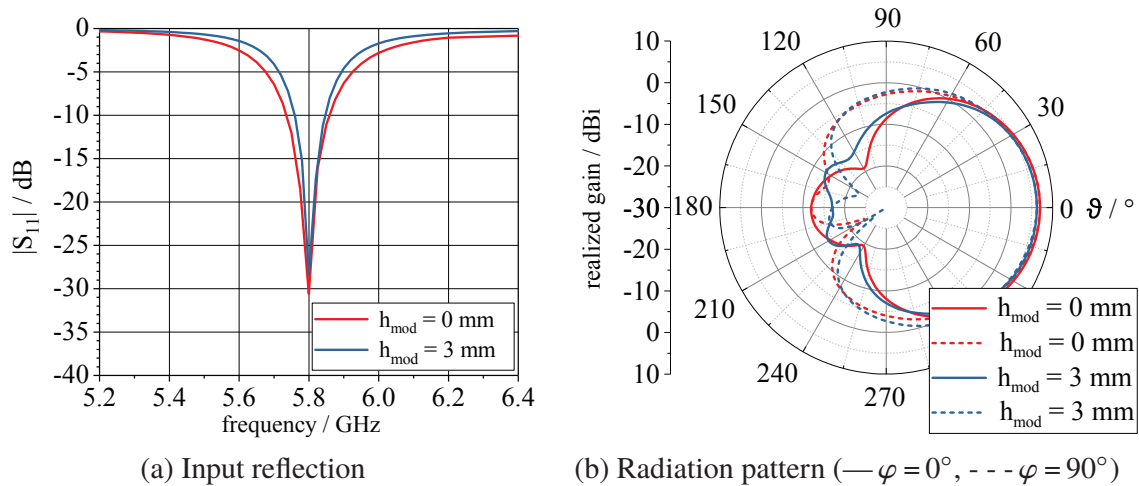


Figure 5.8 Characteristics of a triangular modulated patch with $h_{\text{mod}} = 3$ mm operating at 5.8 GHz (simulated)

modulation used is a triangular shaping as it is depicted in Fig. 5.6a together with the relevant dimensions. The height of the modulation $h_{\text{mod}} = 3$ mm results in an overall height of $h_{\text{res}} = 4$ mm with a substrate height of $h = 1$ mm. Fig. 5.9b shows the input reflection coefficient for the configuration compared to the reference setup. As can be seen, the centre frequency is decreased down to $f = 5.2$ GHz. In addition, two modes are excited whose resonance frequencies are shifted close together as can be seen from the two minima in the input reflection coefficient. Considering, the fact that the patch is quadratic and the modulation is done symmetrically this indicates that a second, orthogonal mode is excited on the patch. At $f = 5.2$ GHz both modes occur close together causing a low input reflection coefficient. This indicates that this configuration provides a circular polarisation instead of a linear polarisation. This is verified by the axial ratio plotted in Fig. 5.9 e. The axial ratio is below 3 dB at $f = 5.2$ GHz. This example shows a further aspect to use a 3D surface modification for microstrip antenna design.

In addition to the surface modulation discussed above, a modification of the shape of the patch can be done. This could for example be the usage of slots as it is done for the prototype design that is described in the following.

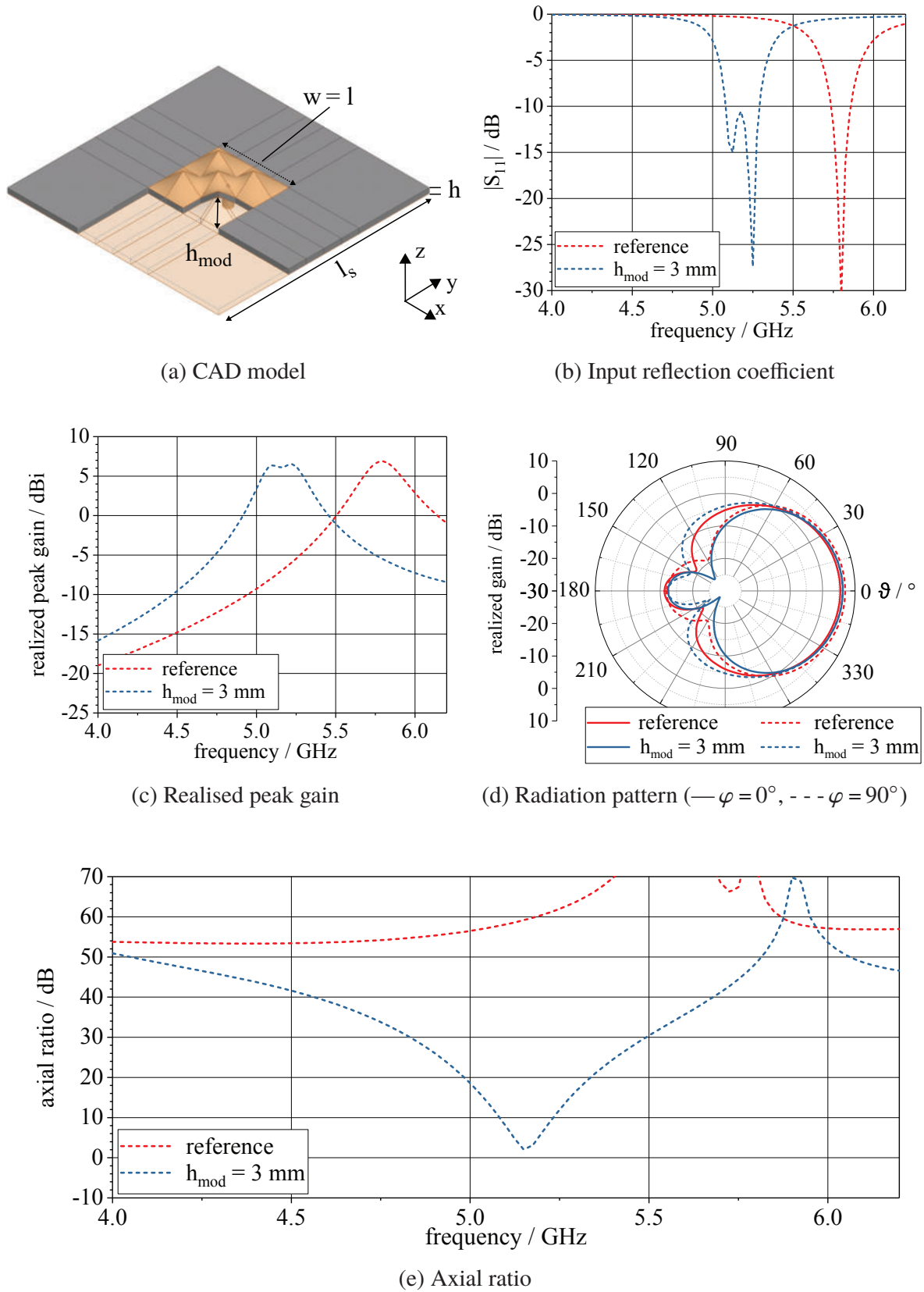


Figure 5.9 Simulated data for a patch antenna with a triangular modulation in the inner area of the patch

The main findings on the 3D surface modulation of square patch antennas operated in the fundamental mode discussed in this section are:

- Provided that the modulation height (h_{mod}) is kept in limits, the modulation of a patch antenna including the ground plane does not change the RF characteristics of a patch antenna in principle.
- The surface modulation of a patch antenna reduces the resonance frequency of the antenna and allows for a reduction of the base area of the antenna. This method leads to a reduction of the realised gain.
- The modulation of the inner surface of the patch allows to influence the mode excited on a quadratic patch. This allows for an excitation of the two fundamental orthogonal modes e.g. to induce a circular polarisation.

5.2.2 Combined 3D Microstrip Antenna and Circuitry

Another aspect of using 3D manufacturing methods is the integration of a circuit such as an LNA and a microstrip antenna on a single plastic part. To assemble a circuit, a suitable area for installation must be provided. This can for example be directly under the patch by cutting out the ground metallisation. A cut out under a patch antenna is known as microstrip antennas with defected ground structure (DGS) and frequently discussed in literature. In these cases the DGS is used to optimise the antenna as it is e.g. done in [69]. In this article L-shaped slots are cut in the ground plane positioned under the edges of a quadratic patch. The investigations aimed for a circular polarization of the linearly polarized quadratic patch. In [70] a configuration of a patch with two slots in the ground plane is investigated. The slots are not positioned under the patch but parallel to both sides close to the resonating edges. These evaluations showed a minor influence on the input reflection coefficient and the radiation characteristic. Both investigations show that slots in the ground plane can have a minor as well as a major influence on the antenna characteristics. When integrating a circuit it is not intended to influence the characteristics of the antenna, therefore the slots must be inserted in a suitable position and with a suitable size.

The surface currents on the reference patch antenna and the associated ground plane are shown in Fig. 5.11a. As can be seen, the currents are directed along the non-radiating edges and have a phase difference of 180° between patch

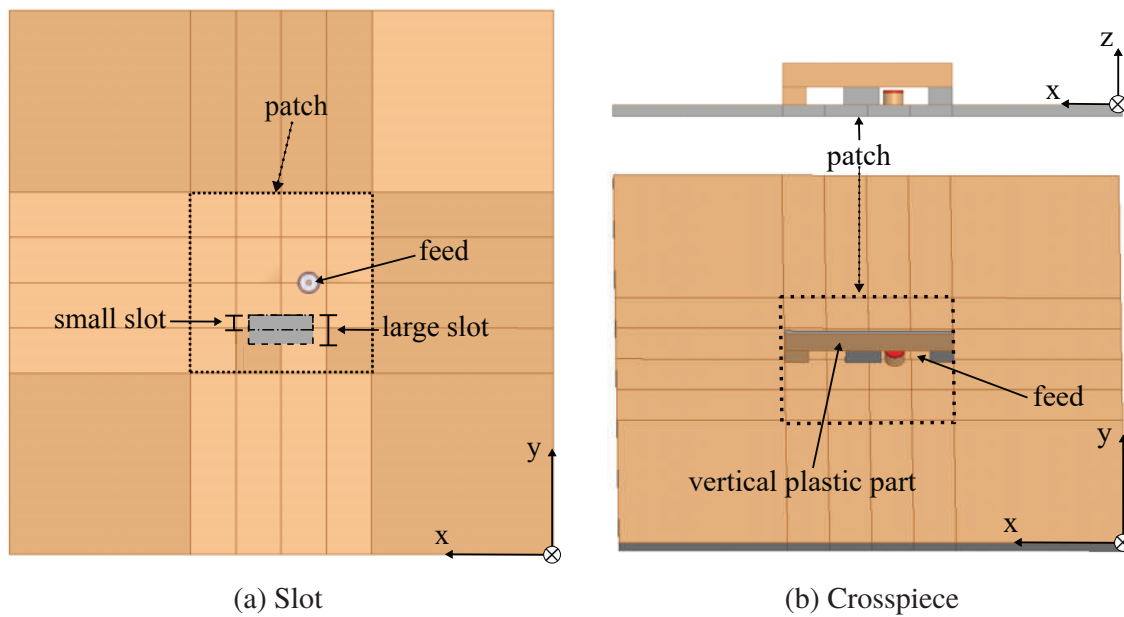


Figure 5.10 Bottom view of a quadratic patch with different gaps in the ground plane

(top-view) and ground plane (bottom-view). When inserting a slot in the ground plane, an integration aligned with the surface currents seems to be an appropriate way to reduce the distortion of the surface currents. Two configurations, as shown in Fig. 5.10a are evaluated in the following. The reference antenna is configured with a slot with a length of $l_{\text{slot}} = 5 \text{ mm}$ and a width of $w_{\text{slot}} = 2 \text{ mm}$ and $w_{\text{slot}} = 1 \text{ mm}$. All investigations are done on the basis of EM field simulations.

Fig. 5.11b-c shows the surface current density for both configurations with slot in the ground plane. As can be seen, the surface current distribution is not influenced basically. There is still the phase difference between patch and ground plane with the surface currents aligned to the non-radiating edges. In the area with the slot there can be seen that the currents are concentrated around the slot. This causes a high current density on the edges of the slot and induces a lengthening of the current path of the currents flowing on the ground plane. Considering the fact that the ground plane of the reference patch is finite ($l_s = 38.8 \text{ mm}$) this will have an influence on the interference of the overall currents on patch and ground plane. This in turn may influence the radiation characteristic and the resonance frequency. For the configuration with the small slot $w_{\text{slot}} = 1 \text{ mm}$ (Fig. 5.11b) the distortion of the surface currents is significantly reduced, compared to the configuration with the large slot (Fig. 5.11c).

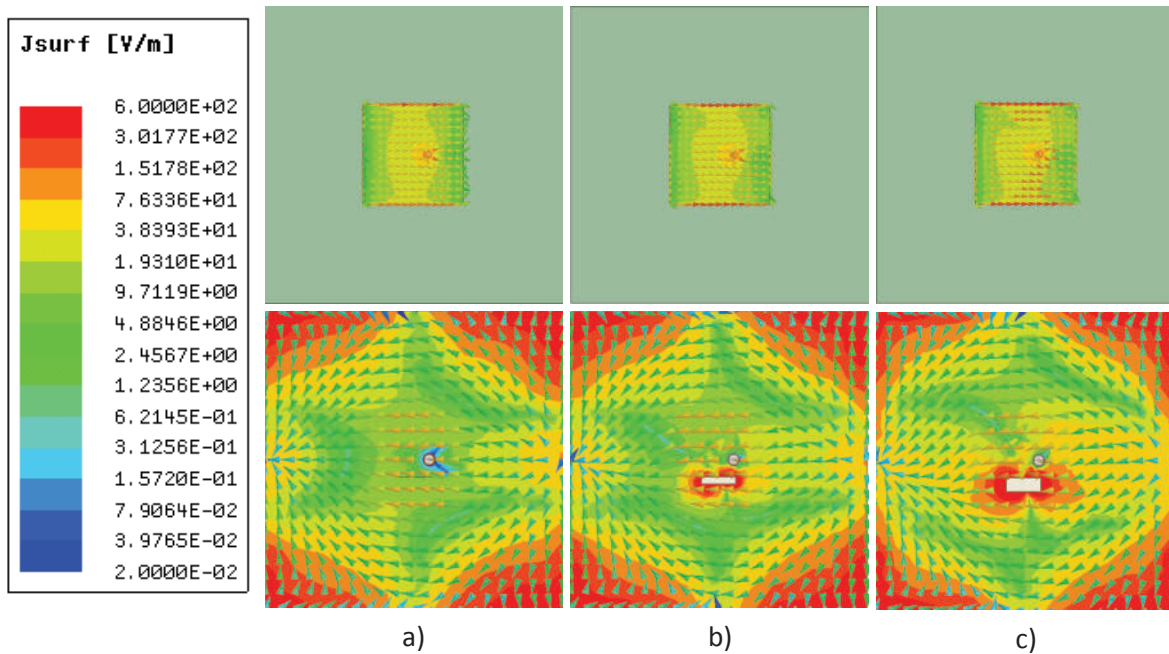


Figure 5.11 Surface currents of the reference patch antenna without slot and with small and large slot in the ground plane, top-view and bottom-view

Fig. 5.12a shows the simulated input reflection coefficients for both configurations. As can be seen the large slot causes a shift of the centre frequency from $f = 5.8$ GHz down to $f = 5.62$ GHz. In case of the small slot the centre frequency is at $f = 5.8$ GHz as expected. The radiation pattern depicted in Fig. 5.12b shows a slight change of the radiation pattern for the configuration with a large slot while for the configuration with the small slot no differences compared to the reference configuration are seen.

Depending on the size of the slot the available space can be used to integrate a circuit directly. It should be borne in mind that, depending on the operating frequency, the space gained by a slot in the ground plane can be very small providing not enough space for circuit integration. Another aspect to consider is that electromagnetic interference can occur that influences the circuit characteristics. A further aspect is the ground reference. In case of using e.g. microstrip lines a ground reference is needed. These points must be carefully considered before this area can be used for circuit integration.

Another possibility is the installation of an additional plastic part to integrate the circuit. With this configuration, the slot in the ground plane under the patch can be much smaller, as only a mechanical attachment must be ensured. Fig. 5.10b shows a configuration with three small slots and a plastic part installed

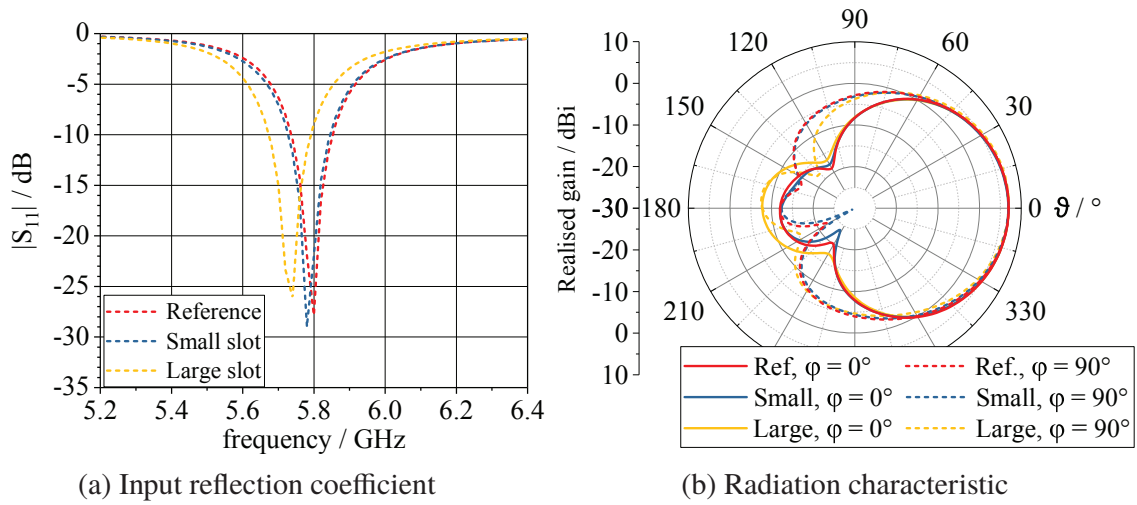


Figure 5.12 Simulated characteristics of quadratic patch with slot in the ground plane

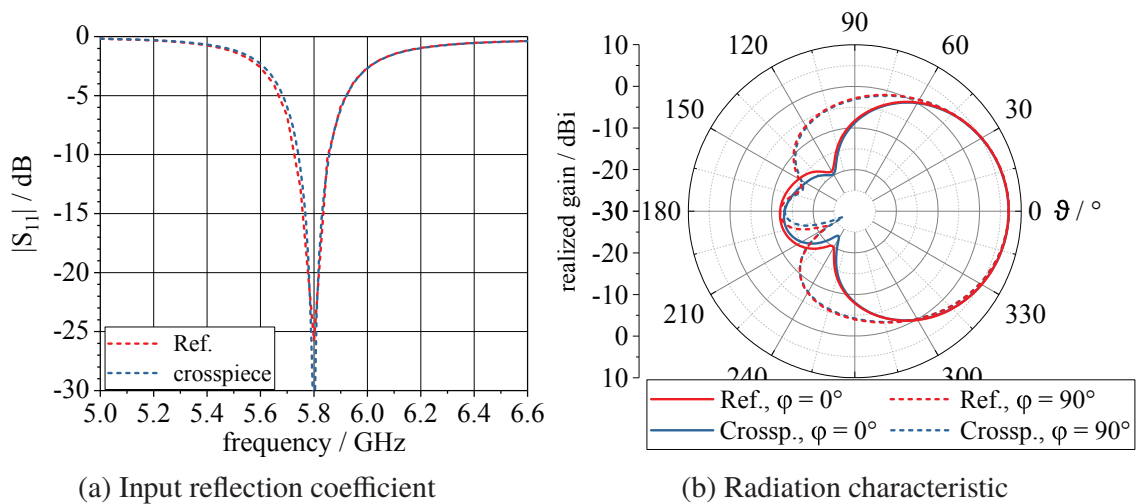


Figure 5.13 Simulated characteristics of quadratic patch with crosspiece installed under the patch

perpendicular to the patch surface. The plastic part is connected to the ground plane of the patch, having one side completely metallised. The area for circuit integration that is gained by installing this crosspiece is $3.5 \text{ mm} \times 14.4 \text{ mm}$ for the reference antenna operating at $f = 5.8 \text{ GHz}$. Fig. 5.13a shows the simulated input reflection coefficient for this configuration compared to the reference antenna. As can be seen, the input reflection coefficient is only slightly influenced by the installation of the crosspiece. The same applies to the radiation characteristic plotted in Fig. 5.13b.

The main findings concerning the circuit integration on microstrip antennas as discussed in the last Section are:

- Slots in the ground plane of a patch antenna can be integrated in such a way, that the antenna characteristics are only slightly influenced.
- Slots in the ground plane of a microstrip antenna may be used to integrate a circuit. It has to be considered that depending on the operating frequency, the slot that can be integrated under the patch without influencing the antenna characteristics may be very small. This may result in insufficient space to install a circuit directly in the area of the slot.
- A further possibility to integrate a circuit under a patch antenna is to install an additional part perpendicular to the ground plane. If such a plastic part is installed appropriately, it has only a minor influence on the antenna characteristics.

5.3 Realisation of 3D Active GPS Antenna

On the basis of the investigations described in the last Section an active patch antenna is designed for civil GPS at $f = 1.575$ GHz using the 3D LDS manufacturing. The LNA circuit is integrated on the same plastic part. The antenna design is described in detail in [AF5] (© IEEE 2015). The developed antenna is targeted to provide an input reflection coefficient $|S_{11}| \leq -10$ dB in a 50Ω system. The polarisation should be right handed circular (RHCP) with an axial ratio (AR) of less than $AR \leq 3$ dB in the upper half space. A square patch antenna with slots is used to achieve circular polarisation. In the first step, the slotted patch antenna is evaluated on a planar substrate and optimised for the target application. In the next step, the patch antenna is applied on a triangular modulated surface as discussed in Sec. 5.2.1 and matched again to $Z = 50 \Omega$. The space under the modulated patch antenna is used to integrate the LNA. In Fig. 5.14a the slotted rectangular patch antenna is shown on the 3D substrate. The feeding is done using a coaxial feed that is positioned on the diagonal axis. Besides the surface modulation directly underneath the patch surface the side parts are folded down and outwards (Fig. 5.14) to obtain additional space to integrate the LNA circuit later on. Optimising the antenna leads to a total height of $h_{\text{total}} = 12.5$ mm and a length of the entire configuration of $l_{\text{sub}} = 64$ mm. The

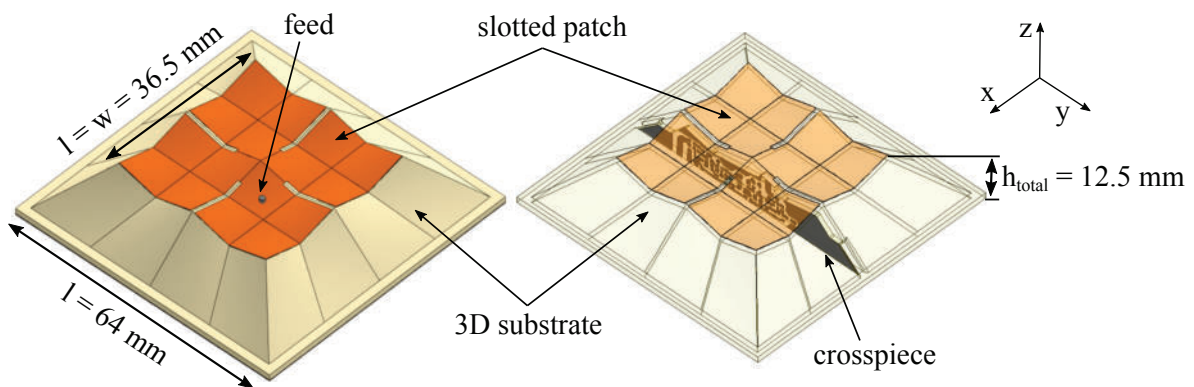


Figure 5.14 Slotted and 3D modulated patch antenna [AF5] (© IEEE 2015)

length of the modulated patch is $w = l = 36.5$ mm and the height due to patch modulation is $h_{\text{mod}} = 3$ mm. The space under the antenna is used to install a small crosspiece on which the circuit elements for the LNA are placed on. The crosspiece is fixed at three points only, to assure not to influence the antennas characteristics as discussed in Sec. 5.2.2. The fixing point in the middle of the crosspiece is used to route the feed line from the antenna to the input of the LNA circuit as depicted in Fig. 5.16.

The antenna is fabricated using a 3D SLA part which is metallised with LPKF ProtoPaint LDS. The relative permittivity of the SLA epoxy resin (SL(EP)9000 Der SL Profi) is $\epsilon'_r = 3.4$ and the loss tangent $\tan \delta = 0.018$, both measured at $f = 1$ GHz with the admittance measurement method. Since the relative permittivity of this material is lower than for materials typically used for GPS patch antennas, it is obvious that the dimensions of the antenna will increase. Furthermore, the realised gain may be reduced due to the relatively high dielectric losses. However, this can be accepted for a prototyping application. As already described in Sec. 2.4, there are LDS materials available providing comparable low losses as materials typically used for RF applications. The changes in the relative dielectric constant due to the LDS ProtoPaint coating of the epoxy resin are taken into account by reducing the dielectric constant to $\epsilon_r = 3.29$ for the EM simulations. The 3D design shown in Fig. 5.14 allows to integrate a circuit very close to the feeding point of the antenna. For an active antenna the integration of the LNA close to the feeding point is of particular importance to reduce the system noise figure. A further advantage of the proposed antenna design is that the ground plane of the patch antenna shields the circuit against electromagnetic interferences. This is especially important considering the low signal strength in GPS applications.

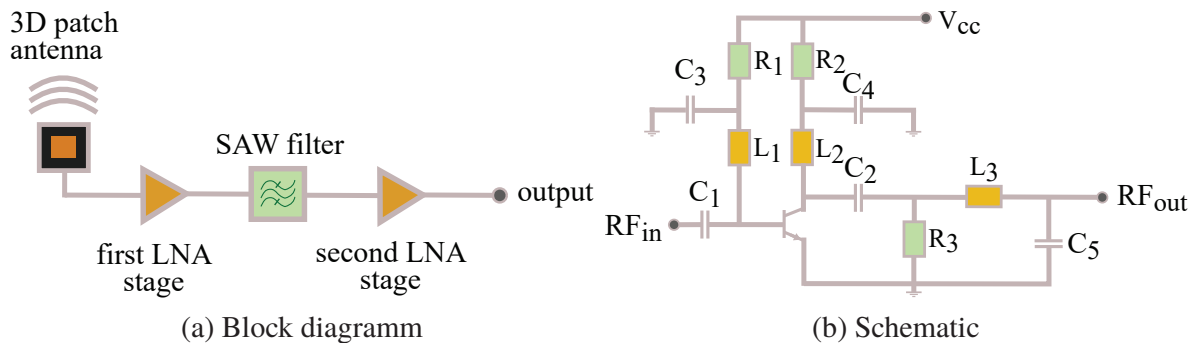


Figure 5.15 Two stage low noise amplifier for 3D GPS antenna [AF5] (© IEEE 2015)

For the design of the LNA a two-stage approach is used. As the first part of a RF system influences the noise figure of the overall system the most, the first amplifier stage is designed minimising the noise figure. After this first stage a surface acoustic wave (SAW) filter (EPCOS SAW RF filter B3522) follows. The second amplifier stage does not have to be as low-noise as the first stage. Thus, other aspects could be considered as design goal depending on the specific application.

Fig. 5.15a shows the block diagram of the amplifier design. The supply voltage is set to be provided as $V_S = 3.3$ V phantom powering. For the layout of the LNA circuit the integration space is considered. This means in detail that the layout of the circuit fits on the crosspiece and must be realisable with the LDS ProtoPaint method. The crosspiece is metallised and connected to the ground plane of the patch on the rear. Thus, the patch antenna and the LNA circuit have the same ground reference. As mentioned before, the design goal for the first LNA stage is minimising the noise figure. Furthermore, a small bandwidth should ensure the rejection of unwanted signals e.g. in the cell phone communication frequency range. With regard to these specifications the amplifier design is done using noise matching instead of impedance matching.

Fig. 5.15b shows the schematic of the LNA for the first stage. It is a class A amplifier based on the transistor BFP640FESD from Infineon and a reference design of the manufacturer. The operating point that is set via the resistors R_1 and R_2 is optimised for a minimum noise figure. To ensure a biasing independent from the RF circuit, two coupling capacitors (C_1 , C_2) are integrated, disconnecting the DC voltage from the rest of the circuit. These capacitors are additionally used to reduce the complexity of the matching network in the next step. Input noise matching is realised with C_1 and an inductive element

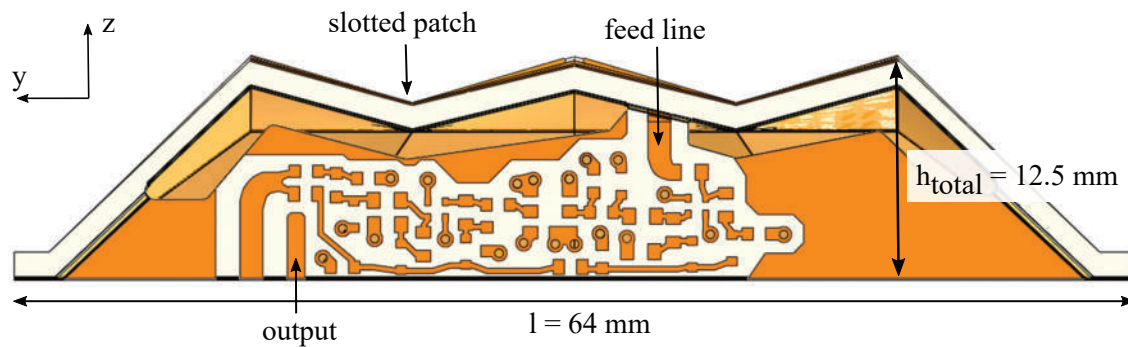


Figure 5.16 LNA circuit layout on the crosspiece of active 3D GPS patch antenna [AF5] (© IEEE 2015)

L_1 connected to ground with a large capacitor C_3 . The capacitor C_3 represents a short for RF signals and prevents the noise matching from being influenced by the biasing resistors. The DC supply is provided via L_1 . To achieve a better frequency selectivity the transistor is loaded with a series resonant circuit that is connected to the collector of the transistor (L_2, C_4). Close to the resonance of the LC circuit there is a short to ground reducing the amplification. With this technique the frequency selectivity is achieved. To ensure the stability an additional resistor R_3 is connected in series with the coupling capacitor C_2 , parallel to the output. These elements reduce the amplification for lower frequencies. Next, the output is matched for power transmission. Therefore an LC series circuit is used, operating as a further low-pass filter (C_5, L_3). Finally, the patch antenna is optimised with the circuit layout on the crosspiece as depicted in Fig. 5.16

Fig. 5.17 shows the realised prototype antenna as unassembled LDS part and assembled. The prototype is realised with a high resolution SLA process. The through holes required for the LNA in the crosspiece are realised directly during the SLA process. Afterwards the through holes are filled with copper wires. Subsequently, the SLA part is covered with LDS ProtoPaint and processed in standard LDS process. For antenna characterisation the antenna is connected directly at the feeding point with an soldered SMA connector and the LNA circuit disconnected.

The simulated and measured antenna characteristics are depicted in Fig. 5.18. In the operating frequency range an input reflection coefficient $|S_{11}| \leq -10$ dB is obtained. The centre frequency measured and simulated differs about $\Delta f = 25$ MHz. This may be caused by differences in the permittivity of the varnished epoxy resin. The evaluation of the radiation characteristic is done at



Figure 5.17 Realised active 3D GPS antenna [AF5] (© IEEE 2015)

the respective centre frequency. An axial ratio of $AR = 1.5$ dB is obtained. The maximum value of the axial ratio is less than $AR \leq 8$ dB for the upper half space. The maximum realised antenna gain is about $G_{real} = -2.5$ dBi at the zenith. The low realised gain is caused by the high losses in the epoxy resin.

For an evaluation of the LNA integrated on the crosspiece an SMA connector is installed on the output and directly at the feed line on the crosspiece. The feed line is disconnected from the antenna and matched to 50 Ohm. This allows an characterisation of the LNA independent of the antenna. The associated impedance levels are considered in the circuit simulation. All simulations shown in the following are performed with Keysight Advanced Design System (ADS), version 2013.06. The simulated values for this first stage LNA indicate a noise figure of $F_{Noise} = 0.76$ dB and a gain of $G_{LNA} = 17$ dB. After the first LNA stage a commercial SAW filter for GPS applications follows. It improves the selectivity of the LNA. In case of the prototype GPS antenna discussed here the second LNA stage is the same as the first LNA stage.

Fig. 5.19 shows the simulated and measured transmission coefficient of the

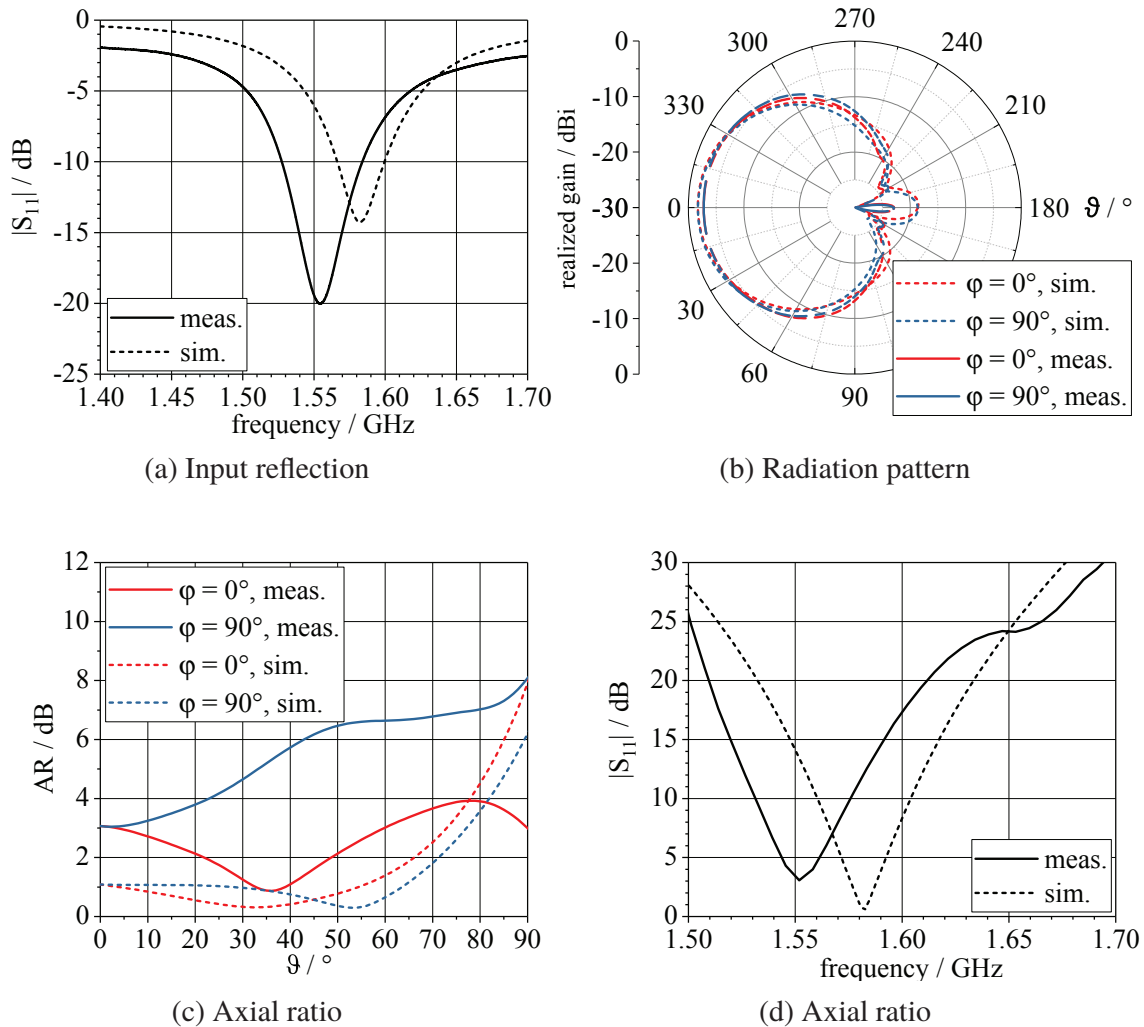


Figure 5.18 Simulated and measured characteristics of the realised 3D GPS antenna [AF5] (© IEEE 2015)

LNA. The results show a good agreement, especially when considering the complexity of the structure. The gain achieved in the target frequency range is about $G_{\text{LNA}} = 29$ dB in the measurement and $G_{\text{LNA}} = 32$ dB for the simulation. The out-of-band rejection in the upper frequency range is about 20 dB below the simulated results. This and the slight differences in the amplification may be due to tolerances of the circuit elements and the manufacturing process.

In conclusion, the prototypical realisation showed that using 3D fabrication methods allows for a flexible modification of the typically planar microstrip antennas. Furthermore, a circuit can be integrated directly under the antenna. The good agreement between measured and simulated characteristics of the

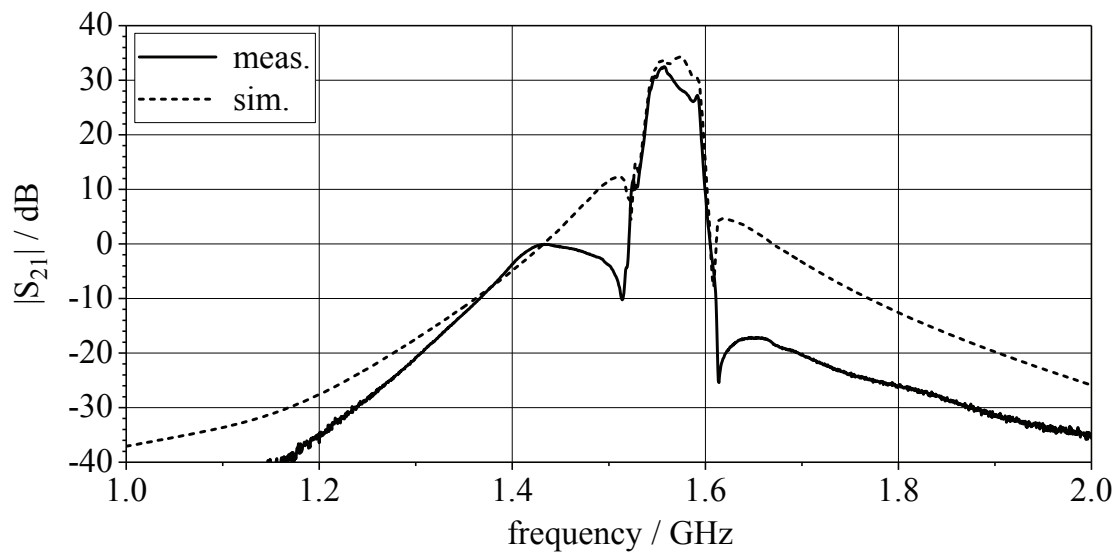


Figure 5.19 Simulated and measured magnitude of the transmission coefficient of the LNA circuit installed on the crosspiece of the 3D GPS antenna [AF5] (© IEEE 2015)

prototype antenna indicates the suitability of the design approach and the reliability of the manufacturing process, especially considering the complexity of the overall structure.

3D Fabrication for Waveguide Fed Antennas

The following Chapter discusses dielectric or dielectric-filled horn antennas as a further application area for 3D LDS fabrication. First, a basic concept for the integration of these antennas into a plastic part is discussed in Sec. 6.1. Different feeding concepts including the transition from transmission lines to a rectangular dielectric filled waveguides are investigated in Sec. 6.2. Subsequently, two prototype antennas are designed and fabricated with LDS method operating at $f = 24$ GHz and at $f = 61$ GHz ISM band. On the basis of the prototype antenna design, an antenna system that is integrated into a plastic frame operating at $f = 60$ GHz (WiGig according to IEEE-Standard 802.11ad) is developed and characterised on the basis of EM simulations. This Section uses textual material and figures based on the authors publications [AF1] (© IEEE 2017), [AF2] (© IEEE 2016) and [AF4] (© IEEE 2016).

6.1 Concept for LDS Fabricated Waveguide Fed Antennas

In the following Section the usage of the LDS fabrication for antennas that are fed by dielectric filled waveguides are discussed. A waveguide consists of a metallic contour, which can in principle be of any shape. This cross section is typically extended in one direction, the direction the electromagnetic wave should propagate. The cross section can also be varied in the direction of propagation, e.g. to convert a electromagnetic wave guided inside the waveguide [71, 72]. The inner side of the waveguide can be filled with air or a dielectric or magnetic material that is defined by its material constants μ, ϵ, σ . Fulfilling Maxwell equations under the specific boundary conditions, infinite types of electromagnetic field distributions can exist in the metallic cross-section of a waveguide, which propagate in the direction of the extension of the waveguide. These different field distributions are referred to as waveguide modes. Common and technical relevant cross sections are rectangular and

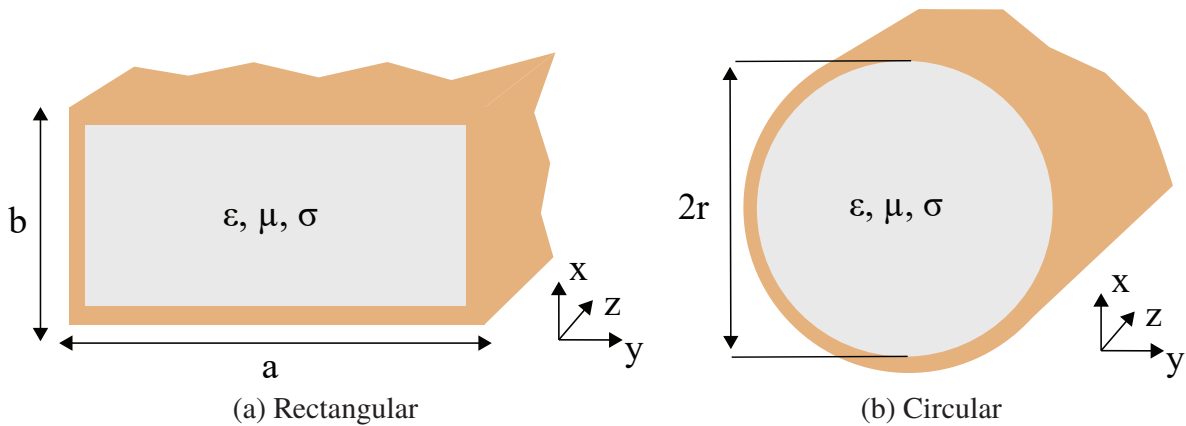


Figure 6.1 Cross section of a waveguide

circular waveguides, as shown in Fig. 6.1. Waveguides are frequently used air-filled, but a dielectric filling is also possible.

The cut-off frequency describes the frequency from which a certain mode can propagate in the waveguide. According to [19] it is defined for the different modes of a rectangular waveguide to:

$$f_{\text{cut-off}} = \frac{1}{2} \frac{c}{\sqrt{\epsilon_r \mu_r}} \sqrt{\left(\frac{m}{a}\right)^2 + \left(\frac{n}{b}\right)^2} \quad m, n = 0, 1, 2, \dots \quad m \neq n = 0 \quad (6.1)$$

As can be seen, the cut-off frequency depends on the geometric dimensions and is scaled by the square root of the relative permeability and permittivity of the material that fills the metallic cross section. A higher permittivity of this material leads to a lower cut-off frequency or smaller dimensions for a specific cut-off frequency. Above its cut-off frequency, a mode in the waveguide can propagate without being limited in bandwidth in principle.

Besides using a waveguide as transmission line, waveguides are often used to feed antennas. Such antennas are based on a radiating aperture, for instance a tapered metallic horn as described in [73] or a tapered dielectric rod/horn as discussed in [74]. The main principle of these antennas is a feeding waveguide which is excited with a specific mode and radiated by the antenna element. Typical optimisation goals for this type of antennas are the gain of the main lobe, the beam width, the front-to-back ratio or the side lobe rejection. These parameters are influenced by the boundary conditions given by the radiating element and the

feeding waveguide. The radiation characteristic of those antennas can provide high gain with very small beam width as e.g. described in [75] for a dielectric tube antenna. Another possibility is to realise a wider beam width with lower peak gain values as discussed for surface integrated waveguide (SIW) antennas in [76]. To influence the side lobe rejection, a principle frequently used is the corrugation of the inner metal walls of the tapered horn as described in [77]. By influencing the surface impedance of the metal walls due to the corrugation, the propagating mode can be transformed to optimise the radiation characteristic, e.g. side lobe reduction. All waveguide-fed antennas have in common that the radiation characteristic can be influenced by the mode the antenna element is fed with, as well as by the geometric shape and material of the radiating element. The use of 3D fabrication for this type of antenna can increase the design scope. The 3D selective metallisation of a three dimensional substrate could be used to combine or develop new techniques to optimise waveguide-fed antennas. Due to the fact that the 3D substrate is processed in an injection mould only the usage of dielectric filled or dielectric coated waveguides is possible. For applications at higher frequencies with small geometric dimensions a dielectric coating may be not manufacturable. In these cases the waveguide structures need to be filled completely. The filling of the waveguide with a dielectric material causes dielectric losses. Using materials that have a low dielectric loss tangent will help to reduce these losses.

Besides the induced losses, the dielectric filling leads to a reduction of the cut-off frequency, as derived from Equ. 6.1. This in turn reduces the geometric dimension of the waveguide at a fixed operating frequency. For all following investigations Xantar LDS 3730 (PC) is used as substrate material. The relative permittivity is $\epsilon_r' = 2.9$ and the loss tangent $\tan \delta = 0.005$ both at $f = 24$ GHz. An RF system often consists of an antenna and a circuitry, e.g. for data processing. With 3D manufacturing, both can be combined, as already described in the last Chapter for microstrip antennas. For this purpose, the transmission line coming from the circuit must be matched to the waveguide feeding the antenna. Such a configuration can be divided into 3 parts as depicted in Fig. 6.2 for some example configurations which illustrate the concept in principle.

An LDS capable plastic part is typically fabricated in an injection moulding process. Thus, the shape of the dielectric antenna is limited only by the respective design rules. This allows to realise plastic parts with surface modifications like corrugations, for example. Additionally, the selective metallisation of these dielectric surfaces can be used to influence the antenna characteristic by realising surface impedances, for example. The concept of LDS fabricated waveguide

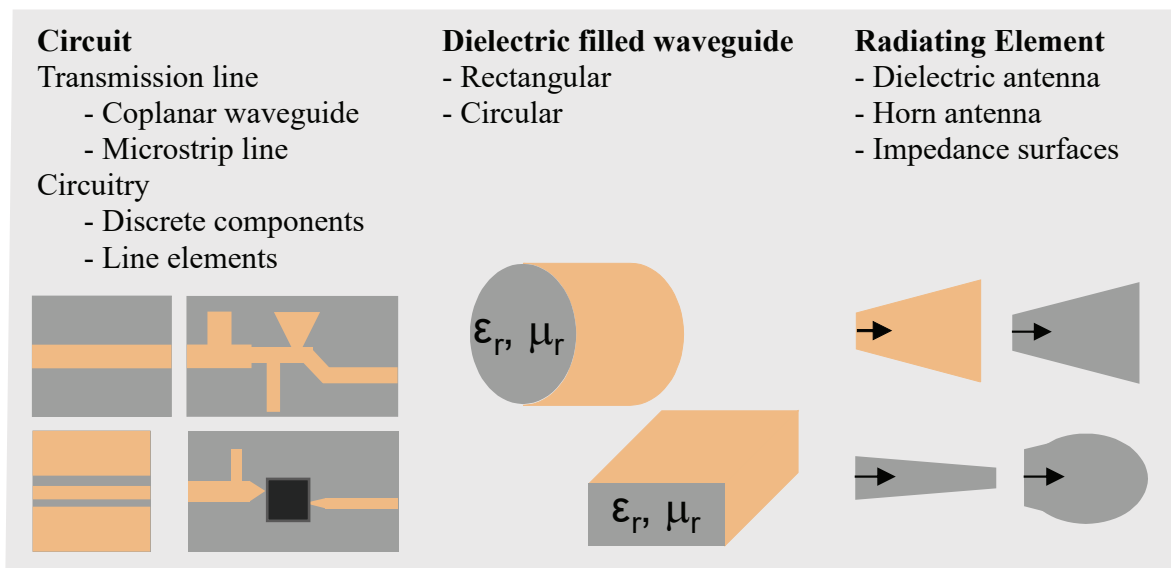


Figure 6.2 Schematic diagram of possible waveguide fed antenna configurations using LDS fabrication [AF1] (© IEEE 2017)

fed antennas is further evaluated and discussed in the following sections on the example of a dielectric horn antenna.

6.2 Feeding Concepts

Especially in applications with operating frequencies in the millimetre wave range, the interconnection between antenna and RF circuit must be carefully designed to reduce the induced losses. Among other things, the losses can be influenced by the length of the transmission line. At millimetre wave frequencies with short wavelengths, which are further reduced by dielectric filling, the transmission lines should be kept as short as possible. Integrating a RF circuit and the antenna on a single LDS fabricated plastic part allows to keep the interconnecting transmission lines as short as possible. The processing RF systems are often fabricated as integrated circuits (IC). In this applications the type of the package and the specific inner interconnects determines the type of transmission line that can be used to connect the IC with the circuit board. For RF circuits based on discrete elements, all types of transmission lines may be used in principle.

As a first aspect, transmission lines can be divided into balanced and unbalanced. Another aspect is the type of transmission line. Typical configurations with

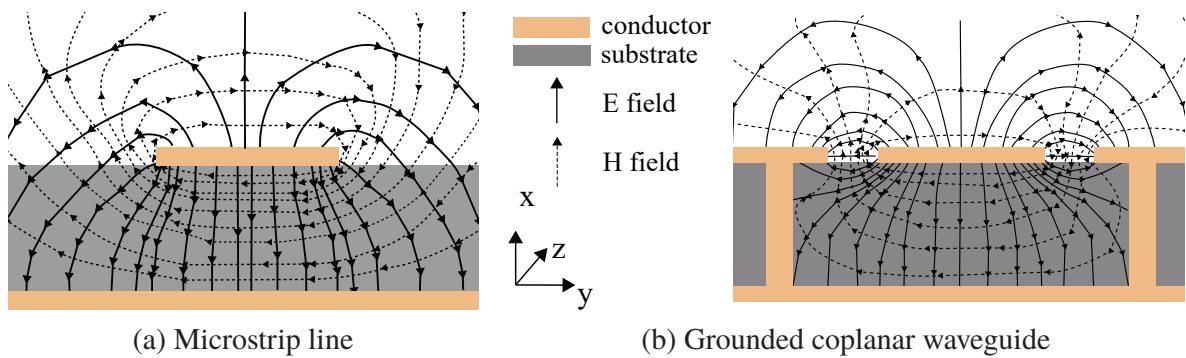


Figure 6.3 RF transmission lines with field distribution of the fundamental mode (schematic)

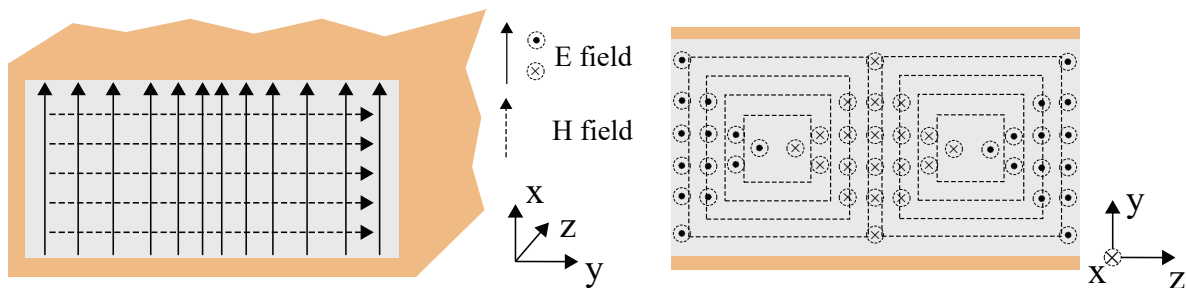


Figure 6.4 Field distribution of fundamental H_{10} Mode in rectangular waveguide (schematic)

a high practical relevance are microstrip lines (MSL), coplanar or grounded coplanar waveguides (CPW or G-CPW). Each transmission line can be designed with different characteristic impedances by varying the geometric cross-section. For balanced transmission lines $Z = 100 \Omega$ and for unbalanced transmission lines $Z = 50 \Omega$ are frequently used. However, deviating values are also possible. As described for the waveguide modes in the last Section, these transmission lines can guide different modes, resulting in a specific field distribution that solves Maxwell's equations under the given boundary conditions.

Fig. 6.3 shows the cross section of a MSL and a G-CPW with the electric and magnetic field distribution for the fundamental mode. To realise a transition from these transmission lines to the rectangular waveguide the mode on the transmission line has to be transformed into the waveguide mode or vice versa. Fig. 6.4 shows the electric and magnetic field distribution of the fundamental mode H_{10} in a rectangular waveguide. As can be seen, the fundamental mode is a TE-Mode with a magnetic field component in the direction of propagation. The associated E-field has only one component which is directed in the x-direction with sinusoidal y-dependence. Considering the field distributions in

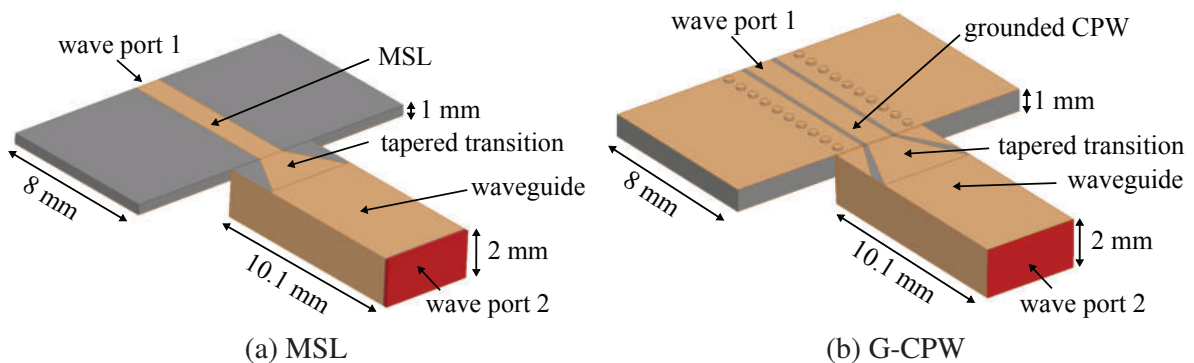


Figure 6.5 CAD model for the transition from planar transmission lines to rectangular waveguide [AF2] (© IEEE 2016)

Fig. 6.3 a and Fig. 6.4 the field distribution of the balanced microstrip line is quite similar to the H_{10} waveguide mode. This can be observed similarly for the grounded coplanar waveguide mode in Fig. 6.3b. On basis of this qualitative evaluation of the field distributions two transitions for both transmission lines are developed and investigated.

The problem of these transitions is similar to the already know and investigated transitions to surface integrated waveguides, which are discussed in several publications e.g. in [78] for a MSL or in [79] for a G-CPW. The difference to SIW structures is that they are realised on a substrate material with constant thickness. For a 3D LDS fabricated transition, the thickness between the two parts may vary. This requires an additional mechanical transition of both parts. The height of the waveguide and the transmission line depends on the operating frequency. Compared to typical SIW structures, the LDS technology can be used to realise waveguides with lower operating frequencies, since the waveguide can also be fabricated with large thicknesses, while for SIW structures typically the limited thickness of the substrate limits the height.

Designing the transition discussed in this work the simplicity of the fabrication process is one objective. Therefore, only LDS metallised surfaces of a solid plastic part are used. In addition, through holes can be used, as these can be realised with the LDS method. The plastic part can be designed arbitrary shaped but considering the design rules of injection moulding and LDS process. For both transmission lines a transition to rectangular waveguide is designed, evaluated and optimised on basis of EM simulations. The waveguide and the transmission line are designed to operate in the 24 GHz ISM-Band. The results can be adapted to other operating frequency ranges by scaling the dimensions.

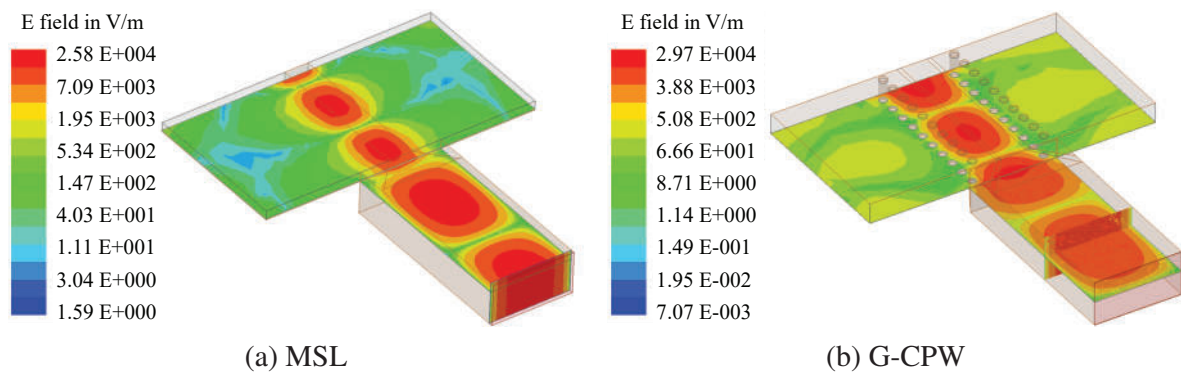


Figure 6.6 Simulated E-field for the different transitions to waveguide [AF2] (© IEEE 2016)

Fig. 6.5 shows the CAD model of the two different transitions as used for the EM simulations. The metallic walls are modelled as sheets with finite conductivity made of LDS copper ($\sigma = 35 \text{ MS/m}$). The structure is fed with wave ports on both sides, the MSL/G-CPW and the rectangular waveguide. To excite the fundamental mode in the rectangular waveguide the inner conductor of the transmission line is tapered and connected to the outer waveguide wall. The ground conductor is connected to the walls of the waveguide, respectively. Varying the width, the gap width and the length of the taper the input reflection coefficient can be influenced. For the mechanical transition, the plastic part of the transmission line can be tapered from the substrate height ($h_{\text{sub}} = 1 \text{ mm}$) to the waveguide height ($h_{\text{wg}} = 2 \text{ mm}$) or this can be done in one step. This applies to the width of the waveguide. In some cases it may be necessary to taper this part for mechanical or electromagnetic reasons. In case of the MSL and G-CPW discussed here, there is no tapering used and the mechanical transition is done in one step.

As can be seen from the magnitude of the electrical field distribution for both configurations in Fig. 6.6, the fundamental mode in the rectangular waveguide is excited. Fig. 6.7 shows the transmission and input reflection coefficient of both configurations from $f = 23 \text{ GHz}$ to $f = 33 \text{ GHz}$. The magnitude of the input reflection coefficient is $|S_{xx}| \leq -12.5 \text{ dB}$ over the whole frequency range. The magnitude of the transmission coefficient decreases from $|S_{xy}| = -1.1 \text{ dB}$ at $f = 23 \text{ GHz}$ down to $|S_{xy}| = 2 \text{ dB}$ at $f = 33 \text{ GHz}$. As already mentioned these transitions can be scaled for other frequency ranges. This is done for the prototype antenna realised and described in Sec. 6.3 for operating frequencies above $f = 60 \text{ GHz}$.

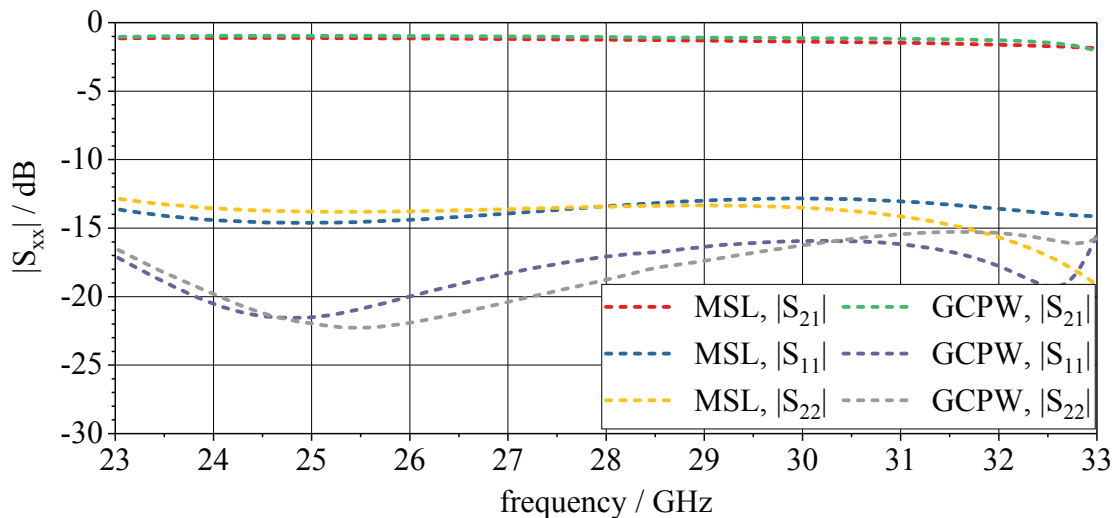


Figure 6.7 Simulated input reflection and transmission coefficient of the different transitions to rectangular waveguide [AF2] (© IEEE 2016)

The main finding obtained in this Section is:

- A transition from an MSL and G-CPW to a rectangular waveguide can be realised with only one single plastic part by selective surface metallisation and through holes using LDS technology. Such LDS-manufactured transitions can offer suitable RF characteristics to be used in RF applications, including the millimetre wave range.

6.3 Prototypic Realisation

On the basis of the basic antenna- and feeding concept discussed, two prototype antennas are developed and fabricated. The operating frequency range is the $f = 24$ GHz and $f = 61$ GHz ISM band. The developed test antennas are not designed for a specific application. Nevertheless, the operating frequency ranges are specified taking into account possible future applications. Both antennas consist of a transition from G-CPW to rectangular waveguide, which feeds a dielectric horn. The plastic parts are made of an injection-moulded plate with a height of $h = 2$ mm. The outlines are cut out using a milling machine. This leads to a very limited design scope for the prototypes. In case of an injection moulded part the full 3D design scope can be used. These limitations in the design scope

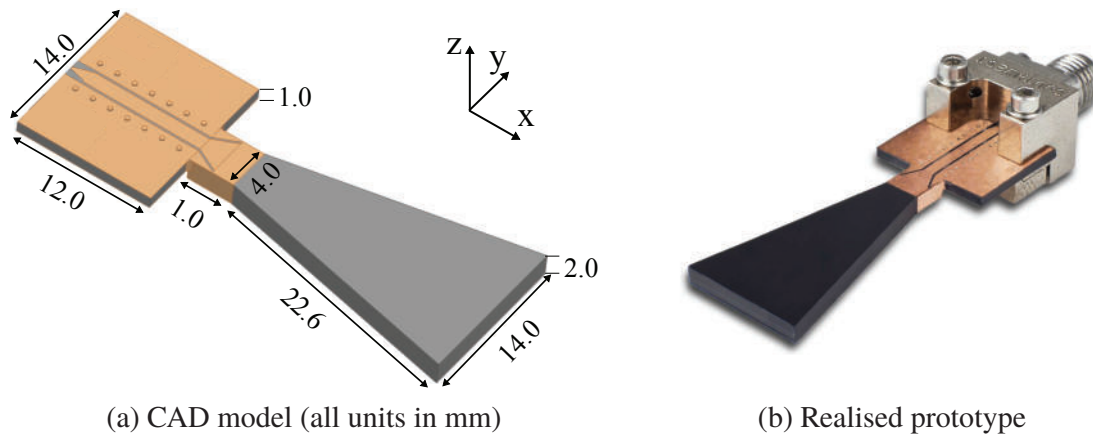


Figure 6.8 Prototype of dielectric horn antenna operating at $f = 24$ GHz [AF2] (© IEEE 2016)

do not restrict the general purpose of the prototypes, the evaluation of the LDS process for a fabrication of waveguide fed antennas in millimetre wave range. The substrate material used is a polycarbonate (MEP Xantar LDS 3730) with a permittivity of $\epsilon_r = 2.9$ and a loss tangent of about $\tan \delta = 0.007$ both measured at $f = 60$ GHz. This LDS capable material offers a good plating ability, high adhesion and mechanical robustness. It is already used for different LDS MID applications in automotive and consumer devices. The metallisation is done with copper ($t \approx 12 \mu\text{m}$). The metallisation is modelled as a sheet with finite conductivity of $\sigma = 35$ MS/m for LDS copper.

Fig. 6.8a shows the CAD model of the prototype antenna design for $f = 24$ GHz (ISM Band). The prototype consists of a G-CPW part that represents the area a circuit can be placed on. The dielectric filled rectangular waveguide is excited with the fundamental mode and feeds a dielectric tapered horn. The horn is tapered in one dimension (sector horn) due to the aforementioned design limitations. The transition of the G-CPW ($h = 1$ mm) to the rectangular waveguide ($h = 2$ mm) is done in one step. Fig. 6.8b shows the fabricated antenna. For characterisation the G-CPW is connected with an end-launch connector. A simplified model of the connector is considered in the EM simulations, as it has a considerable influence on the properties of the antenna. The through holes of the G-CPW are drilled and metallised afterwards.

Fig. 6.9 depicts the simulated and measured magnitude of the input reflection coefficient and the radiation pattern of the realised prototype. The antenna provides an input reflection coefficient $|S_{11}| \leq -10$ dB around the centre frequency $f = 23.8$ GHz. The simulation model was optimised with de-embedded

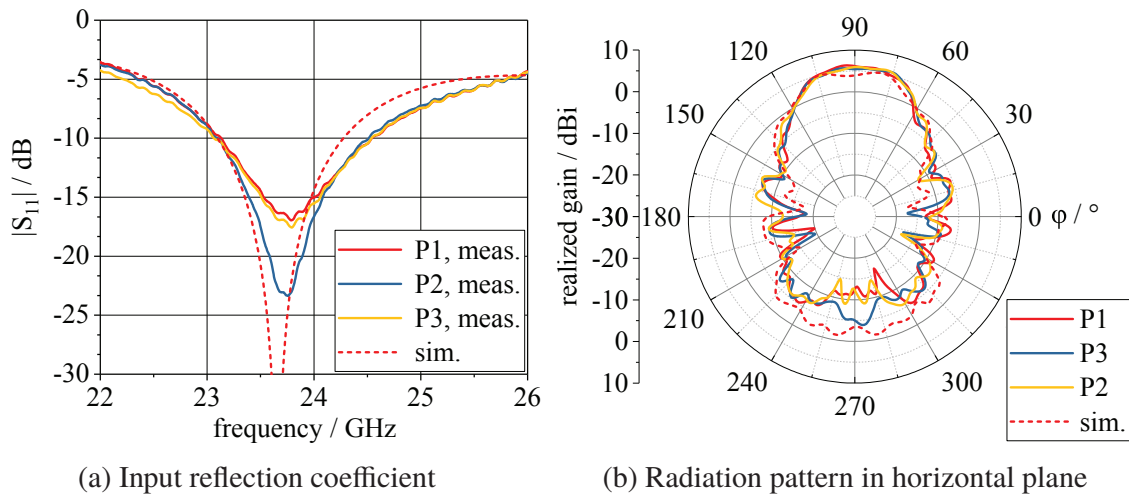


Figure 6.9 Measured and simulated results for prototypic dielectric horn antenna [AF2] (© IEEE 2016)

connector and the connector was only added to compare the results with the measurements. This is why the centre frequency is not at $f = 24$ GHz. There are three prototype antennas measured. The agreement between the simulated and measured data is good, especially considering the assembly of this prototype. The milled and metallised part with the manually positioned through holes is less accurate than a series production with an injection-moulded and laser drilled part would be.

The radiation pattern (Fig. 6.9b) is measured in an anechoic chamber. As can be seen, the radiation characteristic is directive, as expected for this type of antenna. The low front to back ratio is due to the restriction in the design scope and the large end-launch connector, which influences the radiation in the backward direction. The agreement between the simulated and measured data is good. The partial realised gain in the main direction is about $G_{\text{real}} = 6.9$ dBi (measured) and about $G_{\text{real}} = 5.9$ dBi (simulated). For the measured prototypes the gain in the backward direction is reduced. This is due to the fact that the antenna is fixed from the backward direction in the measurement setup.

Next, a prototype antenna is fabricated to operate at $f = 60$ GHz. The fabricated prototype is shown in Fig. 6.10. As for the prototype at $f = 24$ GHz (ISM-Band) the antenna consists of a G-CPW that feeds a dielectric filled rectangular waveguide. The G-CPW substrate and the rectangular waveguide have the same height. The radiating element is a dielectric horn tapered in the xy-plane. The measured and simulated magnitude of the input reflection coefficient is depicted

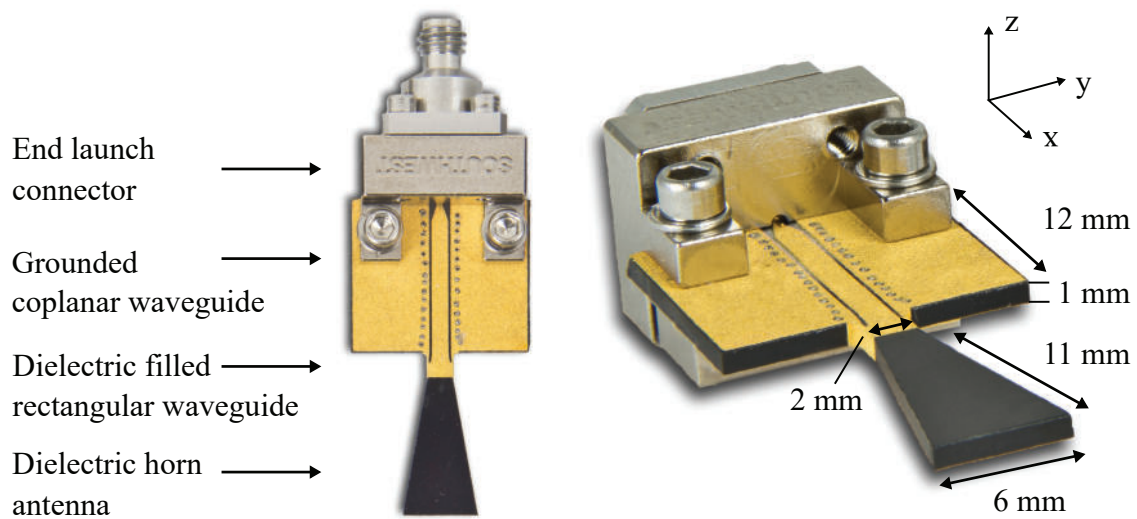


Figure 6.10 LDS fabricated dielectric horn antenna [AF1] (© IEEE 2017)

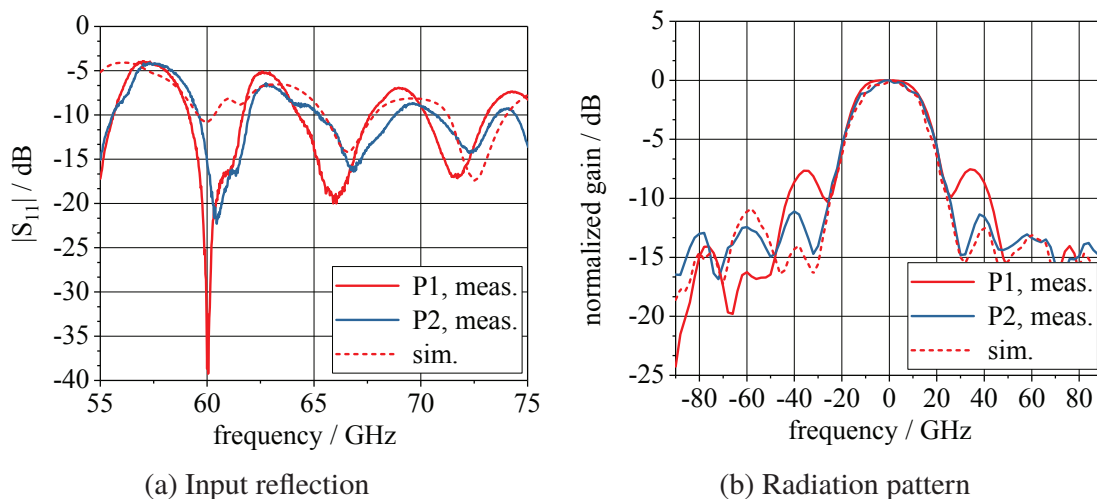


Figure 6.11 Measured and simulated characteristics of the test antenna [AF1] (© IEEE 2017)

in Fig. 6.11a. Two fabricated antennas are measured and the results show an adequate agreement compared to the simulated data. In this concern, it has to be considered that the measurements are carried out with the relatively large end launch connector that influences the antenna characteristic considerably. In the simulations the connector is modelled but only using a simplified model. In the next step the radiation pattern of the antenna is measured at $f = 75.5$ GHz. The normalised radiation pattern in the H-plane is depicted in comparison with

the simulated results in Fig. 6.11b. As can be seen, a good agreement for the main lobe is achieved. The side lobes are in the same angular position, but show slight differences in the magnitude. Comparing the measured results of both test antennas they show a similar behaviour. The measured realised peak gain for the prototype antenna P1 is $G_{\text{real. P1}} = 6.4$ dBi and for antenna P2 $G_{\text{real. P2}} = 6.0$ dBi both at $f = 75.5$ GHz. The simulated results show a peak gain of $G_{\text{real. sim.}} = 7.5$ dBi.

The prototype realisation verifies the suitability of the LDS process for RF devices fabrication at millimetre wave frequencies in principle. Furthermore, it indicates the suitability of the proposed antenna concept. As already indicated in the investigations in Chapter 2, the losses due to metallisation and dielectrics are in a comparable range to typical RF fabrication methods. The prototype concepts discussed in this Section only use a very limited design scope. An integration into plastic parts and an application of a possible circuit pattern are not considered. In the following Section, a generic antenna system is developed and discussed which includes both aspects.

6.4 Plastic Integrated Waveguide Fed Antennas

The results described in the last Section show the suitability of the LDS process for the fabrication of waveguide-fed antennas in the millimetre wave range in principle. For the prototype antennas, the given design scope could not be used due to cost limitations. Considering future RF applications the possibilities gained of LDS manufacturing can be used to integrate waveguide-fed antennas into plastic parts, combining the function of a mechanical part (e.g. housing, plastic cover) as well as an electrical part. This reduces the transitions between antenna, air and other plastic or metal parts in the housing, that cause reflections and thus losses. In case of an integration of the antenna into a plastic part the electromagnetic wave can directly be radiated. It should be noted that this only applies to radiating structures where the main radiation occurs in the areas that are connected to the outer plastic part or housing. In addition to the radiating element, an RF circuit can be integrated on the same plastic part. As an example, Fig. 6.12 shows a schematic sketch of a possible device with an integrated dielectric horn antenna and a transceiver circuitry. The feeding rectangular waveguide can additionally be formed in a slight curve, as is required, for example, to adapt the plastic part to the respective installation space. The mode propagating in the waveguide is not influenced by this as

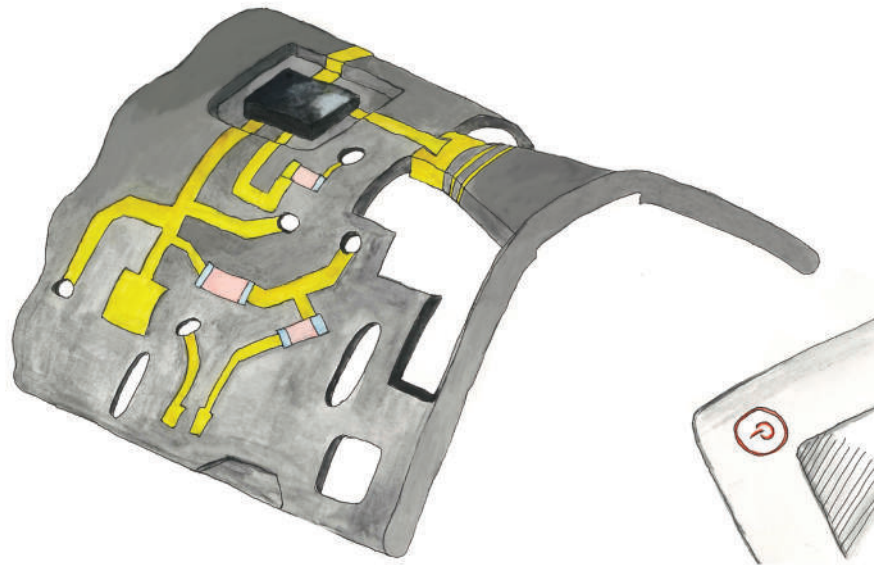


Figure 6.12 Schematic sketch of future smart device with 3D integrated antenna [AF1] (© IEEE 2017)

long as the cross section nearly remains the same. This is already evaluated e.g. in [80] for twists and bends in rectangular waveguides operating in X and S band. To reduce the height of the circuitry parts, like e.g. a packaged transceiver chip, a recess can be designed into the plastic part like it is done in the generic sketch (Fig. 6.12). The metallisation required for RF transmission lines and DC feed circuits is applied on the plastic part, which also forms the frame of a possible plastic housing.

Following, a simplified model of the antenna shown in the schematic in Fig. 6.12 is evaluated on the basis of EM simulations. The antenna development is done for an operation frequency in IEEE WIFI 802.11ad short range data transmission (WiGig). The plastic material is Xantar LDS 3730 as used for the prototype antennas discussed in the last Section ($\epsilon'_r = 2.9$, $\tan \delta = 0.007$ at 60 GHz). The metallisation is modelled as sheets with finite conductivity of LDS copper (35 MS/m). The respective CAD model is shown in Fig. 6.13. The plastic part of the integrated antenna (grey) is covered from the upper and the bottom side with plastic plates (white). Doing so the antenna is completely enclosed in the plastic part. The radiating element is a dielectric horn antenna fed by a rectangular waveguide that in turn is fed by a G-CPW.

The simulated results of the magnitude of the input reflection coefficient are shown in Fig. 6.14. The antenna provides an input reflection coefficient of $|S_{11}| \leq -10$ dB from $f = 57$ GHz up to $f = 64$ GHz and a input reflection

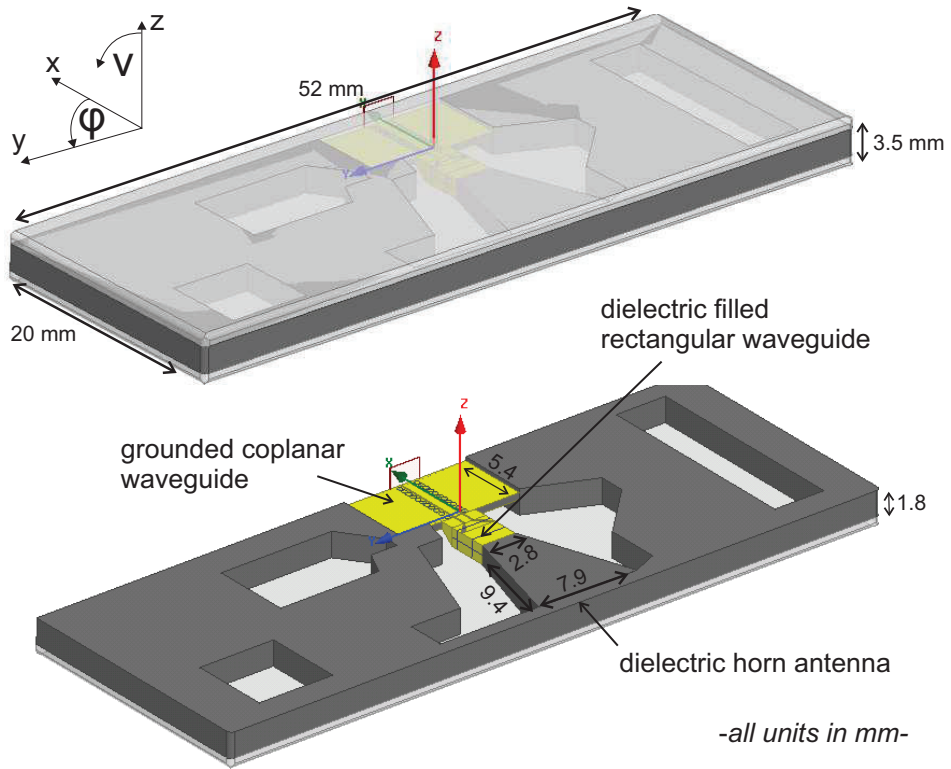


Figure 6.13 Simulation model of integrated smart device antenna [AF1] (© IEEE 2017)

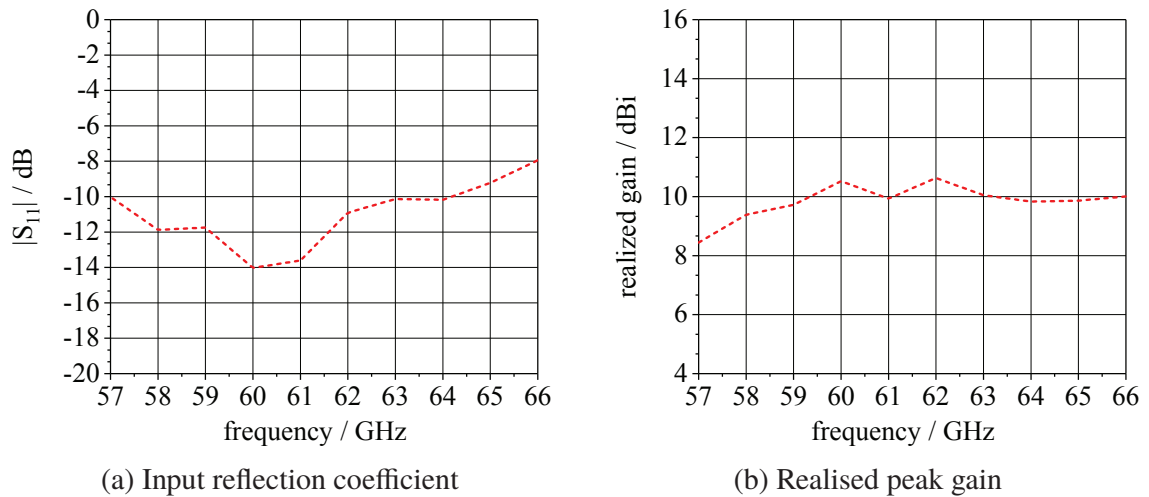


Figure 6.14 Simulated radiation characteristics of the integrated smart device antenna [AF1] (© IEEE 2017)

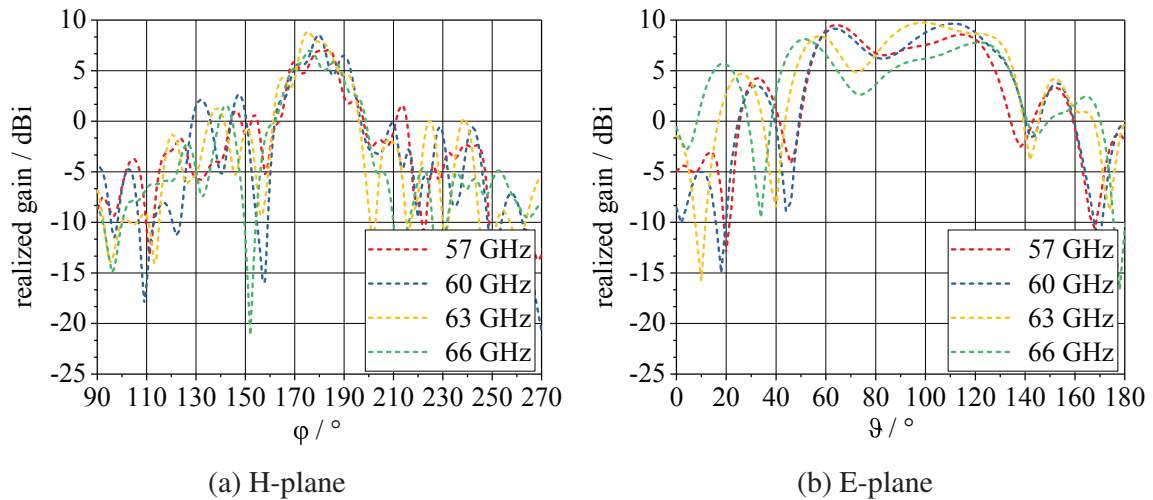


Figure 6.15 Simulated radiation characteristics of the integrated smart device antenna [AF1] (© IEEE 2017)

coefficient below $|S_{11}| \leq -8$ dB from 64 GHz up to 66 GHz. The radiation characteristics in the H- and E-plane is depicted in Fig. 6.15. As expected, the antenna shows a directive pattern. In the H-plane the radiation characteristic has a relatively small main lobe while in the E-plane a wider main lobe occurs due to the planar structure. The realised peak gain in the 60 GHz WiFi/WiGig frequency band is shows a relatively smooth curvature with a maximal variation of about 2.2 dB (Fig. 6.14b).

The results of this test antenna design gives a first insight on the possibilities using 3D manufactured plastic part for an integration of waveguide fed antennas. The designed antenna shows a promising radiation characteristic, especially when considering that the antenna is completely covered with plastic parts. Moreover, the approach using waveguide fed structures provides a broad bandwidth. This is especially interesting for applications in millimetre wave range, which frequently operate with a high bandwidth. Additionally, the sensitivity for slight changes in the fabrication process may be reduced compared to resonant structures like e.g. patch antennas. This may be an important aspect in terms of the fabrication costs.

This thesis contains the investigation of the application of 3D fabrication methods focused on Laser Direct Structuring (LDS) method for antenna and RF circuit design. On the basis of the possibilities gained of the 3D fabrication different antenna concepts were developed. The approaches discussed aim for a specific automotive application as well as for more general integration scenarios.

Although, the Laser Direct Structuring (LDS) technology is already used for different large scale productions of antennas for mobile devices, the RF properties are evaluated in only a limited range. To ensure a reliable fabrication of RF devices and allow for an efficient development process, a detailed analysis of the properties of LDS fabricated RF devices was done first. The analysis of LDS materials showed that there are LDS materials available having dielectric properties that are suitable for RF applications up to 70 GHz. The evaluations showed that LDS thermoplastics are often filled with particles due to mechanical reasons. Those fillers lead to an anisotropy of the material properties, e.g. the dielectric constant. As a further aspect influencing the properties of RF devices, the layered LDS metallisation, was investigated in terms of material properties and surface condition. It showed that the laser structuring causes a specific surface structure that is strongly depending on the direction in which the surfaces are activated with the laser. Considering different methods to model losses due to surface roughness, it could be verified by measurement that the specific surface structure induces less losses than it would be expected on the basis of the parameters typically used to describe such surfaces.

On the basis of the technological evaluation of the fabrication process two antenna concepts for automotive installation spaces were developed. Starting with a given installation space, a shark-fin shaped roof antenna module, a two-antenna MIMO system for LTE/GSM and a two-antenna MIMO system for V2V communication was developed. The volume efficient design on the 3D surface of the shark fin shaped plastic part provides better RF characteristics compared to a reference system. This has been proved during test drives in a LTE live Network in Munich.

On the basis of an evaluation of possible spaces for installation for future vehicular antenna systems, an antenna system was developed to be integrated in the cowl of a convertible. The single antenna elements were fabricated and characterised by measurements. The integration of an antenna system based on these single elements in the target installation space was done. The simulated results proved the suitability of the antenna concept and the installation space in principle.

On the example of microstrip antennas, a further possible use of 3D fabrication methods was shown. After deriving a suitable reference model based on the principle function of microstrip antennas, several concepts using 3D fabrication were discussed. Selected configurations were evaluated on the basis of EM simulations. These showed that modifications of the substrate of a microstrip antenna can be used to adapt the antenna on a given installation space. Furthermore, 3D modifications can be used to modify the radiation characteristic, for example by means of the polarisation. Concerning a circuit integration it could be shown that there are suitable ways to integrate the circuitry directly on the substrate of the patch antenna. The investigations were verified by the development and fabrication of an active GPS antenna. The prototype integrates a LNA circuit under a slotted patch antenna with a triangular shaped surface modulation. The RF characterisation showed a good agreement between simulated and measured results, proving the suitability of the concept and the LDS fabrication, respectively.

A further application of 3D fabrication discussed in this work were waveguide fed antennas. The main concept includes the integration of waveguide fed antennas and a circuit directly into a plastic part. To allow for a connection of the circuit and antenna, a transition between the transmission lines used on the circuit part and the waveguide feeding the antenna has to be made. On the basis of a rectangular dielectric filled waveguide two transitions from RF transmission lines were discussed. It was shown that the possibilities of LDS production can be used to design suitable transitions. Subsequently, two prototype antennas were developed and fabricated operating in 24 GHz and 61 GHz ISM band. This proved the suitability of the LDS process for this antenna concept in terms of function and reliability of the fabrication. Finally, an antenna that is completely integrated in a plastic frame was developed and evaluated for 60 GHz WiGig. This verified the suitability of the approach in principle, by providing sufficient bandwidth and an appropriate radiation characteristic.

References

- [1] J. Franke, *Three-Dimensional Molded Interconnect Devices (3D-MID) - Materials, Manufacturing, Assembly and Applications for Injection Molded Circuit Carriers*, 1st ed. Hanser, 2014.
- [2] D. Unnikrishnan, D. Kaddour, and S. Tedjini, "Molded interconnect devices for rf applications: Transmission lines and low pass filters," in *2012 International Symposium on Signals, Systems, and Electronics (ISSSE)*, Oct 2012, pp. 1–5.
- [3] C. Orlob, D. Kornek, S. Preihs, and I. Rolfes, "Characterization of electromagnetic properties of molded interconnect device materials," in *2009 German Microwave Conference*, March 2009, pp. 1–4.
- [4] D. Unnikrishnan, D. Kaddour, and S. Tedjini, "Microstrip transmission lines and antennas on molded interconnect devices materials," in *2013 13th Mediterranean Microwave Symposium (MMS)*, Sept 2013, pp. 1–4.
- [5] S. G. Pytel, P. G. Huray, S. H. Hall, R. I. Mellitz, G. Brist, H. M. Meyer, L. Walker, and M. Garland, "Analysis of copper treatments and the effects on signal propagation," in *2008 58th Electronic Components and Technology Conference*, May 2008, pp. 1144–1149.
- [6] P. G. Huray, S. Hall, S. Pytel, F. Oluwafemi, R. Mellitz, D. Hua, and P. Ye, "Fundamentals of a 3-d snowball model for surface roughness power losses," in *2007 IEEE Workshop on Signal Propagation on Interconnects*, May 2007, pp. 121–124.
- [7] T. Hansen and F. Hofmann, "Automotive multi- and broadband monopole antenna for gsm, wlan and uwb applications," in *2008 IEEE International Conference on Ultra-Wideband*, vol. 2, Sept 2008, pp. 219–222.
- [8] R. Azaro, F. D. Natale, A. Massa, S. Piffer, and E. Zeni, "Design of an integrated antenna for automotive applications," in *11th International*

- Symposium on Antenna Technology and Applied Electromagnetics [ANTEM 2005]*, June 2005, pp. 1–4.
- [9] K. V. Hoel, S. Kristoffersen, J. Moen, K. G. Kjelgård, and T. S. Lande, “Broadband antenna design using different 3d printing technologies and metallization processes,” in *2016 10th European Conference on Antennas and Propagation (EuCAP)*, April 2016, pp. 1–5.
- [10] H. Kanj and S. M. Ali, “Compact multiband folded 3-d monopole antenna,” *IEEE Antennas and Wireless Propagation Letters*, vol. 8, pp. 185–188, 2009.
- [11] D. Augustin, R. Staraj, O. Benevello, and E. Cambiaggio, “Microstrip antennas printed on inclined planes to constitute original conformal phased arrays,” in *1994 24th European Microwave Conference*, vol. 2, Sept 1994, pp. 1825–1830.
- [12] M. Thiel, “Design considerations for microstrip antennas on cylindrical sector structures,” in *IEEE Antennas and Propagation Society International Symposium (IEEE Cat. No.02CH37313)*, vol. 1, 2002, pp. 88–91 vol.1.
- [13] B. I. Wu and I. Ehrenberg, “Ultra conformal patch antenna array on a doubly curved surface,” in *2013 IEEE International Symposium on Phased Array Systems and Technology*, Oct 2013, pp. 792–798.
- [14] D. Kornek, E. Slotke, C. Orlob, and I. Rolfes, “Experimental investigation of bent patch antennas on mid substrate,” in *Proceedings of the Fourth European Conference on Antennas and Propagation*, April 2010, pp. 1–3.
- [15] F. Sonnerat, R. Pilard, F. Gianesello, F. L. Pennec, C. Person, and D. Gloria, “Innovative lds antenna for 4g applications,” in *2013 7th European Conference on Antennas and Propagation (EuCAP)*, April 2013, pp. 2773–2776.
- [16] A. Cihangir, F. Ferrero, C. Luxey, G. Jacquemod, and P. Brachat, “A bandwidth-enhanced antenna in lds technology for lte700 and gsm850/900 standards,” in *2013 7th European Conference on Antennas and Propagation (EuCAP)*, April 2013, pp. 2786–2789.
- [17] M. Hedges and A. Marin, “3d aerosol jet printing - adding electronics functionality to rp/rm,” in *Proc. Direct Digital Manufacturing Conf.*
- [18] B. Derby, “Inkjet printing of functional and structural materials: Fluid

- property requirements, feature stability, and resolution,” *Annual Review of Materials Research*, vol. 40, no. 1, pp. 395–414, 2010.
- [19] C. Balanis, *Advanced Engineering Electromagnetics*. Wiley, 2012.
- [20] N. Heininger, W. John, and H.-J. Boßler, “Manufacturing of molded interconnect devices from prototyping to mass production with laser direct structuring,” in *International Congress MID*, 2004.
- [21] G. Mallory, J. Hajdu, and American Electroplaters and Surface Finishers Society, *Electroless Plating: Fundamentals and Applications*. The Society, 1990.
- [22] *LDS MID Design Rules - Design rules for laser direct structured MID components*, LPKF Laser & Electronics AG, 2010.
- [23] H. Czichos, T. Saito, and L. Smith, *Springer Handbook of Materials Measurement Methods*. Springer, 2006.
- [24] P. Ansuinelli, A. G. Schuchinsky, F. Frezza, and M. B. Steer, “Passive intermodulation due to conductor surface roughness,” *IEEE Transactions on Microwave Theory and Techniques*, vol. 66, no. 2, pp. 688–699, Feb 2018.
- [25] P. Debye, *Polar Molecules*. Dover, 1929.
- [26] K. S. Cole and R. H. Cole, “Dispersion and absorption in dielectrics i. alternating current characteristics,” vol. 9, pp. 341–351, 04 1941.
- [27] R. N. Clarke, A. P. Gregory, D. Cannell, M. Patrick, S. Wylie, I. Youngs, and G. Hill, “A guide to the characterisation of dielectric materials at rf and microwave frequencies,” Institute of Measurement and Control / National Physical Laboratory,” Report.
- [28] M. Bonnet, *Kunststofftechnik - Grundlagen, Verarbeitung, Werkstoffauswahl und Fallbeispiele*, 2nd ed. Springer Vieweg, 2014.
- [29] *E4991A RF Impedance/Material Analyzer - Data Sheet*, Agilent Technologies, 10 2004.
- [30] A. M. Nicolson and G. F. Ross, “Measurement of the intrinsic properties of materials by time-domain techniques,” *IEEE Transactions on Instrumentation and Measurement*, vol. 19, no. 4, pp. 377–382, Nov 1970.

- [31] J. Baker-Jarvis, "Transmission / reflection and short-circuit line permittivity measurements," National Institute of Standards and Technology," NIST Technical Note 1341.
- [32] S. Zinal and G. Boeck, "Complex permittivity measurements using te_{11p} modes in circular cylindrical cavities," *IEEE Transactions on Microwave Theory and Techniques*, vol. 53, pp. 1870–1874, 2005.
- [33] (2016) Damaskos, inc. website, open resonator. [Online]. Available: <http://www.damaskosinc.com/cavity.htm>
- [34] J. E. Mark, *Polymer Data Handbook*, 1st ed. Oxford University Press, 1999.
- [35] G. Gold and K. Helmreich, "A physical model for skin effect in rough surfaces," in *2012 7th European Microwave Integrated Circuit Conference*, Oct 2012, pp. 631–634.
- [36] S. Kal, A. Bagolini, B. Margesin, and M. Zen, "Stress and resistivity analysis of electrodeposited gold films for mems application," *Microelectron. J.*, vol. 37, no. 11, Nov. 2006.
- [37] S. Groiss, I. Bardi, O. Biro, K. Preis, and K. R. Richter, "Parameters of lossy cavity resonators calculated by the finite element method," *IEEE Transactions on Magnetics*, vol. 32, no. 3, pp. 894–897, May 1996.
- [38] E. Hammerstad and O. Jensen, "Accurate models for microstrip computer-aided design," in *1980 IEEE MTT-S International Microwave symposium Digest*, May 1980, pp. 407–409.
- [39] S. Hall, S. G. Pytel, P. G. Huray, D. Hua, A. Moonshiram, G. A. Brist, and E. Sijercic, "Multigigahertz causal transmission line modeling methodology using a 3-d hemispherical surface roughness approach," *IEEE Transactions on Microwave Theory and Techniques*, vol. 55, no. 12, pp. 2614–2624, Dec 2007.
- [40] P. G. Huray, S. Hall, S. Pytel, F. Oluwafemi, R. Mellitz, D. Hua, and P. Ye, "Fundamentals of a 3-d snowball model for surface roughness power losses," in *2007 IEEE Workshop on Signal Propagation on Interconnects*, May 2007, pp. 121–124.
- [41] G. Ghione and C. Naldi, "Analytical formulas for coplanar lines in hybrid

- and monolithic mics,” *Electronics Letters*, vol. 20, no. 4, pp. 179–181, February 1984.
- [42] H. A. Wheeler, “Formulas for the skin effect,” *Proceedings of the IRE*, vol. 30, no. 9, pp. 412–424, Sept 1942.
- [43] F. Gustrau, *RF and Microwave Engineering: Fundamentals of Wireless Communications*.
- [44] R. B. Marks, “A multiline method of network analyzer calibration,” *IEEE Transactions on Microwave Theory and Techniques*, vol. 39, no. 7, pp. 1205–1215, Jul 1991.
- [45] D. Manteuffel, “Mimo antenna design challenges,” in *2009 Loughborough Antennas Propagation Conference*, Nov 2009, pp. 50–56.
- [46] A. Posselt, L. Ekiz, O. Klemp, B. Geck, and C. F. Mecklenbräuker, “System level evaluation for vehicular mimo antennas in simulated and measured channels,” in *The 8th European Conference on Antennas and Propagation (EuCAP 2014)*, April 2014, pp. 3051–3054.
- [47] C. A. Balanis, *Antenna Theory - Analysis And Design*, 4th ed. John Wiley & Sons, Inc., 2005.
- [48] A. G. Koutinos, D. E. Anagnostou, R. Joshi, S. K. Podilchak, G. A. Kyriacou, and M. T. Chryssomallis, “Modified easy to fabricate e-shaped compact patch antenna with wideband and multiband functionality,” *IET Microwaves, Antennas Propagation*, vol. 12, no. 3, pp. 326–331, 2018.
- [49] Y. Shi and J. Liu, “A circularly polarized octagon-star-shaped microstrip patch antenna with conical radiation pattern,” *IEEE Transactions on Antennas and Propagation*, vol. 66, no. 4, pp. 2073–2078, April 2018.
- [50] K. Mandal and P. P. Sarkar, “High gain wide-band u-shaped patch antennas with modified ground planes,” *IEEE Transactions on Antennas and Propagation*, vol. 61, no. 4, pp. 2279–2282, April 2013.
- [51] L. Peng, C. L. Ruan, and X. H. Wu, “Design and operation of dual/triple-band asymmetric m-shaped microstrip patch antennas,” *IEEE Antennas and Wireless Propagation Letters*, vol. 9, pp. 1069–1072, 2010.
- [52] G. Kumar and K. Ray, *Broadband Microstrip Antennas*, ser. Artech House antennas and propagation library. Artech House, 2003.

- [53] J. James, *Handbook of Microstrip Antennas*, ser. Iee Electromagnetic Waves Series ; 28. Peregrinus, 1989. [Online]. Available: <https://books.google.de/books?id=yfg5chW7kMUC>
- [54] W. Richards, Y. Lo, and D. Harrison, "An improved theory for microstrip antennas and applications," *IEEE Transactions on Antennas and Propagation*, vol. 29, no. 1, pp. 38–46, Jan 1981.
- [55] D. Pozar, "Considerations for millimeter wave printed antennas," *IEEE Transactions on Antennas and Propagation*, vol. 31, no. 5, pp. 740–747, Sep 1983.
- [56] R. Garg, *Microstrip Antenna Design Handbook*, ser. Antennas and Propagation Library. Artech House, 2001. [Online]. Available: https://books.google.de/books?id=_er1LO5pEnUC
- [57] K. Kark, *Antennen und Strahlungsfelder: Elektromagnetische Wellen auf Leitungen, im Freiraum und ihre Abstrahlung*, ser. Aus dem Programm Informationstechnik. Vieweg, 2006. [Online]. Available: <https://books.google.de/books?id=K9YKhe-IXNIC>
- [58] M. U. Khan, M. S. Sharawi, and R. Mittra, "Microstrip patch antenna miniaturisation techniques: a review," *IET Microwaves, Antennas Propagation*, vol. 9, no. 9, pp. 913–922, 2015.
- [59] G. Sanford, "Conformal microstrip phased array for aircraft tests with ats-6," *IEEE Transactions on Antennas and Propagation*, vol. 26, no. 5, pp. 642–646, September 1978.
- [60] C. Krowne, "Cylindrical-rectangular microstrip antenna," *IEEE Transactions on Antennas and Propagation*, vol. 31, no. 1, pp. 194–199, January 1983.
- [61] P. Kabacik, A. Byndas, and M. Hofman, "Optimizing signal coverage in the azimuth plane of conformal microstrip antennas by widening their sectorial beamwidths," in *2017 IEEE International Symposium on Antennas and Propagation USNC/URSI National Radio Science Meeting*, July 2017, pp. 2235–2236.
- [62] R. J. Allard and D. H. Werner, "A flexible analysis and design approach for body-mounted conformal microstrip antennas," in *IEEE Antennas and*

- Propagation Society International Symposium (IEEE Cat. No.02CH37313)*, vol. 1, 2002, pp. 766–769 vol.1.
- [63] R. E. Munson, “Conformal microstrip communication antenna,” in *Military Communications Conference - Communications-Computers: Teamed for the 90’s, 1986. MILCOM 1986. IEEE*, vol. 2, Oct 1986, pp. 23.3.1–23.3.4.
- [64] B. R. Piper and M. E. Bialkowski, “Modelling the distortions to manufacture spherical conformal microstrip antennas,” in *IEEE Antennas and Propagation Society Symposium, 2004.*, vol. 4, June 2004, pp. 3525–3528 Vol.4.
- [65] X. Cheng, J. Shi, J. Kim, C. Kim, D. E. Senior, and Y.-K. Yoon, “Compact self-packaged active folded patch antenna with omni-directional radiation pattern,” in *Proc. 61st IEEE ECTC*.
- [66] D. Poddar, J. Chatterjee, and S. Chowdhury, “On some broad-band microstrip resonators,” *IEEE Transactions on Antennas and Propagation*, vol. 31, no. 1, pp. 193–194, Jan 1983.
- [67] N. Das and J. S. Chatterjee, “Conically depressed microstrip patch antenna,” *Microwaves, Optics and Antennas, IEE Proceedings H*, vol. 130, no. 3, pp. 193–196, 1983.
- [68] W. G. Whittow, “Microstrip patch antennas with 3-dimensional substrates,” in *2012 Loughborough Antennas Propagation Conference (LAPC)*, Nov 2012, pp. 1–5.
- [69] W. S. Yoon, J. W. Baik, H. S. Lee, S. Pyo, S. M. Han, and Y. S. Kim, “A reconfigurable circularly polarized microstrip antenna with a slotted ground plane,” *IEEE Antennas and Wireless Propagation Letters*, vol. 9, pp. 1161–1164, 2010.
- [70] W. Xu, J. Wang, M. Chen, and Z. Zhang, “Radiation and scattering of the microstrip antenna with slotted ground plane,” in *ISAPE2012*, Oct 2012, pp. 325–328.
- [71] B. M. Thomas, “Mode conversion using circumferentially corrugated cylindrical waveguide,” *Electronics Letters*, vol. 8, no. 15, pp. 394–396, July 1972.
- [72] A. A. Kirilenko, L. A. Rud, and V. I. Tkachenko, “Nonsymmetrical h-plane corners for te_{10} - te_{q0} -mode conversion in rectangular

- waveguides,” *IEEE Transactions on Microwave Theory and Techniques*, vol. 54, no. 6, pp. 2471–2477, June 2006.
- [73] W. L. Barrow and L. J. Chu, “Theory of the electromagnetic horn,” *Proceedings of the IRE*, vol. 27, no. 1, pp. 51–64, Jan 1939.
- [74] J. R. James, “Engineering approach to the design of tapered dielectric-rod and horn antennas,” *Radio and Electronic Engineer*, vol. 42, no. 6, pp. 251–259, June 1972.
- [75] G. Armbrecht, C. Zietz, E. Denicke, and I. Rolfes, “Dielectric tube antennas for industrial radar level gauging,” *IEEE Transactions on Antennas and Propagation*, vol. 60, no. 11, pp. 5083–5091, Nov 2012.
- [76] M. Esquiús-Morote, B. Fuchs, J. F. Zürcher, and J. R. Mosig, “Novel thin and compact h-plane siw horn antenna,” *IEEE Transactions on Antennas and Propagation*, vol. 61, no. 6, pp. 2911–2920, June 2013.
- [77] C. Granet and G. L. James, “Design of corrugated horns: a primer,” *IEEE Antennas and Propagation Magazine*, vol. 47, no. 2, pp. 76–84, April 2005.
- [78] Z. Liu and G. Xiao, “A new transition for siw and microstrip line,” in *2013 Asia-Pacific Microwave Conference Proceedings (APMC)*, Nov 2013, pp. 948–950.
- [79] R. Kazemi, A. E. Fathy, S. Yang, and R. A. Sadeghzadeh, “Development of an ultra wide band gcpw to siw transition,” in *2012 IEEE Radio and Wireless Symposium*, Jan 2012, pp. 171–174.
- [80] A. Mukherjee, K. Raghunathan, S. Sundaram, and G. S. Mani, “Waveguide twists and bends,” *Electronic and Radio Engineers, Proceedings of the Indian Division of the Institution of*, vol. 5, no. 2, pp. 37–41, April 1967.
- [81] J. L. Volakis, *Antenna Engineering Handbook*, 4th ed. McGraw Hill, 2007.
- [82] V. Rabinovich, N. Alexandrov, and B. Alkhateeb, *Automotive Antenna Design and Applications*. CRC Press, 2010. [Online]. Available: <https://books.google.de/books?id=P5zMBQAAQBAJ>
- [83] G. Piefke, “A contribution to the theory of corrugated guides,” pp. 533–555, Jan 1960.

- [84] R. Macary and R. Hamilton, "Selectconnect? process for metallizing circuits on molded parts and components," *metal finishing*, pp. 35–37, 2010.
- [85] N. M. Martin, "Improved cavity model parameters for calculation of resonant frequency of rectangular microstrip antennas," *Electronics Letters*, vol. 24, no. 11, pp. 680–681, May 1988.
- [86] B. Curran, "Loss modeling in non-ideal transmission lines for optimal signal integrity," Ph.D. dissertation, Technische Universitaet Berlin, 2012.
- [87] K. Carver and J. Mink, "Microstrip antenna technology," *IEEE Transactions on Antennas and Propagation*, vol. 29, no. 1, pp. 2–24, Jan 1981.
- [88] S. Hall, S. G. Pytel, P. G. Huray, D. Hua, A. Moonshiram, G. A. Brist, and E. Sijercic, "Multigigahertz causal transmission line modeling methodology using a 3-d hemispherical surface roughness approach," *IEEE Transactions on Microwave Theory and Techniques*, vol. 55, no. 12, pp. 2614–2624, Dec 2007.
- [89] R. Munson, "Conformal microstrip antennas and microstrip phased arrays," *IEEE Transactions on Antennas and Propagation*, vol. 22, no. 1, pp. 74–78, Jan 1974.
- [90] N. Heininger, "3d lds components for new production opportunities," *Microwave Journal*, vol. 55, no. 5, Feb 2012.
- [91] S. Babu, I. Singh, and G. Kumar, "Improved linear transmission line model for rectangular, circular and triangular microstrip antennas," in *IEEE Antennas and Propagation Society International Symposium 1997. Digest*, vol. 2, July 1997, pp. 614–617 vol.2.
- [92] K. Carver and J. Mink, "Microstrip antenna technology," in *IEEE Trans. Ant. Prop. AP-29*.
- [93] A. Neto, S. Maci, and P. J. I. D. Maagt, "Reflections inside an elliptical dielectric lens antenna," *IEE Proceedings - Microwaves, Antennas and Propagation*, vol. 145, no. 3, pp. 243–247, Jun 1998.

Curriculum Vitae

Personal Details

Name Aline Friedrich

Date of Birth 14th March, 1982 in Sebnitz, Germany

Nationality German

Education

2006–2011 Diploma in Electrical Engineering, Major: Communication Engineering, Leibniz Universität Hannover, Germany

2011–2019 Research Assistant and Ph.D Student at Institute of Microwave and Wireless Systems, Leibniz Universität Hannover